UC Berkeley
UC Berkeley Electronic Theses and Dissertations

Title
Mineralization of carbon dioxide sequestered in volcanogenic sandstone reservoir rocks

Permalink
https://escholarship.org/uc/item/8c07c21w

Author
Zhang, Shuo

Publication Date
2014

Peer reviewed|Thesis/dissertation

eScholarship.org Powered by the California Digital Library
University of California

Mineralization of carbon dioxide sequestered in volcanogenic sandstone reservoir rocks

by

Shuo Zhang

A dissertation submitted in partial satisfaction of the

Requirements for the degree of

Doctor of Philosophy

in

Earth and Planetary Science

in the

Graduation Division

of the

Univeristy of California, Berkeley

Committee in charge:
Professor Donald J. DePaolo, Chair
Professor Michael Manga
Professor Phillip Geissler

Fall 2014

Mineralization of carbon dioxide sequestered in volcanogenic sandstone reservoir rocks

Copyright 2014

By

Shuo Zhang

Abstract

Mineralization of carbon dioxide sequestered in volcanogenic sandstone reservoir rocks

by

Shuo Zhang

Docotr of Philosophy in Earth and Planetary Science

University of California, Berkeley

Professor Donald J. DePaolo, Chair

We proposed to use volcanogenic sandstones for CO_2 sequestration. Such sandstones with a relatively high percentage of volcanic rock fragments (VRF) could be a promising target for CO_2 sequestration in that they have a sufficient percentage of reactive minerals to allow substantial mineralization of injected $scCO_2$, which provides the most secure form of CO_2 storage, but can also be porous and permeable enough to allow injection at acceptable rates. The limitation in using volcanogenic sandstones as CO_2 reservoir rocks is that porosity and permeability tend to decrease with increase of volcanic rock fragments (VRF) and with the length and complexity of the diagenetic history. Decreased porosity limits the rate at which CO_2 can be injected. We evaluated these tradeoffs to assess the feasibility of using volcanogenic sandstone to achieve highly secure CO_2 storage. Using relationships between VRF percent, porosity and permeability from available geological data, the reactive transport code TOUGHREACT was used to estimate the rate and extent of CO_2 mineralization over 1000 years, and the trade-off between higher reactivity and lower porosity and permeability. For the parameter set that we believe is defensible, the optimal VRF percent for the largest amount of mineralized CO_2 is around 10-20%. The results show that as much as 80% CO_2 mineralization could occur in 1000 years and still allow sufficient injectivity so that ca. 1 megaton of CO_2 can be injected per year per well. The key to estimating how much CO_2 can be injected and mineralized is the relationship between permeability (or injectivity), reactive mineral content, mineral dissolution rates and reactive surface areas. We have sampled examples of volcanogenic sandstones from the Miocene Etchegoin Formation, central California to examine these parameters. Characterizations of these samples by SEM, XRF and XRD show that they are very rich in reactive minerals with around 32% plagioclase, 10% orthopyroxene, 2% clinopyroxene, and 1% ilmenite. Porosities range from 10% to 20%, and permeabilities range from 10 mD to 1000 mD. Batch experiments are also conducted to measure dissolution rates of one of the common minerals in volcanic sandstones, i.e. chlorite. Results show that the released Mg from chlorite in such sandstones could provide enough cations to potentially mineralize about half the stored CO_2 in the pore space within 1000 years. The last chapter presents an extension of the TOUGHREACT code to include carbon 13 isotope into reactive transport modeling. ^{13}C isotope proves to be a great tracer for monitering subsurface flow of CO_2.

Table of Contents

List of Figures

List of Tables

Ackowledgement

I cannot thank my advisor Prof. Don DePaolo enough for finishing this thesis and my entire PhD. He has provided more than everything that an advisor can provide. He is insightful and experienced. He provides explicit comments and advises that help push my project forward whenever I'm stuck. He has resources that are beyond compare. The Center for Nanoscale Control of Geological CO_2 of which he is the director offers multiple opportunities for his students to work on different projects and collaborate with different people. Most of all, he is devoted. He spends hours to revise every manuscript I have written, very extensively, and word by word, although his schedule is always crazy. I consider myself extremely lucky to have Don as my advisor, because I wouldn't be able to finish my PhD without Don in a hundred years.

I also thank all the collabrators, Dr. Tianfu Xu, Carl Steefel, Liange Zheng, Li Yang, Marco Voltolini, Tim Kneafsey, Lauren Beckingham, Jonathan Ajo-Franklin, Ian Bourg, Eric Sonnethal, Christine Doughty, Curt Olderbourg, Nicolas Spycher, Hui-Hai Liu, Joern Larsen and April Van Hise at Lawrence Berkeley National Lab for their patient help in all the details of the multiple projects I worked on.

The Department of Earth and Planetary Science has provided everything I need as a student. I thank Professor Michael Manga, Phillip Geissler, and Douglas Dreger for being in my committee. My peer classmates Jenny Druhan, Jim Watkins, Laura Nielsen, Jesse Day, Andrea Chiang and Carolina Munoz have always been fantastic friends. I wouldn't survive either without the support from Margie Winn, Marilyn Saarni, Shaun Brown, Tom Owens, Tim Teague and Sean Mulcahy.

Last, I must thank my wife Fei Tang, for always being supportive on my pursuing the PhD, and on every decision I have made. I cannot imagine a life without her. Finally to my parents, for loving me, and I love you too Mom and Dad.

Chapter 1 Introduction

The accumulation of CO_2 in the atmosphere increases greenhouse forcing and contributes to global warming. Because it is likely that fossil fuels will continue to be a vital component of energy resources in the next several decades, the emitted CO_2 has to be dealt with in some way. Geological carbon storage is one of the primary options to reduce CO_2 emission during the extended transition to carbon neutral energy sources. Geological formations, especially deep saline aquifers are promising for carbon storage due to their large potential storage capacity and geographic extent. The success of this option will be measured by the storage duration and the risk for leakage. Effective CO_2 storage requires that ≥99% of injected CO_2 be retained in the subsurface for >1000 years (Intergovernmental Panel on Climate Change, 2005).

There are four so-called trapping mechanisms that contribute to retention of CO_2 in the subsurface during geological carbon sequestration (Intergovernmental Panel on Climate Change, 2005): (1) structural trapping, in which CO_2 is trapped as a single supercritical phase according to the structural lithology of the storage zone, (2) capillary trapping, where CO_2 is retained as small (≤1mm) bubbles in pore space due to the fact that CO_2 generally does not wet mineral surfaces whereas saline brine does, (3) dissolution trapping, which refers to CO_2 that becomes dissolved in the ambient liquid phase (brine), and (4) mineral trapping, which is CO_2 that has been incorporated into minerals due to chemical precipitation. Mineral trapping is considered to be the most secure form of CO_2 storage, but is also slow to develop because it follows the slow release of cations like Fe, Mg and Ca by dissolution of silicate and oxide minerals in the rocks. The most likely candidate storage formations for CO_2 sequestration are sedimentary rocks with relatively high porosity and permeability, such as sandstones. The lithologies with the highest porosity and permeability usually are rich in quartz (SiO_2) with some feldspar, and do not contain an abundance of silicate minerals that contain divalent cations that can combine with CO_2 to form carbonate minerals ($CaCO_3$, $MgCO_3$, $FeCO_3$). For sequestration in these types of rocks, modeling studies have shown that only a few percent of injected CO_2 is trapped in minerals even after 1000 to 10000 years has elapsed from the time of injection (Audigane et al., 2007).

Dissolution of CO_2 into the brine and subsequent formation of carbonic acid is the first step in the mineral trapping mechanism. Carbon dioxide dissolves slightly in water to form carbonic acid, which in turn can slowly dissolve silicate minerals. Under appropriate conditions, the divalent cations released by silicate mineral dissolution can combine with dissolved carbonate ions to form stable carbonate minerals. This mechanism, however, requires host rocks with a high acid neutralization potential (Baines and Worden, 2004). Rocks rich in calcium, magnesium, and iron silicate minerals can neutralize acids by providing Ca^{2+}, Mg^{2+}, Fe^{2+} that can form stable carbonate phases in the presence of CO_2 (Gunter et al., 2000).

Igneous rocks, especially mafic and ultramafic rocks, are rich in magnesium, iron, and calcium silicate minerals, and could theoretically provide a high potential of mineral trapping by mineral carbonation (Kelemen and Matter, 2008). However, plutonic igneous (and metamorphic) rocks have negligible matrix permeability and porosity. The permeability in such rocks is determined primarily by the presence, type and orientation of fractures. Thus intrusive igneous and metamorphic rock bodies are normally unpromising hosts for subsurface disposal or sequestration of CO_2, despite the apparently favorable rates of chemical reactions.

Most extrusive igneous rocks are subject to similar limitations for the disposal of CO_2. The most extensive are flood basalts, found covering large areas of the earth's surface in certain parts of the world. Basalts are commonly heavily fractured, and also possess rubble zones and vesicle porosity. Both microcrystalline groundmass and residual glass contain significant Ca, Mg and Fe. Therefore basalts could be candidate host rocks for CO_2 sequestration (Matter et al., 2007; McGrail et al., 2006). If the basalt flows are buried and overlain by impermeable sedimentary cap rocks, they could be favorable potential repositories of supercritical CO_2, particularly if tectonic deformation were to create structural traps. However, the generally low permeability and porosity of the matrix would suggest that CO_2 injection rates would be limited, even if injectivity could be enhanced by hydraulic fracturing. Furthermore, because crystalline rocks do not contain a significant amount of indigenous brine, reaction can only be achieved by injection of CO_2-saturated water (Matter et al., 2007). Since CO_2 is sparingly soluble in H_2O, roughly 200 times the volume of fluid would need to be injected into the rocks to store the same amount of CO_2 that would be accomplished with injection of pure supercritical CO_2. This large volume of fluid translates to the need for 200 times more injection wells, water, and pore space. There are cases where ophiolite complexes are subjected to severe hydrothermal alteration to serpentinites. Large amount of CO_2 mineralization can be expected in these serpentinite-hosted aquifers and serpentinized peridotites due to high reactivity of these rocks. The upscaling of existing technologies that accelerate serpentinite carbonation may prove sufficient for offsetting local industrial emissions. However, global-scale implementation will require considerable incentives and further research and development (Oelkers et al., 1995).

Volcanogenic sandstones with a relatively high percentage of volcanic rock fragments (VRF) could be a promising target for CO_2 sequestration in that they have a sufficient percentage of reactive minerals to allow substantial mineralization of injected CO_2, but can also be porous and permeable enough to allow injection at acceptable rates. The potential shortcoming is that sediments with high VRF fractions tend to be more heavily modified during burial diagenesis, including more compaction and secondary mineral precipitation in pore space, and hence tend to have decreased porosity and permeability (Remy, 1994). However, volcanogenic sandstones are potential or actual petroleum reservoirs in a number of locations (Summer and Verosub, 1992), which indicates that there are instances where porosity and permeability are high enough for oil recovery. Several porosity-enhancing natural mechanisms such as framework-grain dissolution, devitrification of glass at shallow depths, precipitation of early cements that retard compaction, and fracturing have been identified in volcanogenic sandstones (Hawlader, 1990). These processes can produce volcanogenic sandstone formations that are deeply buried but still relatively porous and permeable. Questions remain concerning how common these porosity-enhancing processes are, and our understanding of the major controls on the diagenesis of volcanogenic sandstones is incomplete.

This thesis focuses on predicting the amount of CO_2 that can be mineralized by volcanogenic sandstones reserovirs using combined experimental techniques with multi-phase multi-component reactive transport modeling. Chapter 1 provides the general introduction of CO_2 geological storage, and the mechanisms of CO_2 mineralizaiton by reservoir rocks. Chapter 2 describes the current modeling approach to calculate CO_2 mineralization using geochemical data from the literature, and evaluates the trade-off between permeability and reactivity of volcanic sandstones on the amount of CO_2 mineralization. Sensitivity tests are also conducted for key parameters including reactive surface area, residual gas saturation, and dimension of the model. Chapter 3 takes volcanic sandstone samples from Central California and measures the surface areas and abundances of reactive minerals. The measured data are incorporated into the model to get more relistic results. Chapter 4 measures the dissolution rate of one representative mineral in volcanic sandstones, i.e. chlorite, under conditions relevant to CO_2 sequestration using a flow-through reactor. The dissolution rate of chlorite is determined as a function of pH and chemical affinity at 100 ^{o}C. This rate law is implimented into the reactive transport code for calculating chlorite dissolution. Finally, Chapter 6 provides a newly developed module of the reactive transport code that incorporates ^{13}C isotope into tranditional geochemical calculations. The new module is tested against several theoretical ideal systems, and proves to enhance our understanding of the field data of ^{13}C isotope measured in the CO_2 sequestration project at Pembina, Canada.

Chapter 2 Reactive transport modeling of CO_2 mineralization in volcanogenic sandstone reservoirs

2.1 Introduction

In this chapter, we evaluate, using model rock compositions and measured hydrological properties of sandstones taken from the literature, how volcanic rock fragment abundance will affect the amount of CO_2 that can be injected from a single well and mineralized in a flat-lying 40 meter-thick sandstone reservoir. The reactive transport code TOUGHREACT is used to calculate the amount of CO_2 that can be injected and trapped in minerals, the timescale over which such mineralogical trapping would occur, and how the total amount of mineralized CO_2 varies as a function of rock porosity, permeability and mineralogy. Key uncertain parameters are reactive surface area and residual gas saturation, so sensitivity tests are conducted with varying values for these parameters. This chapter is published in the International Journal of Greenhouse Gas Control in 2013, titled *Mineralization of carbon dioxide sequestered in volcanogenic sandstone reservoir rocks.*

2.2 Problem Setup

2.2.1 Mineralogy of sandstone

To mineralize injected CO_2, the requirement is that there be sufficient Ca, Mg and Fe available to combine with CO_2 to form carbonate minerals, and also that these divalent cations be held in minerals that dissolve relatively rapidly so that the cations are released into solution on a time scale of hundreds of years. In general, those minerals that contain Ca, Mg and Fe in large proportions are also the minerals that dissolve fastest in the presence of acidic aqueous solutions, so there is a correlation between the amount of available cations and the rapidity with which the cations will become available.

Our approach is to evaluate model sedimentary rock compositions that involve mixtures of quartz, alkali feldspar, and basaltic minerals such as plagioclase feldspar and pyroxene, plus iron-titanium oxides. The anorthite component of plagioclase is a source of Ca ions, and the “diopside” and orthopyroxene are sources of Mg, Fe, and additional Ca. Oxide minerals are mainly a source of Fe. This specific mineralogy we use for the simulations is not typical of most volcanogenic sandstones, but we use for illustrative purposes because the dissolution kinetics of these minerals is relatively well studied. In most volcanogenic sands, the divalent cation-bearing minerals are more likely to be chlorite, zeolites, smectite, amphibole, and devitrified lithic fragments that may still contain some of the original igneous minerals such as those we are using for our model composition. The simulations using typical igneous minerals provide us with generalizable results that we can apply in a qualitative way to other sandstone mineralogies.

For our modeling purposes we use an idealized basaltic rock composition for the mineralogy of volcanic rock fragment (VRF) based on the mineralogy of the Palisades Sill, which is holocrystalline and consequently the mineralogy can be specified better than for volcanic rocks that contain devitrified glass and poorly crystalline groundmass. Matter et al. (2007) presented a dolerite analysis from the contact zone between the Palisades Sill and the underlying Newark Basin sediments. The dolerite is rich in Ca-bearing plagioclase and pyroxenes (augite and orthopyroxene) and free of olivine. The whole rock chemistry and observed mineralogy based on thin section analysis of the dolerite are summarized in Table 2.1. The mineralogy used in the model is determined from normative calculation as shown in Table 2.2 from the elemental chemistry, because for the purposes of the model we need to separate out the (Mg,Fe) and (Na,Ca) endmembers as separate minerals, although we use the same dissolution kinetics for the solid solution endmembers. The value of Fe^{3+}/ (total iron) is assumed to be 0.2. Apatite and chromite are ignored since they are present in very small amounts. The diopside in our model is different from the "diopside" of normative calculation in that the diopside in our model only has Mg and Ca, and has no Fe as in the diopside from the normative calculation. This will cause some differences in results but they should not change the conclusions because Mg and Fe are playing similar roles.

Table 2.1 Chemical composition and mineralogy of the Palisades Sill Gabbro

Rock Chemistry Diabase	wt%	Observed Mineralogy[a]
SiO_2	52.2	quartz
Al_2O_3	14.65	plagioclase
CaO	10.43	alkali feldspar
MgO	7.91	hypersthene
Na_2O	2.14	diopside
K_2O	0.69	magnetite
Fe_2O_3	10.14	ilmenite
MnO	0.15	
TiO_2	1.28	
P_2O_5	0.17	
Cr_2O_3	0.07	
LOI[b]	0.2	

a Based on thin section analysis.

b LOI, loss on ignition.

Table 2.2 Normative mineral calculations of mafic volcanic rock fragments

Normative Minerals	Volume fraction	Minerals introduced in the model	Chemical composition	Volume fraction
		Primary minerals		
Quartz	0.0434	Quartz	SiO_2	0.0477
Plagioclase	0.5212	Anorthite	$CaAl_2Si_2O_8$	0.3115
		Albite	$NaAlSi_3O_8$	0.2097
Orthoclase	0.0483	K-feldspar	$KAlSi_3O_8$	0.0483
Hypersthene	0.1847	Enstatite	$MgSiO_3$	0.1339
		Ferrosilite	$FeSiO_3$	0.0508
Diopside	0.1654	Diopside	$CaMgSi_2O_6$	0.1654
Magnetite	0.0172	Magnetite	Fe_3O_4	0.0172
Ilmenite	0.0155	Ilmenite	$FeTiO_3$	0.0155
Apatite	0.0037	Not used		
Chromite	0.0006	Not used		

Total	1.0000

Our strategy is to use the Palisades sill mineralogy as our "volcanic rock fragment" composition, and then to use natural sandstone samples that contain mafic volcanic rock fragments to evaluate the relationships between VRF content and hydrological parameters. Sandstone samples from the Tangbe formation of north central Nepal (Durr and Gibling, 1994) are used as models for sandstone mineralogy (Table 2.3). Volcaniclastic grains are characteristic of Tangbe sandstones, which classify as lithic arenites. The lithic volcaniclastic grains (Lv) are separated into two major groups on the basis of their mineral composition and texture. Mafic grains Lv(M) represent basaltic fragments according to their chemistry. Felsic grains Lv(F), on the other hand, are mainly composed of quartz, plagioclase and K-feldspar (with the ratio of 0.52:0.35:0.13). From their modal composition, felsic grains represent rhyolite and dacite. A small number of volcanic grains Lv(Ch) fits neither group. These grains are made up of material with a chert-like appearance but a characteristic dark brown stain. Feldspar laths in these lithic grains enable classification as volcanogenic grains. For the purposes of calculation of silicate dissolution rates, the Lv(M) component of the sandstones is assumed to have a modal mineralogy the same as the normative mineralogy of the Palisades Sill basalt.

Table 2.3 Point-count results of early Cretaceous volcaniclastic sandstones from Tangbe Formation in north central Nepal.

Sample Number	Lv(M) (%)	Quartz (%)	Plagioclase (%)	K-feldspar (%)	Cement (calcite) (%)	Matrix (%)	Lv(F) (%)	Lv(Ch) (%)	AccOpaq. (%)	Ls+Lm (%)
1	1.6	11.6	4.6	10.6	1.3	9.3	59.3	1.3	0.3	0.3
2	6	12.6	4.6	2.6	0.3	10.3	56	1	4.3	2.3
3	11.3	33.5	7.3	0	19.3	0	24.8	3	0	1
4	21.5	37.5	0.5	0	27.5	0	10.5	2.8	0.3	0
5	32.3	33.8	1.3	0	23.3	1.8	4	1.3	0.3	2.5

Lv(M)=mafic volcanic lithics; Lv(F)=felsic volcanic lithics; Lv(Ch)=chert like volcanic lithics; AccOpaq=accessories and opaques; Ls=sedimentary lithics; Lm=metamorphic lithics

2.2.2 Relationships between volcanic rock fragment percent, porosity and permeability

Several processes can affect porosity during diagenesis of volcanogenic sandstones, including early diagenesis (early leaching by fresh meteoric water, compaction, authigenic mineral precipitation, cementation of first-generation clays and burial dissolution) and late diagenesis (late-stage cements, dissolution of framework grains or cement during structural deformation). The diagenetic processes are controlled by a number of factors, such as depositional environment, detrital mineralogy, grain size, pore-water chemistry, temperature, pressure, and burial history (Remy, 1994). Porosity is strongly influenced by detrital mineralogy. Remy (1994) showed that rocks with abundant VRF experienced the most compaction, hence had decreased post-compaction porosity (which equals current macroporosity plus cement and can be considered as the remaining porosity after early compaction but before cementation). Cements vary in mineralogy. First-generation chloritic mixed-layer clays are most abundant in volcaniclastic petrofacies, whereas first-generation illite-smectite and calcite are most abundant in nonvolcaniclastic petrofacies, so the relationship between the extent of cementation and VRF is not easy to generalize. Also uncertain is the production of secondary porosity due to dissolution as a function of VRF. In rocks rich in VRF and with very low initial porosities, pore-water circulation is severely restricted, thereby preventing significant dissolution of framework grains. In rocks rich in VRF and with relatively high porosity, the presence of chemically-unstable lithic fragments promotes the formation of secondary porosity. The complexities of diagenesis make it difficult to predict permeability based on original sandstone mineralogy or any other single compositional or textural parameter. Ultimately, because it is impossible to specify permeability accurately even if porosity is known, we vary permeability over a small range to evaluate its importance in determining the outcome of the simulations.

As one approach to representing the effect of VRF abundance on rock porosity, we used the empirical relationships Eq. 2.1 and Eq. 2.2 from Bloch (1991) to calculate porosity and permeability from mineralogy.

$$\text{Porosity} = -6.1+9.8(1/\text{sorting}) +0.17\text{rigid grain content} \qquad (2.1)$$

$$\text{Log}_{10}\text{Perm} =-4.67+1.34\text{grain size}+4.08(1/\text{sorting}) +0.0342\text{rigid grain content} \qquad (2.2)$$

Here “sorting” is the Trask sorting coefficient (Saccocia and Seyfried Jr, 1994), “perm” is permeability in millidarcys, and “grain size” is grain diameter in millimeters. The two equations were obtained by fitting the data from Yacheng field, South China Sea. The model has a large amount of independent information, and a high coefficient of determination (R^2=0.75 for porosity and 0.86 for permeability). All of the fitted sample data lie within a 95% confidence interval of predicted values as shown in Bloch (1991) (Figure 14 and Figure 15 in the reference), although these limits are large enough to significantly affect the performance of potential reservoirs in a CO_2 sequestration scenario.

The empirical equations from Bloch (1991) imply that porosity and permeability are affected by mineralogical variables (rigid grain content) and textural variables (grain size and sorting). Since the objective is to evaluate the effect of mineralogy on rock porosity and permeability, we assigned typical values to textural variables. The Trask sorting coefficient is given a value of 1.5 for well to moderately sorted sandstone, and grain size is assigned as 0.8 mm. Since the calibration data set is based on wells with similar temperature and pressure histories, post-depositional parameters (temperature, pressure, time) are not incorporated in these models. So all the uncertainties in textural variables (sorting and grain size) and post-depositional parameters (temperature, pressure, time) are gathered in the constants calculated with sorting coefficient =1.5 and grain size =0.8. Below we see that these values lead to slightly smaller permeabilities than expected from field data, and this is compensated by generating another permeability set that covers slightly larger permeability values.

Another approach to evaluating mineralogy-permeability relations is to use natural sandstones where there are sufficient characterization data to evaluate the variability as well as the overall trends. Gibson-Poole et al. (2008) presented porosity and permeability data from Gippsland Basin in southeast Australia. The data for the Kingfish Formation sediments are reprinted here in Fig. 2.1. The porosities are mostly in the range 10% to 30% and the permeabilities vary from about 0.1 to 10,000 mD. The majority of the points lie in the 15-30% porosity and 10-10,000 mD permeability ranges. The empirical formula generated by determining a best fit to these data is:

$$k = 0.0442e^{36.29\phi} \qquad (2.3)$$

where k is permeability in mD and ϕ is porosity. According to this equation, at least 8.6% porosity is needed to provide a minimum permeability (i.e. 1md) for injection. Clearly this relationship has limited applicability because the permeability can vary by a factor of over 100 for the same porosity. Nevertheless, we use this relationship as a reference, and use Equations 2.1 and 2.2 and the mineralogy of the Tangbe sedimentary rocks to calculate porosity and permeability. These calculated values all lie close to but below the best-fit line of the Kingfish Formation porosity-permeability data.

Our conclusion is that Equations 2.1 and 2.2 give a reasonable estimate of porosity-permeability relations in arenites, but that the large spread in permeability at all porosities means that no one porosity-permeability curve can adequately represent the likely range in natural reservoirs. To account for this range, and to evaluate the effect of permeability, we use two sets of permeability values. Those calculated directly from Equations 2.1 and 2.2 are noted as "low permeability," and another set of porosity-permeability data ("high permeability") is also used in our model where all permeabilities are increased by 5 times. This additional set of permeability data is beneficial in that the relationship between VRF and permeability is key to this study and the two data sets allow us to illustrate the large effect of the permeability-porosity relationship. Our selected range of values is nevertheless small in comparison to the likely natural range as illustrated in Fig. 2.1. Further discussion of permeability and its effects is provided in the Section 2.4.

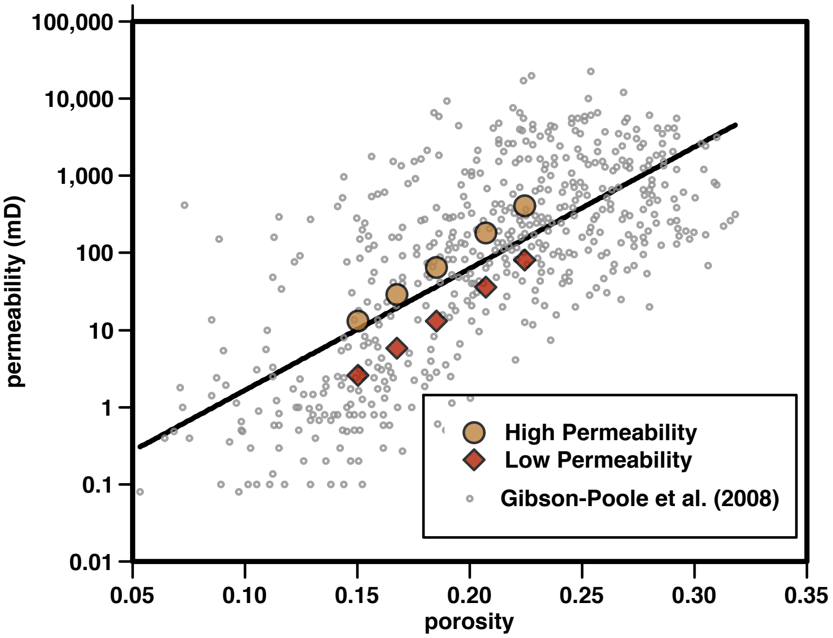

Figure 2.1 Relationship between permeability and porosity from literature and porosity-permeability values used in the models

Table 2.4 Mineral assemblages, porosities, permeabilities and injection rates for different VFR percentages

Sample Number	Lv(M) (%)	Quartz (%)	Anorthite (%)	Albite (%)	K-feldspar (%)	Calcite (%)	Enstatite (%)	Ferrosilite (%)	Diopside (%)	Magnetite (%)	Ilmenite (%)	Total (%)	Porosity (%)	Low Permeability (mD)	High Permeability (mD)
1	1.6	51.05	6.51	13.02	16.50	1.30	0.21	0.08	0.26	0.03	0.02	89.00	22.46	81.15	405.76
2	6	50.07	7.01	14.03	8.39	0.30	0.80	0.30	0.99	0.10	0.09	82.10	20.70	36.06	180.31

3	11.3	50.51	6.36	12.72	2.98	19.30	1.51	0.57	1.87	0.19	0.18	96.20	18.51	13.06	65.29
4	21.5	45.50	4.73	9.47	2.07	27.50	2.88	1.09	3.56	0.37	0.33	97.50	16.76	5.80	29.01
5	32.3	38.00	6.36	12.72	1.95	23.30	4.32	1.64	5.34	0.56	0.50	94.70	15.03	2.60	12.99

2.2.3 Hydrogeological setting and model

The mafic volcanic rock fragment percent of the Nepal samples ranges from 1.6% to 32.3%. Reservoir porosities and permeabilities are calculated for each sample and then listed in Table 2.4. Brine compositions are obtained by pre-equilibrating 1.0 mol/L NaCl saline water with the respective corresponding mineral assemblage for 10 years. All simulations are run initially with a 1-D model with radial symmetry. The model is therefore in some sense a 2-D model, but we refer to it as 1-D because the fluids are not allowed to segregate vertically due to buoyancy forces. We have run 2-D radial models as well, and the differences between 1-D and 2-D models are relatively small and discussed further below. Initial reservoir pressure is set at constant 200 bar with a formation temperature of 75 ^{o}C. This temperature is calculated for a depth of 2 km, given a land surface temperature of 15 ^{o}C and a geothermal gradient of 30 ^{o}C/km. Formation thickness is set to 40m. Continuous injection is assumed to take place over a period of 100 years at a constant injection rate of 1 megaton CO_2 per year. For the lower reservoir permeabilities that are associated with our model rocks with higher VRF, injection pressure needs to be increased to achieve the same injection rate of 1 Mt/yr. We set a maximum injection pressure of 390 bar (39 MPa). In cases where the reservoir permeability is too low to allow injection of 1 Mt/y CO_2 at this injection pressure, the injection pressure is set at 39 MPa and the rate is decreased to be consistent with the permeability. Geochemical transport simulations are continued until 1000 years, an arbitrary cutoff chosen to limit the computational time for the models and to allow us to compare the amount of CO_2 mineralized in a specified amount of time.

Table 2.5 Hydrogeologic parameters for the radial fluid flow problem

Aquifer thickness	40m
Compressibility	$4.5 \times 10^{-10} Pa^{-1}$
Temperature	$75^{o}C$
Pressure	200bar
Reactive surface area	$10 cm^2/g$
Residual gas saturation	0.1
Salinity (mass fraction)	0.06
Relative permeability	
Liquid(van Genuchten, 1980)	
$k_{rl} = \sqrt{S^*}\left\{1-(1-[S^*]^{1/m})^m\right\}^2$	$S^* = (S_l - S_{lr})/(1-S_{lr})$
Irreducible water saturation	$S_{lr} = 0.30$
Exponent	$m = 0.457$
Gas (Corey,1954)	
$k_{rg} = (1-\hat{S})^2(1-\hat{S}^2)$	$\hat{S} = \frac{(S_l - S_{lr})}{(S_l - S_{lr} - S_{gr})}$
Irreducible gas saturation	$S_{gr} = 0.1$
Capillary pressure	
Van Genuchten (1980)	
$P_{cap} = -P_0([S^*]^{-1/m} - 1)^{1-m}$	$S^* = (S_l - S_{lr})/(1-S_{lr})$
Irreducible water saturation	$S_{lr} = 0.00$
Exponent	$m = 0.457$

Strength coefficient	$P_0 = 19.61 kPa$
Tortuosity	
$\tau = \phi^{1/3} S^{3/7}$	
Porosity	ϕ
Phase saturation	S

2.3 Modeling Approach

2.3.1 Simulation method

Simulations are conducted using the nonisothermal reactive transport code TOUGHREACT V2 (Xu and Pruess, 2001a). This code introduces reactive chemistry into the existing multiphase fluid and heat flow code TOUGH2 (Pruess, 1991b). A new fluid property module, ECO2N, is used based on the work by Spycher and Pruess (2005). ECO2N provides an accurate description of the thermophysical properties of water and CO_2 mixtures under conditions typically encountered in saline aquifers for CO_2 disposal (10 ºC ≤ T ≤110 ºC; P ≤ 600 bars).

Fluid and heat flow processes considered in this code are: (1) fluid flow of liquid and gas phases under pressure and gravity forces, (2) capillary pressure effects for liquid phases, and (3) heat flow by conduction, convection and diffusion. Transport processes that affect aqueous and gaseous species are advection, molecular diffusion and hydrodynamic dispersion. For our simulations, chemical reactions between dissolved aqueous species and gas (i.e. supercritical CO_2) are assumed to be locally at equilibrium (although TOUGHREACT V2 can consider aqueous species kinetics). Mineral dissolution and precipitation are subject to kinetic limitations.

The space discretization in our modeling is based on the integral finite difference (IFD) method (Narasimhan and Witherspoon, 1976). This method allows the use of unstructured grids, which is well suited for simulation of flow, transport, and fluid-rock interactions in heterogeneous and fractured rock systems with varying petrology, and hence provides flexible discretization of geologic media. For regular grids, the IFD method is equivalent to the conventional finite difference method.

TOUGHREACT uses a sequential iteration approach for calculations of flow, transport, and kinetic geochemical reactions (but noniterative between transport and chemistry). After solving flow equations, velocities and saturations of the aqueous phase are used for aqueous chemical transport calculations. Chemical transport is solved on a component basis. Resulting concentrations obtained from the transport and CO_2 gas pressures from multiphase flow calculation are then substituted into a chemical reaction model. The system of chemical reaction equations is solved on a grid-block basis by Newton-Raphson iteration.

An automatic time step control is used for the flow calculation. Time step size is doubled if convergence occurs within 4 Newton-Raphson iterations. The starting time step is 1 second and the upper limit for time step size is set to be 5 days. For transport equations, a stabilized bi-conjugate gradient solver is used. No limit of the time step size for chemical reactions is included.

2.3.2 Flow and transport model setup

The specific model we used for our calculation is a 1-D model with distance *d* ranging from 0 m to 100 km, which can be considered as infinitely long. For boundary conditions, there is no flow at both *d*=0m and *d*=10^5m. For fixed injection pressure condition, the first grid is assigned an infinitely large volume (10^{50}m^3) and a gas saturation of 100% so that it serves as a CO_2 source and its properties don't change during the simulation. For the fixed injection rate condition, the injection well is also located in the first grid. Since the distance is large enough to be considered infinite in the model, the right end boundary condition is equal to an open end although there is no flow at d=10^5m. For initial conditions, the temperature is set to be 75 ^oC and the pressure is 200 bar. Initial gas saturation is zero and the formation is filled with all brine. Initial brine compositions are obtained by pre-equilibrating 1.0mol/L NaCl saline water in a batch model for 10 years with minerals that are used later for reactive transport modeling. Water chemistry is not changing after 10 years, which indicates that a steady state fluid composition has been reached under pre-injection conditions.

The equations for calculating relative permeability and capillary pressure and corresponding parameters are listed in Table 2.5. They are all from Van Genuchten(2008). Changes in porosity and permeability due to mineral dissolution and precipitation are taken into account in our model. Changes in porosity during the simulation are monitored by tracking changes in mineral volume fractions. We chose a simple grain model of Kozeny-Carman to calculate changes in permeability due to changes in porosity, although the actual porosity-permeability correlation in geologic media depends on a complex interplay of many factors such as pore size distribution, pore shapes, and connectivity. The Kozeny-Carman equation relates permeability *k* (in m^2) to porosity (ϕ) by

$$k = \frac{R_0}{45}\left(\frac{\phi^3}{(1-\phi)^2}\right) \tag{2.4}$$

where R_0 is the initial local spherical close-pack radius. Hence, the ratio of permeability *k* to initial permeability k_0 can be expressed as

$$\frac{k}{k_0} = \left(\frac{\phi}{\phi_0}\right)^3\left(\frac{1-\phi_0}{(1-\phi)}\right)^2 \tag{2.5}$$

where ϕ_0 is the initial porosity. Since porosity decreases are of order 10% of initial porosities during the course of the simulations, and the initial porosities average about 16.8%, the typical permeability change over 1000 years is $k/k_o \approx 0.68$. Using the fitted porosity-permeability relationship from Gibson-Poole et at. (2008) presented earlier, the ratio of final permeability and initial permeability k/k_o is 0.52 (initial porosity= 16.8%, final porosity= 15.0%), which is in the same order with the result from the Kozeny-Carman model used in the simulation. Considering the several orders of magnitude of permeability range and the large uncertainties in determining the porosity-permeability relation from geological data, the error caused from using the Kozeny-Carman equation is negligible.

For species transport, the diffusion coefficient for aqueous species is set to be 10^{-9} m^2/s. The diffusion coefficient is then multiplied by the tortuosity and liquid saturation. The diffusion coefficient of the medium for gaseous species is $10^{-5}m^2/s$. Tortuosity is calculated internally from the Millington and Quirk (2012) model, which is listed in Table 2.5.

2.3.3 Geochemical data

The reaction rate expression used in this paper is based on the transition state theory (TST) (Steefel and Lasaga, 1994):

$$r = kA\left[1 - \left(\frac{Q}{K}\right)^{\theta}\right]^{\eta} \tag{2.6}$$

where r is the kinetic rate (positive values indicate dissolution, and negative values indicate precipitation), k is the rate constant (moles per unit mineral surface area and unit time) which is temperature dependent, A is the specific reactive surface area per gram of mineral, Q is the reaction quotient, and K is the equilibrium constant for the mineral-water reaction written for the destruction of one mole of mineral, whose values originated from the EQ3/6 V7.2b database (wolery, 1992). The parameters θ and η must be determined by experiment, but are commonly set to unity when experimental quantification is not available. Precipitation of secondary minerals is represented using the same kinetic expression, although as noted below this is a simplification for which there is little justification other than lack of more detailed information.

The kinetic rate constant k^T (where T is the temperature in Celsius) can be summed from three mechanisms (Palandri, 2004):

$$\begin{aligned} k &= k_{nu}^{25}\exp\{\frac{-E_{nu}}{R}\left(\frac{1}{T}-\frac{1}{298.15}\right)\} \\ &+k_{H}^{25}\exp\{\frac{-E_{H}}{R}\left(\frac{1}{T}-\frac{1}{298.15}\right)\}a_{H}^{n_H} \\ &+k_{OH}^{25}\exp\{\frac{-E_{OH}}{R}\left(\frac{1}{T}-\frac{1}{298.15}\right)\}a_{OH}^{n_{OH}} \end{aligned} \tag{2.7}$$

where subscripts nu, H, and OH indicate neutral, acid, and base mechanisms respectively, E is the activation energy, k^{25} is the rate constant at 25°C, R is gas constant, T is absolute temperature, a is the activity of species, and n is a constant power term.

Mineral dissolution and precipitation rates are a product of the kinetic-rate constant, the reactive surface area and the affinity term (1-Q/K), which describes how far the system is from equilibrium, as represented by Eq. 2.6. The parameters used for the kinetic rate expression are given in Table 2.6. We included separate rate constants (k_{25}), activation energies (E), and reaction orders (n) for processes catalyzed by H^+ and OH^-. At any pH, the total rate is the sum of the rates from all mechanisms. However, catalysis by H^+ or OH^- is only considered for mineral dissolution, not for precipitation. Parameter values for the rate law were taken from Palandri (2004), who compiled and fitted experimental data reported by many investigators. Solid solution effects are not considered in this study. To make up for this deficiency, the kinetic parameters of end members of each solid solution are set equal to the *slowest* one, e.g. anorthite is set to albite; ferrosilite is set to enstatite; and smectite-Na is set to smectite-Ca. These simplifications are conservative but all potentially significant. We have not attempted to evaluate each one independently because that would result in an unwieldy number of simulations and would affect the results in reasonably predictable ways (e.g. faster dissolution kinetics will allow for more dissolution per unit time and hence more mineralization).

Table 2.6 Parameters for calculating kinetic rate constants of minerals (Palandri, (2004))

Mineral	RSA (cm^2/g)	Parameters for kinetic rate law								Note
		Neutral mechanism		Acid mechanism			Base mechanism			
		k_{25} (mol/m^2 s)	*Ea* (kJ/mol)	k_{25}	Ea	n (H^+)	k_{25}	Ea	n (H^+)	
Quartz	9.8	$1.0233 x 10^{-14}$	87.7							
Anorthite	9.8	$2.7542 x 10^{-13}$	69.8	$6.9183 x 10^{-11}$	65.0	0.457	$2.5119 x 10^{-16}$	71.0	-0.572	Set to albite
Albite	9.8	$2.7542 x 10^{-13}$	69.8	$6.9183 x 10^{-11}$	65.0	0.457	$2.5119 x 10^{-16}$	71.0	-0.572	
K-feldspar	9.8	$3.8905 x 10^{-13}$	38.0	$8.7096 x 10^{-11}$	51.7	0.5	$6.3096 x 10^{-22}$	94.1	-0.823	
Enstatite	9.8	$1.9055 x 10^{-13}$	80.00	$9.5499 x 10^{-10}$	80.00	0.6				
Ferrosilite	9.8	$1.9055 x 10^{-13}$	80.00	$9.5499 x 10^{-10}$	80.00	0.6				Set to enstatite
Calcite	9.8	$1.5488 x 10^{-06}$	23.5	$5.0199 x 10^{-01}$	14.4	1.0				
Diopside	9.8	$1.9055 x 10^{-13}$	80.00	$9.5499 x 10^{-10}$	80.00	0.6				
Magnetite	9.8	$1.6596 x 10^{-11}$	18.6	$2.5704 x 10^{-09}$	18.6	0.279				
Ilmenite	9.8	$6.9183 x 10^{-12}$	37.9	$4.4668 x 10^{-09}$	37.9	0.421				
Magnesite	9.8	$4.5709 x 10^{-10}$	23.5	$4.1687 x 10^{-07}$	14.4	1.0				
Siderite	9.8	$1.2598 x 10^{-09}$	62.76	$6.4565 x 10^{-04}$	36.1	0.5				
Dolomite	9.8	$2.9512 x 10^{-08}$	52.2	$6.4565 x 10^{-04}$	36.1	0.5				
Dawsonite	9.8	$1.0000 x 10^{-07}$	62.8							
Ankerite	9.8	$2.9512 x 10^{-08}$	52.2	$6.4565 x 10^{-04}$	36.1	0.5				
Kaolinite	151.6	$6.9183 x 10^{-14}$	22.20	$4.8978 x 10^{-12}$	65.9	0.777	$8.9125 x 10^{-18}$	17.90	-0.472	
Illite	151.6	$1.6596 x 10^{-13}$	35.00	$1.0471 x 10^{-11}$	23.6	0.34	$3.0200 x 10^{-17}$	58.9	-0.40	
Smectite-Na	151.6	$1.6596 x 10^{-13}$	35.00	$1.0471 x 10^{-11}$	23.6	0.34	$3.0200 x 10^{-17}$	58.9	-0.40	Set to smectite-Ca
Smectite-Ca	151.6	$1.6596 x 10^{-13}$	35.00	$1.0471 x 10^{-11}$	23.6	0.34	$3.0200 x 10^{-17}$	58.9	-0.40	

If the aqueous phase supersaturates with respect to a potential secondary mineral, a small volume fraction of 1×10^{-6} is used for calculating seed surface area for the new phase to grow. Possible secondary minerals that are considered in this model are listed in Table 2.7. Precipitation of secondary minerals is represented using the same kinetic expression as that for dissolution. However, several aspects of precipitation are different from dissolution, such as nucleation and crystal growth. Some authors have argued that dissolution and precipitation are fundamentally identical but opposite in sign (Dove et al., 2008), whereas others provide evidence that there are pronounced differences. The kinetics of dissolution are more likely to be important for the results presented here, and it is clear that all reactive transport models are simple representations of what are likely to be complex relationships that depend on solution composition in ways that are not reflected by just the degree of saturation of the particular mineral under consideration. The complications relating to mineral precipitation are not considered in the current model. Since precipitation rate data for most minerals are unavailable, only parameters for neutral pH rates were employed to describe precipitation. Multiple kinetic precipitation mechanisms can be specified in an input file of the TOUGHREACT program, should such information become available.

Table 2.7 Structural formula of secondary minerals

Secondary minerals	Chemical formula
Magnesite	$MgCO_3$
Calcite	$CaCO_3$
Dolomite	$CaMg(CO_3)_2$

Siderite	$FeCO_3$
Dawsonite	$NaAlCO_3(OH)_2$
Ankerite	$CaMg_{0.3}Fe_{0.7}(CO_3)_2$
Kaolinite	$Al_2Si_2O_5(OH)_4$
Illite	$(K,H_3O)(Al,Mg,Fe)_2(Si,Al)_4O_{10}[(OH)_2,(H_2O)]$
Smectite-Na	$Na(Al,Mg,Fe)_4(Si,Al)_8O_{20}(OH)_4.nH_2O$
Smectite-Ca	$Ca(Al,Mg,Fe)_4(Si,Al)_8O_{20}(OH)_4.nH_2O$

Mineral reactive surface areas (RSA) are based on the work of Sonnenthal et al. (2005), and are calculated assuming a cubic array of truncated spheres constituting the rock framework. In conformity to White and Peterson (1990) and Zerai et al. (2006), a surface roughness factor of 10 is incorporated and defined as the ratio of true surface area to equivalent geometric surface area. Interaction with minerals is generally expected to occur only at selected sites of the mineral surface, and the actual RSA could be one to three orders of magnitude less than the surface roughness-based surface area due to coating or armoring (Zerai et al., 2006). To account for these effects, the actual RSA are decreased by 100 times from the surface roughness-based surface areas. The RSA used here (9.8 cm^2/g) for most minerals are similar to those used by Zerai et al. (2006). Clay minerals are assigned much larger RSAs (151.6 cm^2/g) due to small particle size.

To provide the reactive surface area in the unsaturated system corrected by rock/water ratio, the surface area of each mineral (in units of $m^2_{mineral}/kg_{water}$), which is internally calculated, is given by:

$$A_m(m^2 / kg_{water}) = \frac{A_r f_m (S_w - S_m)}{\rho_w \phi_f (1 - S_m) S_w}$$

Where A_r is the reactive surface area in units of $m^2/m^3_{fracture\ medium}$, f_m is volume fraction of the mineral, ρ_w is the density of water (in kg/m^3), ϕ_f is porosity of the medium, S_w is water saturation, S_m is the minimum liquid saturation for which water-rock reactions are considered. S_m was set to a small saturation (e.g. $1x10^{-4}$) in our model, to ensure that reactions take place until virtually no water is left since water is the wetting phase during CO_2 sequestration.

Typically in reactive transport modeling a representative element volume is a well-mixed homogenous block. So here we don’t treat the volcanic rock fragments and the rest of the sandstone as two spatially separate materials in one grid block. Instead the effects of volcanic fragments on the properties of the grid blocks are taken into account in two ways. First, the percentages of volcanic rock fragments are used to calculate porosity and permeability of the whole sandstone. Second, the rock fragment percentages are used to calculate the percentages of reactive minerals; these reactive minerals are then embedded in the rock homogenously with RSA=9.8 cm^2/g which is the same as the other minerals in the sandstone. In this approach, we are assuming that the rock fragments have the same porosity, permeability and RSA as the rest of the rock. These assumptions represent the simplest possible approach, but may be justified for our purposes. For example, we have examined volcanic sandstone samples from the Echegoin Formation near Coalinga, California (thin section picture shown in Figure 2.2). The volcanic fragments of this sandstone have similar sizes as the other mineral grains, which should give similar RSAs for reactions. Also the volcanic fragments are mostly equally distributed in the sandstone, which is reasonable support for our assumption of homogeneous porosity and permeability.

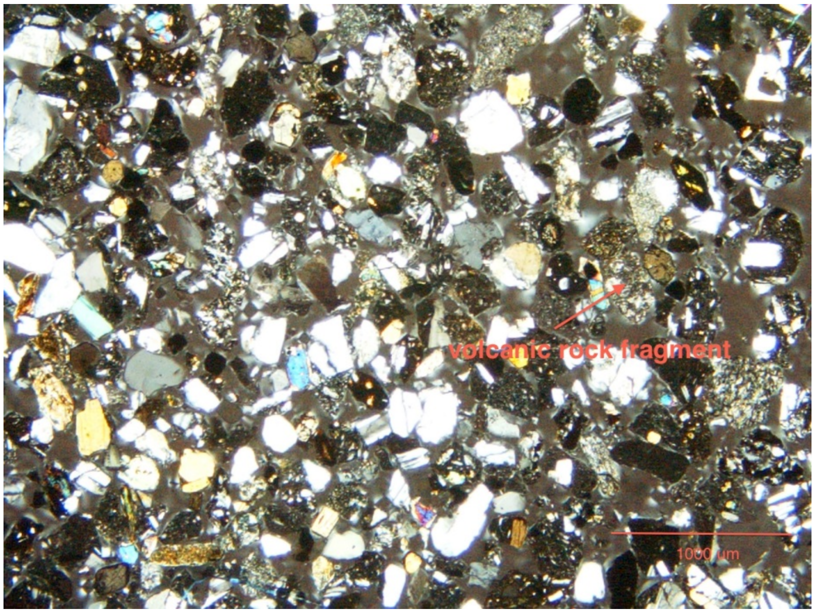

Figure 2.2 Thin section picture of a volcanic sandstone sample from Coalinga, California

2.4 Results

As described in Section 2.2, we selected 5 volcanogenic sandstone samples from Central Nepal that have chemical and mineralogical data available. Porosities and permeabilities were calculated for each sample using empirical equations generated from the Yacheng field. Another set of permeability data was generated by multiplying the original ones by 5 to cover a larger range of permeability values, but a range that is still small in comparison to the full range of possible permeabilities as represented by the Gibson-Poole et al. (2008) data (Figure 2.1). Injection rate is fixed at 1 megaton per year for samples with a large permeability that requires no larger than 390 bar injection pressure, whereas samples with low permeabilities that would need more than 390 bar were set at constant injection pressure of this maximum value and thus had less than 1 Mt/yr of CO_2 injected. All samples were run with the reactive transport code TOUGHREACT using a 1-dimensional (radial) model. The simulations generated results for the distance that the CO_2-bearing fluid would flow, how much CO_2 is mineralized, and how system properties such as gas saturation and pH are distributed along the flow path.

2.4.1 Relationships between VRF and CO_2 mineralization amount

The relationships between the amount of mineralized CO_2 and %VRF are presented in Fig. 2.3 and Fig. 2.4. For the Low Permeability case, sample 1 and sample 2 have injection rates of 1 Mt/yr while samples 3-5 (progressively higher VRF) are fixed at constant injection pressure of 390 bar since they would need a pressure higher than 390 bar to achieve 1 Mt/yr and we assume that standard injection equipment can achieve an injection pressure only as high as 390 bar. As permeability decreases from sample 2 to sample 5, the amount of injected CO_2 decreases. However, since the amount of reactive VRF increases from sample 1 to sample 5, a larger percent of injected CO_2 is mineralized. The trade-off between increasing reactivity and decreasing permeability generates an optimal case at VRF ≈ 6% where the amount of mineralized CO_2 has the largest value. For the High Permeability case, the amount of injected CO_2 and mineralized percent show similar patterns as those in the Low Permeability set, but the optimal case shifts from 6% to somewhere between 10% and 21% VRF. Thus it can be seen that the amount of mineralized CO_2 depends on how we determine permeabilities from mineralogy, or more generally the relationships between mineralogy, porosity and permeability. Nevertheless, the results suggest that if formations can be identified that have relatively high VRF and modest permeability, mineralization of injected CO_2 can be almost quantitative over a timescale of 1000 years.

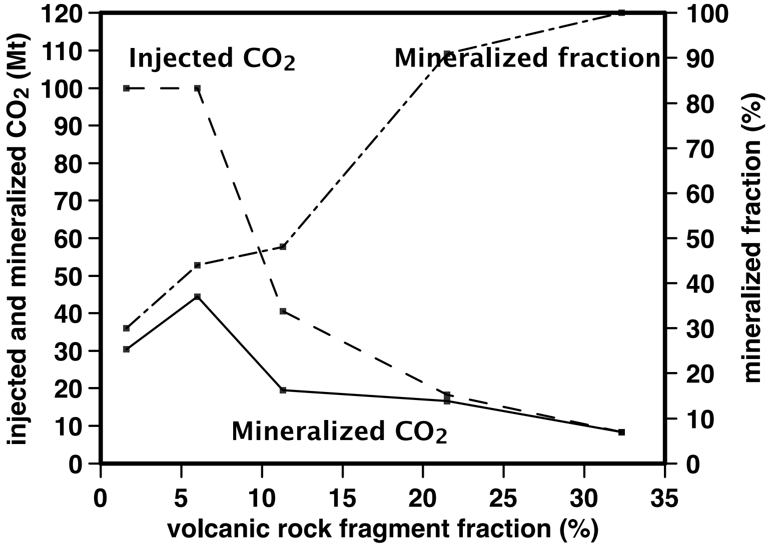

Figure 2.3 The amount of injected CO_2 and mineralized CO_2 and the fraction of mineralization (after 1000 years) for different mafic VRFs for the low permeability data set

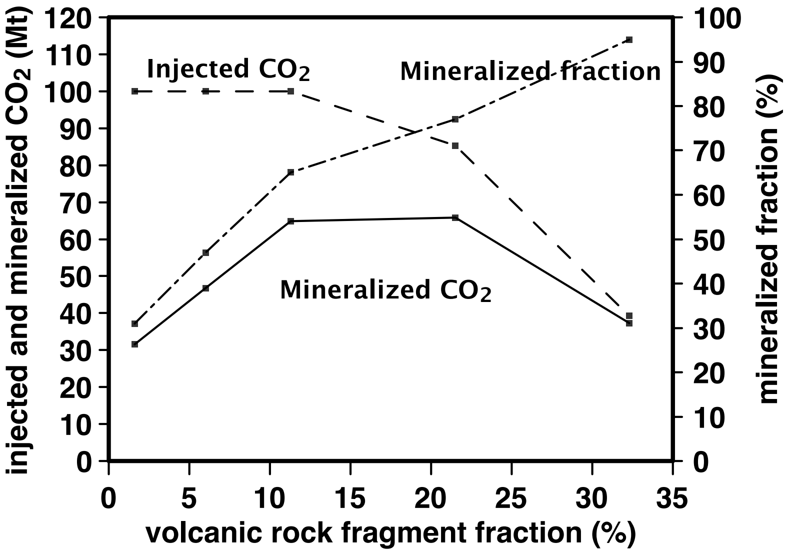

Figure 2.4 The amount of injected CO_2 and mineralized CO_2 and the fraction of mineralization (after 1000 years) for different mafic VRFs for the high permeability data set

Fig. 2.5 shows the evolution of total sequestered CO_2 in the mineralized phase, aqueous phase and supercritical phase for the entire reservoir in the case of 21% VRF in the High Permeability case. CO_2 injection is conducted for 100 years and then stopped. Supercritical CO_2 phase dominates at first and then decreases rapidly after injection ceases, first due to dissolution into the aqueous phase, and then due to mineralization. The amount of aqueous CO_2 increases first until it reaches saturation in water; its value stays roughly stable until about 700 years. Overall, supercritical CO_2 first dissolves in the aqueous phase, and then reacts with cations in the aqueous phase released by mineral dissolution and produces carbonate precipitation. About 78% of injected CO_2 is mineralized, 6% remains in the aqueous phase, and 16% remains as the supercritical phase at time = 1000 years.

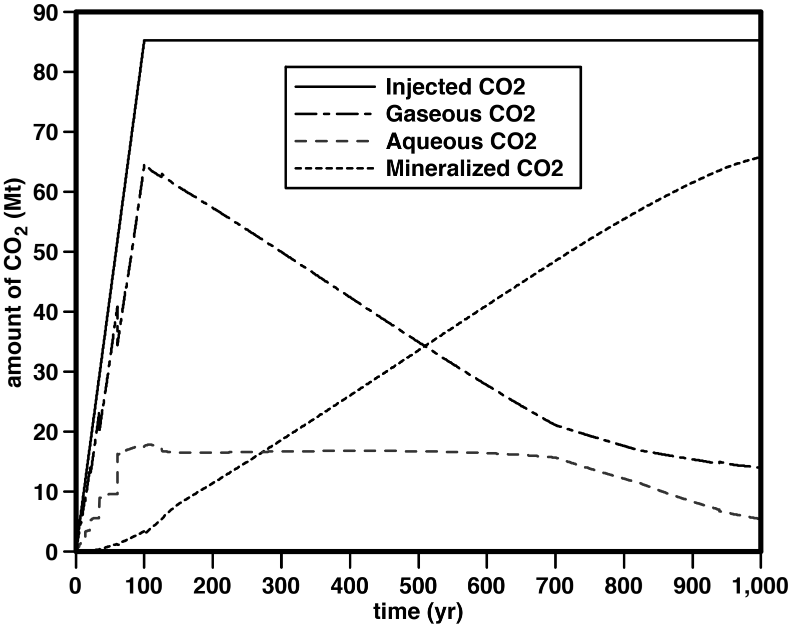

Figure 2.5 Cumulative CO_2 injection and CO_2 mass in different phases for the optimal case of mineralized CO_2 (VRF = 22%, from Figure 2.4)

2.4.2 Radial distribution of system properties for the optimal case

The radial distribution of reservoir pressure, gas saturation, pH, porosity, and CO_2 sequestration amount per medium volume are presented in Fig. 2.6a –2.6e. The CO_2 - affected region is limited within a radial distance of 4500m-6000m except for pressure. In our 2-fluid phase 1-D model, the primary variables are pressure, temperature, gas phase saturation and salt mass fraction. The pressure near injection well as shown in Fig. 2.6a is 390 bar from the beginning to 100 years, when CO_2 is injected into the formation. Pressure decreases further way from the injection well, and the affected distance reaches 60 km, where the hydrostatic pressure is 200 bar. The high pressure decays after injection ceases at 100 years and already returns to hydrostatic pressure at 200 years. Gas saturation is close to 100% within 200 meters from the CO_2 injection well at the time of 100 years, which means that water is almost completely replaced by supercritical CO_2. Further away from the injection well, supercritical CO_2 phase and water phase coexist, where the gas saturation decreases from 1 to 0 as shown in Figure 2.6b. Mutual dissolution of CO_2 and water is also considered and calculated in the model. Subsequently supercritical CO_2 dissolves into the brine and is consumed by mineralization, so the gas saturation line moves down after 100 years, which indicates a decrease of gas saturation in the system. At the same time, water gradually flows back spontaneously due to the suction of water by the rock (capillary pressure). This process of spontaneous flow of the wetting phase into porous media is called imbibition. Gas saturation and water saturation add up to 1 at any time and at all places.

The pH decreases from 8.0 to 5.0 close to the injection well due to CO_2 injection. The low pH induces accelerated mineral dissolution due to the increase in dissolution rate at low pH. The track along which the pH line moves is similar with that in the gas saturation graph. The line moves forward during the first 100 years, and gradually moves backward during the next 900 years, which indicates that a large amount of CO_2 is mineralized subsequent to 100 years when water flows back. Porosity decreases from the original value of 0.168 to 0.150 at 1000 years. This decrease happens because CO_2 mass is added to the solid matrix by rock alteration. The change in porosity reduces permeability to 77% of its original value according to Eq. 2.5. The total mineralized CO_2 reservoir per unit volume keeps increasing monotonically during the whole time period. After 1000 years, the value reaches about 37 kg/m^3. This value would keep increasing if the simulation were not stopped.

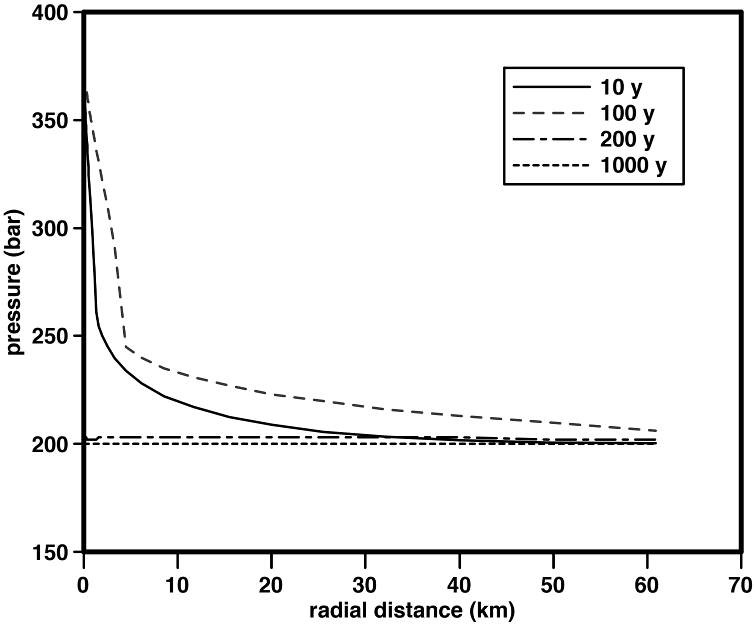

Figure 2.6a: Radial distribution of reservoir pressure at different times for the optimal case

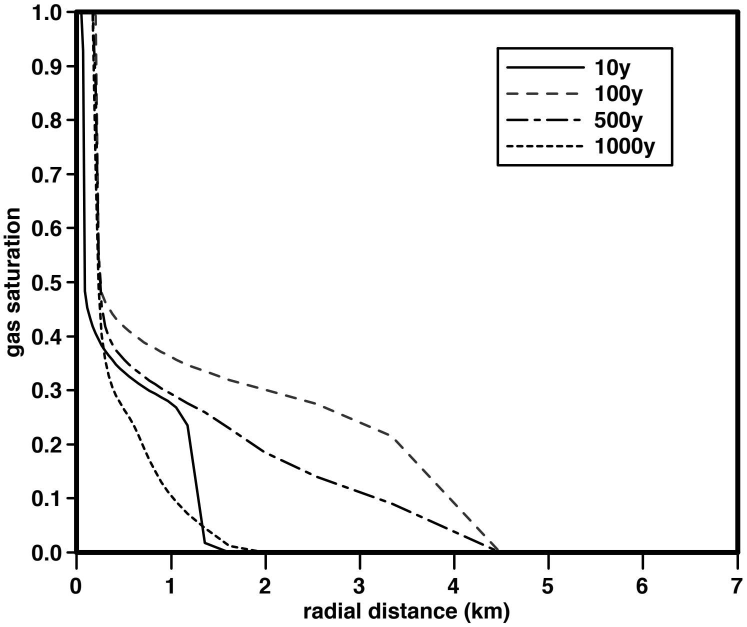

Figure 2.6b: Radial distribution of CO_2 gas saturation at different times for the optimal case

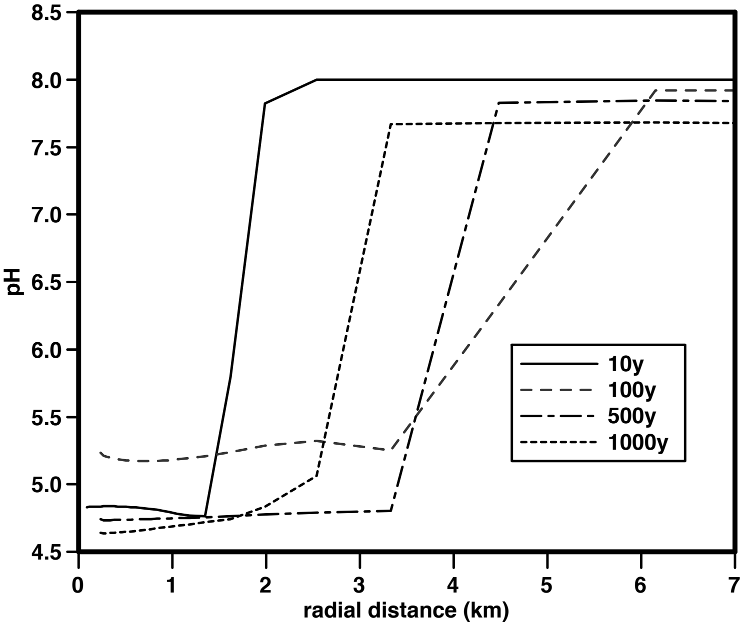

Figure 2.6c: Radial distribution of pH at different times for the optimal case

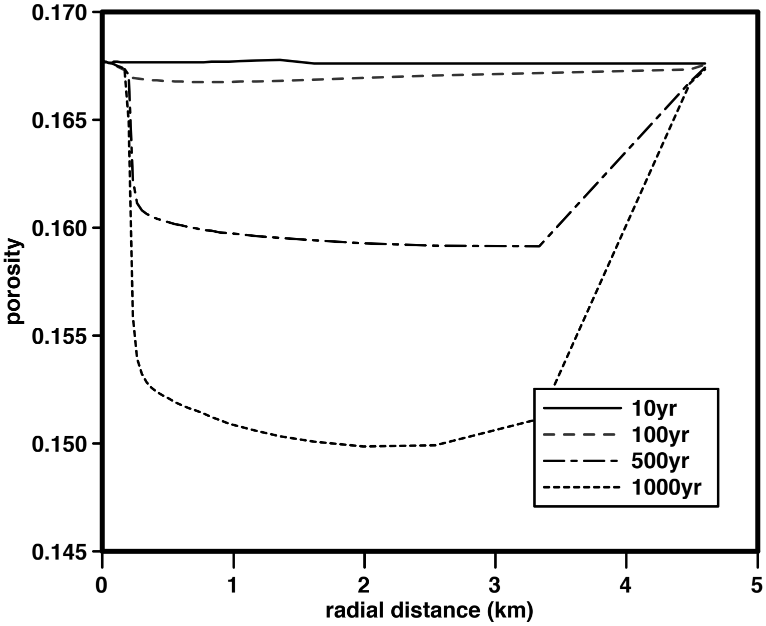

Figure 2.6d: Radial distribution of porosity at different times for the optimal case

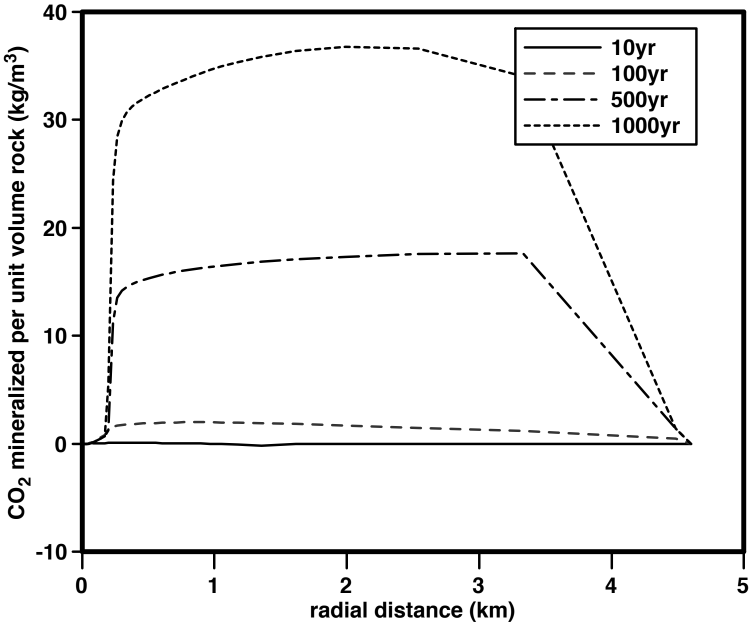

Figure 2.6e: Radial distribution of the amount of mineralized CO_2 per unit volume of medium at different times for the optimal case

2.4.3 Mineral alteration and aqueous phase composition of the optimal case

Minerals and aqueous species with significant changes of abundance are presented in Fig. 2.7a, 2.7b and 2.8. The minerals of the model volcanic rock fragment (pyroxene mainly) all dissolve significantly. As these minerals dissolve, the concentrations of Mg, Fe, and Ca are all increased in the aqueous fluid, and pH is also increased, eventually leading to precipitation of secondary phases. Some of the injected CO_2 is immobilized by precipitation of three carbonate minerals: magnesite, ankerite and calcite. Precipitation of ankerite is due to ferrosilite dissolution to provide Fe^{2+}. Magnesite and calcite precipitation is due to the dissolution of anorthite, enstatite and diopside components to provide Ca^{2+} and Mg^{2+}. Some Ca^{2+} and Mg^{2+} remain in the aqueous phase. There is also significant precipitation of quartz, and significant dissolution of anorthite and precipitation of albite. Minor precipitation of K-feldspar, siderite and dawsonite with abundance changes in the order of 10^{-5} also occur but are not plotted due to their small values. The decrease in pore volume is attributable largely to the fixation of CO_2 into mineral phases and secondarily to the fact that the replacement minerals have lower average density than the primary minerals used for the calculation.

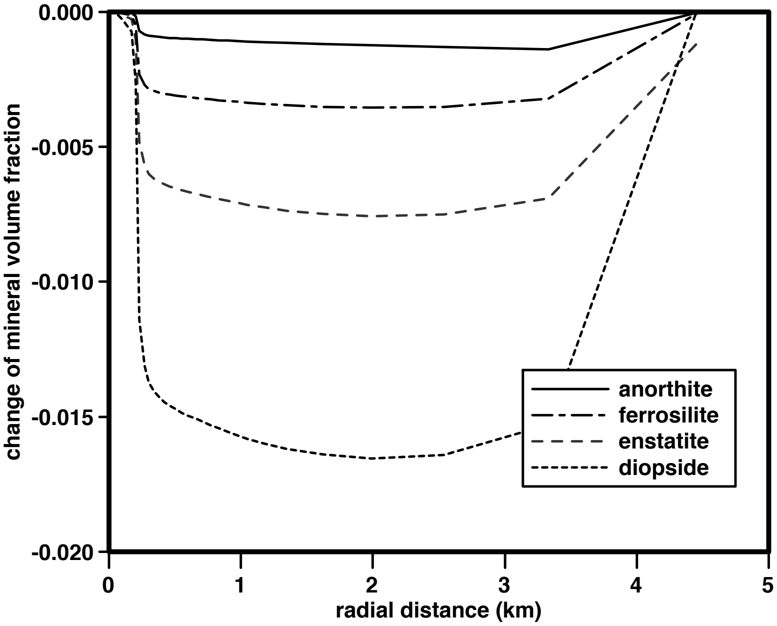

Figure 2.7a: Radial distribution of volume fraction changes of major dissolving minerals at 1000 years for the optimal case

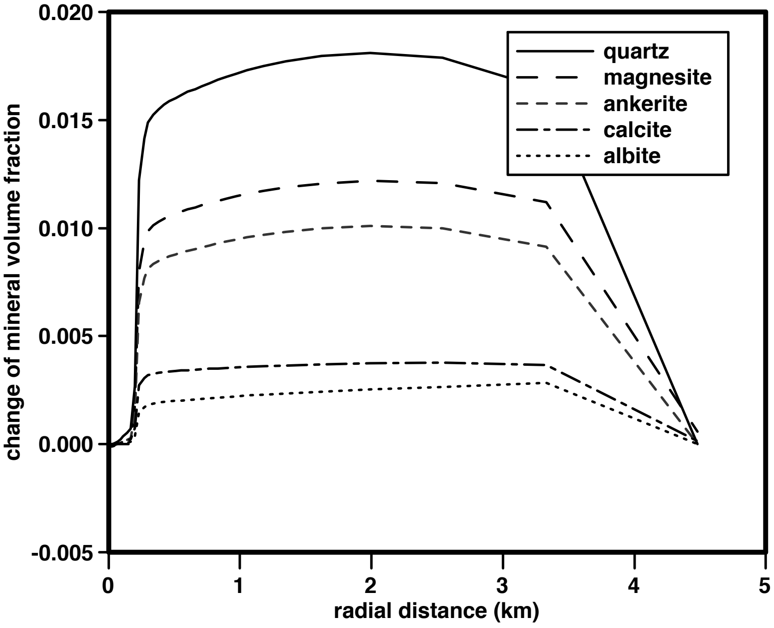

Figure 2.7b: Radial distribution of volume fraction changes of major precipitating minerals at 1000 years for the optimal case

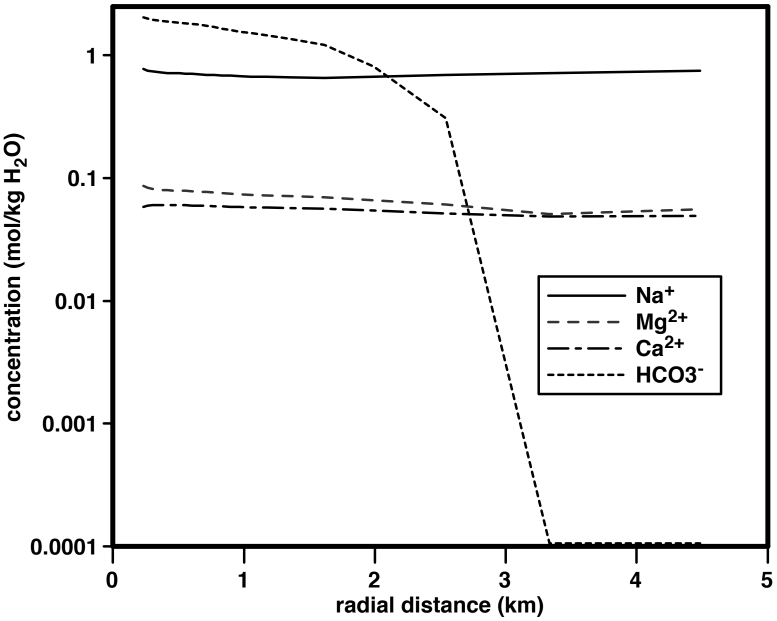

Figure 2.8 Radial distribution of concentrations of major aqueous species at 1000 years for the optimal case

2.5 Discussion and implications

Our simulations suggest that volcanogenic sandstones may be attractive reservoir rocks for geologic carbon sequestration. Volcanogenic sandstones have the advantage of high reactivity as in basalt and peridotite, but are in other respects typical porous sandstones that would allow for deep injection of supercritical CO_2 rather than shallow injection of carbonated water as in Kelemen and Matter (2008). The results of our simulation study, which is based on a combination of observed properties of impure sandstones and a model mineralogy including up to 30% by volume of reactive, divalent cation-bearing minerals, a 40m-thick homogeneous formation with a radius of 5000 m could accommodate injection of 85 megatons of supercritical CO_2 through a single well in 100 years, with 77 percent of the injected CO_2 being converted to carbonate minerals within 1000 years. Because CO_2 storage will only be justifiable if injected CO_2 stays immobilized in the subsurface for thousands of years, this high percentage of mineralization would be attractive.

Typical volcanogenic sandstones are mixtures of mineral grains and volcanic and sub-volcanic rock fragments (Ingersoll, 1983; Linn et al., 1992). To simulate the reactive behavior of volcanic rock fragments we have used a combination of minerals, mainly pyroxenes and feldspar, for which laboratory dissolution rate data are available. In general we have used conservative values for dissolution rate constants and reactive surface area. Nevertheless, the critical control on the percentage of mineralization that can be achieved is the relationship between the volume fraction of reactive minerals (or the fraction of volcanic rock fragments) and permeability. The models suggest that >50% mineralization could be achieved within 1000 years in formations containing at least 10% VRF and a permeability of about 60 mD. We assume, and there are some data in the literature to bear this out, that permeability declines as VRF increases. With this assumption, there is a trade-off between higher reactivity and lower permeability with increasing VRF. But for any reactive mineral content, there is a range of permeabilities that are likely as a result of variable diagenetic histories and proportions of cements. For our low permeability cases, permeability drops off quickly at high VRF, which means that the total amount of CO_2 that can be injected per well is small, and hence the optimum condition for mineralization occurs at low %VRF. For our high permeability cases, the optimum condition shifts to about 15 to 20% VRF, and much more CO_2 can be both injected and mineralized.

2.5.1 Reactive surface area

The evaluation of reactive surface area (RSA) in natural geologic media is complex, especially for multi-mineral systems, and has not yet been described in a manner that would allow accurate estimation for a given mineralogy and porosity. RSA calculated from grain size is often a poor estimate of the hydrologically accessible mineral surface area. The specific RSA may vary over several orders of magnitude depending on grain size, mineralogy, surface roughness, coatings, weathering, and biological effects.

Sensitivity tests with respect to RSA are based on the optimal case with 21% VRF in the high permeability set. Two additional simulations were performed by respectively increasing and decreasing all RSAs uniformly by a factor of 5, which is arbitrarily chosen. The RSAs for secondary minerals are changed by the same factor. Results in Fig. 2.9 show that RSA has a direct effect on the rate of CO_2 mineralization. The amount of injected CO_2 also changes, but very slightly, so only the original injection line is plotted. Varying RSA between $2cm^2/g$ and $50cm^2/g$ changes the mineralized fraction from 29% to 95% at 1000 years. In the RSA= 50 cm^2/g case, reaction is very fast and the CO_2 mineralization reaches its maximum at about 400 years and stops increasing afterwards.

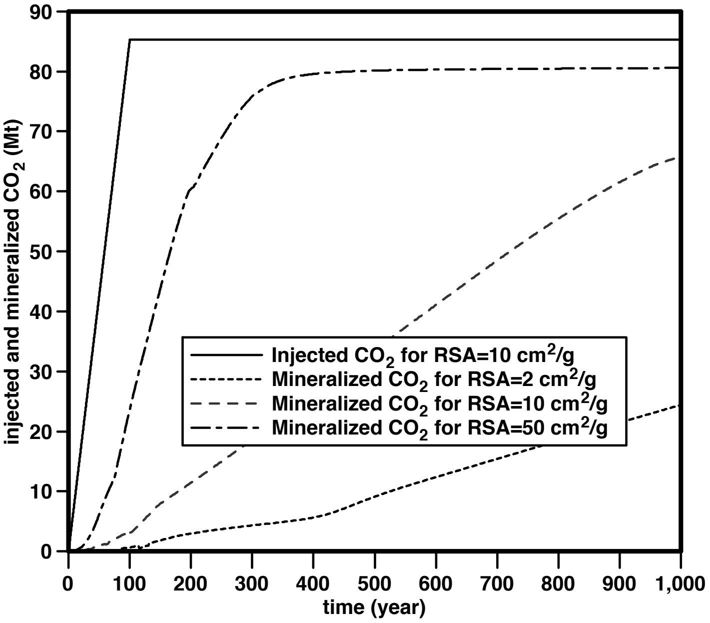

Figure 2.9 The amount of mineralized CO_2 for the optimal case for different reactive surface area values

2.5.2 Residual gas saturation

Residual gas saturation (RGS) was shown to play an important role in storing CO_2 by Kumar et al.(2004; 2004). In our baseline model a value of 0.10 was assigned to RGS, which is consistent with experimental measurements by Kitamura et al. (2006). In the sensitivity tests a smaller value of 0.05 and a larger value of 0.2 are arbitrarily chosen for comparison. However, such values are both possible from core scale measurements or previous models (Park et al., 2003; Prigiobbe and Mazzotti, 2011). Fig. 2.10 shows that small values of RGS lead to increased mineralization of CO_2. This increase comes about because a greater amount of gas remains mobile, which leads to increased contact between CO_2 and brine. In terms of relative permeability, a smaller value of residual gas saturation gives larger values of the relative permeability of supercritical CO_2 phase, especially in low gas saturation zones. The exact equation that describes the relationship between gas relative permeability and residual gas saturation used in this study can be found in Table 2.5. Thus more CO_2 can be injected into the formation for smaller residual gas saturation due to larger gas permeability. About 95 Mton of CO_2 is injected into the formation in 100 years with an injection pressure of 390 bar for RGS=0.05, while only 85 Mton of CO_2 can be injected at the same pressure with RGS = 0.2. Also, CO_2 flows farther for smaller residual gas saturations and occupies a larger volume of the domain. For example, the pH front for RGS=0.1 is at 6000 meters at 100 years as shown in Figure 2.6c, while the pH front of RGS=0.05 is around 9000 meters. So, the volume of rocks that are exposed to CO_2 is larger for smaller RGS values. For our model, the rate-controlling step of mineralization is the dissolution of mafic minerals, which is measured in moles of minerals per unit time per unit volume of rock. With similar dissolution rates, the amount of mineralized CO_2 is thus proportional to the volume of rock that is involved in reactions with CO_2, and increases for smaller values of RGS.

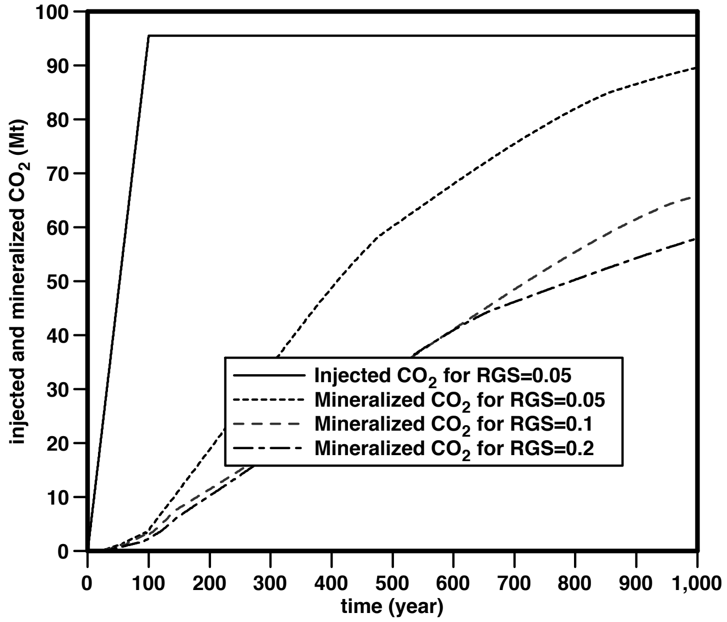

Figure 2.10 The amount of mineralized CO_2 for the optimal case for different residual gas saturation values

2.5.3 Mineralogy and trapping efficiency

Minerals that are sources of divalent cations and common in impure sandstones are biotite, chlorite, glauconite, amphibole, epidote, and montmorillonite. Chlorite and montmorillonite are common alteration products of volcanic glass, and VRF are commonly composed of combinations of such minerals as well as devitrified glass that is effectively amorphous. Available data suggest that the dissolution rates of these minerals are not much different from those used for our simulations. However, they may critically affect the types of secondary minerals formed and the ability for CO_2 to be sequestered by carbonates due to the different types of secondary minerals, and their effect on permeability. Nevertheless, to first order it appears that the specific mineralogy is less important than the amount of reactive minerals. It is also noteworthy that minerals such as chlorite and montmorillonite could have significantly higher reactive surface areas than the values we are using (Landrot et al., 2012).

As shown in Table 2.6, typical dissolution rate constants for divalent cation-bearing silicates are near 10^{-10} mol/m^2/sec at temperature of 75 ^{o}C, which translates to about 0.003 mol/m^2/y. This number has also included the acceleration by the acid mechanism as indicated by Equation 2.7, and will approximate the actual dissolution rate if the solutions are moderately far from equilibrium. If a rock contains 10 volume percent of a mineral with density of 2800 kg/m^3 and specific surface area of 1 m^2/kg, 1m^3 of such rock would contain 280 m^2 of reactive surface area. With these numbers, the predicted timescale of mineral dissolution would be about 1000 years; or in other words roughly 2/3 (actually $1 - e^{-1}$) of the reactive mineral inventory would dissolve in 1000 years. Assuming a molecular weight similar to feldspar (about 280 g/mol), about 600 moles of reactive mineral would be dissolved in 1000 years. For comparison, if 5 to 10% of the rock volume is initially filled with CO_2 at a density of 600 kg/m^3, then the 1m^3 volume contains about 30 to 60 kg of CO_2 or about 680 to 1360 moles of CO_2. Hence the release of cations from mineral dissolution over 1000 years is approximately enough to mineralize 40 to 90 percent of the capillary-trapped CO_2.

The above calculation is significant because it implies that the reaction rate and reactive mineral fraction of reservoir rocks are the critical parameters for assessing mineralization of injected CO_2. It also shows that slight changes in the rates can have a large effect on the result. If dissolution rates are retarded by 10x, there will likely be 10x less mineralization over 1000 years. And if the rates could be enhanced, there would be significant benefit in terms of increasing the amount of mineralized CO_2.

Audigane et al (2007) used a reactive transport model to estimate the relative fractions of capillary trapped, dissolved, and mineralized CO_2 in the Utsira Formation, a quartz-rich sandstone that is being used as a reservoir formation for the Sleipner CO_2 sequestration project. In their simulation, they calculate that only 1-2% of the CO_2 is mineralized after 1000 years. This small amount of calculated mineralization is consistent with the fact that they had only 1.3% by volume of reactive mineral (Fe-rich chlorite), and that the conversion of CO_2 to $FeCO_3$ (about 20 mol/m^3 by 1000 years) was offset by a similar amount of CO_2 release by dissolution of calcite.

Our simulations suggest that the mineralogical trapping efficiency of impure sandstones can be reduced to a relatively simple parameter that involves permeability, reactive mineral percentage and residual CO_2 saturation:

$$E_{MT1000} = \frac{X_{rm}\rho_{rm}M_{co_2}}{s_g\rho_{co_2}M_{rm}} \approx \frac{X_{rm}}{s_g}$$

where X_{rm} is the volume fraction of reactive minerals containing divalent cations, and s_g is the residual gas saturation for CO_2 in brine. The approximate sign applies because the ratio of densities and molecular weights is close to unity for typical minerals and supercritical CO_2. This ratio is effectively a ratio of the number of divalent cations available per unit volume of reservoir rock to the number of CO_2 molecules present as capillary-trapped bubbles. If $X_{rm} / s_g \geq 1$, then a large fraction of injected CO_2 can be expected to be mineralized. For our simulations that produce high mineralization fractions in 1000 years this ratio is in the range 1 to 2. If reaction rates are higher or lower than assumed in our models, it will not greatly affect the fraction of CO_2 mineralized, but it will affect the timescale over which the mineralization happens. The remaining significant parameter is the injectivity, which scales roughly with permeability. Hence, in economic terms, the figure of merit would be:

$$E_{MT1000} = \frac{k_h X_{rm}}{s_g}$$

If this number is high, it will maximize the amount of CO_2 that can be injected and expected to mineralize in 1000 years *per injection well.* Based on our simulations, more than half of injected CO_2

could be mineralized with an injection rate of 1 MT CO_2/yr for formations where this number is ≥50 mD.

5.4 Fractures, heterogeneity, and 2-D effects

A critical component of our analysis is the formation injectivity for CO_2. Our models assume that injectivity is directly determined by the core-scale permeability, which may be an overly conservative assumption. In most cases, the effective permeability at the scale of injection (10's of meters) can be 1 or even 2 orders of magnitude higher than the core-scale permeability (Raghavan, 2006). This difference is usually attributed to larger scale heterogeneity, including the presence of fractures, and tends to be more significant in rocks with lower permeability. If this scale dependence effect were taken into account, it would greatly enhance the potential for mineralization. In terms of our figure of merit, sandstones with much lower permeability could still be effective storage targets. One additional factor that will be important, however, is how mineralization and dissolution will affect the fracture permeability (Sausse et al., 2001).

Formation heterogeneity can also affect both hydrology and geochemical evolution during sequestration. If, for example, a formation has mineralogical heterogeneity, and if permeability decreases as reactive minerals increase as we assumed in our model, then during injection, flow will be concentrated in the regions of high permeability (low %VRF). This would mean that during injection, much of the CO_2 will be separated from the reactive minerals, with the separation distances being similar to the length scales that characterize the permeability heterogeneity. This effect might increase mineralization. The high permeability zones will enhance the injectivity and allow more CO_2 to be injected into the formation per unit time per well. In the early stages of system evolution there is some separation of CO_2 from reactive minerals, but on longer time scales, the CO_2 (and or H^+) will be able to diffuse into the reactive zones. Assuming that the effective diffusivity of CO_2 $D \approx 0.23$ m^2/yr at 100°C(Zeebe, 2011), the diffusion lengthscale in 100 years $L_d \approx (4D\phi t)^{0.5} = 3$ meters, and in 1000 years is about 10 meters. Thus, the low pH conditions in the high-permeability zones will penetrate the low permeability zones if the scale of the heterogeneity (mostly vertical heterogeneity), is of order a few meters or less. The overall effect may be positive as injectivity will be increased but reactivity on a 1000-year time scale will remain similar. As noted by Bryant et al. (1996), permeability heterogeneity may also enhance structural and capillary trapping of CO_2.

Although the calculations we present are 1-dimensional (quasi 2-dimensional because they are radially symmetric), the results do not change much when the extra (vertical) dimension is added. Simulations done using a 2-D (quasi 3-D) allow for buoyancy effects, which allow the CO_2 to rise upward toward the caprock and spread somewhat farther. It also results in more contact area between CO_2 and brine, and hence somewhat faster dissolution of CO_2 into brine and slightly more extensive mineral-rock interaction. The overall effect is to allow somewhat more CO_2 (ca. 18% more) to be mineralized as shown in Figure 2.11.

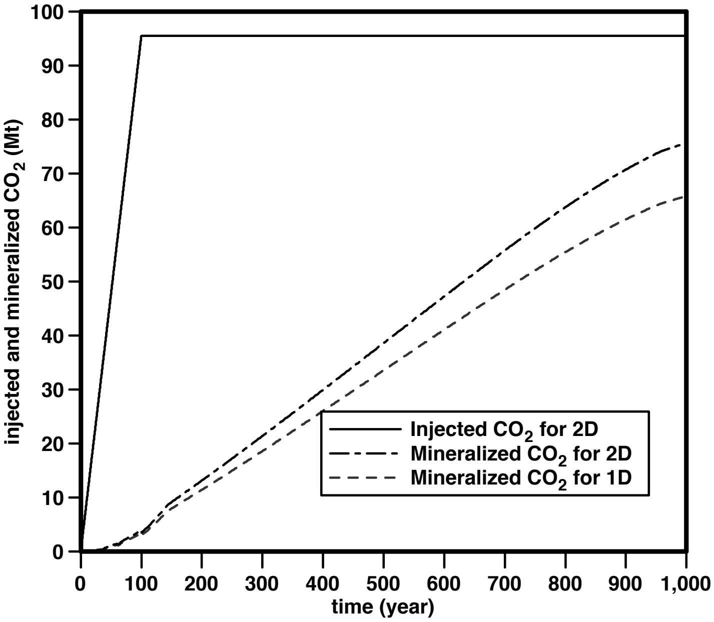

Figure 2.11 The amount of mineralized CO_2 for the optimal case for 1D and 2D model

2.6 Conclusions

As a potential target lithology for CO_2 sequestration, volcanogenic sandstone has both the advantage of high reactivity as in basalts and peridotite, reasonable injection rates as in standard sandstones, and contains native brine so that pure supercritical CO_2 can be injected. According to this simulation study, a 40 m thick homogeneous formation with a radius of 5000 m is able to achieve an injection of 85 megatons CO_2 in 100 years and mineralization of about 80% injected CO_2 at 1000 years.

There is a trade-off for geochemical trapping of CO_2 between higher reactivity and lower permeability with increasing volcanic rock fragment fractions. The key relationship is between mineralogy and permeability. For Low Permeability, the peak of mineralized CO_2 amount lies at less than 10% VRF, while for slightly higher Permeability, it shifts to around 10-20%. Reactive surface area and residual gas saturation affect the rate of CO_2 sequestration significantly. Sensitivity tests are conducted for these parameters.

Further work is necessary to better constrain the critical parameters that control the rate and extent of carbon mineralization; a direct means to this end would be to conduct experiments with volcanic sandstone samples in supercritical CO_2 saturated brine to measure CO_2 mineralization rates. It would also be beneficial to identify volcanogenic sandstone formations that are suitable for CO_2 sequestration projects and evaluate the sequestration potential of such formation by field characterization. Two such formations that are worthy of study are the Haizume and Tomokomai formations of onshore and offshore Japan, which are being used for CO_2 injection experiments (cf. Mito et al., (2008) ; .Sato et al.,(2009))

Chapter 3 Geochemical Characterization of Volcanogenic Sandstone Samples from the Etchegoin Formation, San Joaquin Basin

3.1 Introduction

Chapter 2 (Zhang et al., 2013) used a hypothetical mineralogy, and parameterizations based on other sandstones to estimate the other pertinent properties needed to evaluate reactive transport in volcanogenic sandstones. In this Chapter, we use samples of real volcanic sandstone, from which we can directly measure many of the parameters, especially mineralogy, porosity, permeability, and mineral specific surface areas. We can also make estimates of residual saturation using the rock properties. Our results suggest that the Zhang et al (2013) conclusions are applicable to natural volcanic sandstone, and that sandstone with about 20% reactive mineral content could cause a large portion of injected CO_2 to be converted to carbonate minerals in less than 1000 years. The content based on this chapter is submitted to the journal of Greenhouse Gases: Science and Technology, titled *CO_2 mineralization in volcanogenic sandstones: geochemical characterization of the Etchegoin Formation, San Joaquin Basin.*

3.2 Previous studies

There have been several efforts to characterize sandstone composition and reactive surface areas of minerals for quantitative prediction of CO_2 injection in the subsurface (Landrot et al., 2012; Peters, 2009). Peters (2009) employed Back-Scattered Electron (BSE) microscopy and energy dispersive X-ray spectroscopy to examine mineral content and to statistically characterize mineral contact with pore space for three Viking sandstones (Alberta sedimentary basin, Canada). Peters (2009) did not identify each mineral type in BSE images, but rather classified them into four general categories: pore space, minerals with mean atomic number less than quartz, quartz, and minerals with mean atomic number greater than quartz, and then determined mineral accessibilities for each category. Randomly selected points on the thin sections were examined with EDX to identify minerals. Quartz, K-feldspar, apatite, oxides, and clay minerals such as kaolinite are found in these samples, but exact abundance and reactive surface area of each mineral are not available. Landrot et al. (2012) used a new characterization approach to measure the surface area of each reactive mineral located within the connected pore network of a sandstone from a carbon sequestration pilot site in Cranfield, Mississippi. The most abundant reactive mineral in this sample is chlorite, which accounts for 8.3% of the total volume, and has a reactive surface area of 0.1162 m^2/g. This number, when combined with the dissolution rate of chlorite measured by Smith et al. (2013) which is about $5x10^{-11}$ $mole/m^2/sec$ at reservoir conditions, is sufficient to allow 575 mole CO_2 mineralization in 1 m^3 chlorite-bearing sands in a timescale of 1000 years given that the rock density is 2800 kg/m^3, 8.3% of the rock is chlorite, and 31.8% of chlorite is accessible (Landrot et al., 2012). On the other hand, assuming 10% of the rock volume is filled with supercritical CO_2 which has a density of 600 kg/m^3, the total amount of CO_2 in 1 m^3 rock is 1364 mole, which means that the released Mg and Fe from chlorite in such sandstones is sufficient to mineralize about half of the stored CO_2 in 1000 years. A laboratory autoclave experiment conducted by Lu et al. (2012) using this reservoir rock and brine samples from the field shows that interactions of CO_2 with the rock-forming minerals are limited, although the sensitivity of their experiments is probably inadequate for evaluating reaction over a 1000 year time scale .

In this chapter we present characterization data from a volcanogenic sandstone member of the Etchegoin formation in the San Joaquin Basin, California. This sandstone is rich in andesitic volcanic lithic grains derived from the Mehrten Formation in the western Sierra Nevada (Lerbekmo, 1957) and the Quien Sabe Volcanic province in the western Diablo Range. The Etchegoin volcanic rock fragments contain reactive minerals such as pyroxenes that are sources of Ca, Mg, and Fe that can combine with CO_2 for mineralization. The volcanic minerals are also the ones that dissolve fastest in the presence of acidic aqueous solutions so that the cations are released into solution on a time scale of hundreds of years. The Etchegoin sandstone is well sorted, moderately- to highly porous, and contains little or no cement or matrix. The injectivity of CO_2 into this formation is likely to be high.

Previous studies have reported summaries of the mineralogy and texture of the Etchegoin sands. Lerbekmo’s (1956) study of the so-called "blue sandstones" of central California includes the blue sandstone of the Etchegoin Group. Based on visual estimates of rocks in thin section, Lerbekmo (1956) listed heavy- and light-mineral assemblages of some sandstones from the Etchegoin Group. Lerbekmo (1957) also discussed optical properties of the montmorillonite cement within the sandstones that gives rise to the distinctive blue coloration, and discussed the genetic relationship and provenance of blue sandstones in central California (Lerbekmo, 1961). Perkins (1987) interpreted the provenance of the Etchegoin Formation in the Sulphur Creek, Coalinga anticline, Waltham Canyon, and Reef Ridge areas, and interpreted the paleogeography of a part of central California from the spatial distribution of heavy-mineral assemblages and framework compositions of Etchegoin sandstones. He divided the framework grains into categories designed to emphasize intra-province provenance, and employed the Glagelov-Chayes point-counting method to estimate mineral percentages (Galehouse, 1967). Link et al.(1990) determined the detrital modes of Etchegoin Formation sandstones occurring in the subsurface in the Kern Front oil field, southern San Joaquin Valley. The main thrust of the study was to characterize the petrology and lithofacies of the Etchegoin Formation, and relate them to the reservoir. Link et al. (1990) used the Gazzi-Dickinson (Dickinson and Snyder, 1979) point-counting method to evaluate the mineralogy of the Etchegoin Formation sandstones.

The above-mentioned petrographic studies contain useful information about the general compositions of the Etchegoin Group sandstones. However, no systematic measurements of mineralogy, porosity, and permeability are available for the same set of samples. Also there is a general lack of information on reactive surface areas for all the measured samples. The goal of this study is to provide comprehensive data that are relevant to CO_2 mineralization in volcanogenic sandstones from this specific site and help in developing more accurate reactive transport models of CO_2 sequestration.

3.3 Geological setting

During late Cenozoic time, the San Joaquin basin of central California was an inland sea that was connected to the Pacific Ocean to the northwest and southwest. The San Joaquin Sea became progressively restricted during the late Neogene due to tectonic and eustatic events, and by the beginning of Pleistocene time, the sea had completely withdrawn from the San Joaquin basin. The Etchegoin Group was deposited in the San Joaquin basin during late Miocene and Pliocene time (-7.0 to -2.2 Ma), and records the late Neogene regressive history of the San Joaquin basin (Loomis, 1990).

The modern San Joaquin Valley of central California forms the southern half of the Great Valley of California, and is bordered by the Coast Ranges to the west, the Sierra Nevada to the east, and the Tehachapi Mountains to the south. The Etchegoin Group is exposed from approximately 15km northwest of Hollister to the southern end of the Kettleman Hills in central California. The Etchegoin Group also occurs in the subsurface in the central and southern San Joaquin Valley (AAPG, 1957). The San Joaquin Valley is an asymmetric structural trough that is filled with a prism of upper Mesozoic and Cenozoic sedimentary rocks that attains a thickness of over 9000 meters in the west-central and southern part of the San Joaquin Valley (Bartow, 1987). The Etchegoin Group forms the upper part of the fill of the San Joaquin Valley, and although the thickness of the Etchegoin Group exposed at the surface is variable, it reaches a maximum of about 2500m in the Big Tar Canyon area.

The Etchegoin Group (Jacalitos Formation, Etchegoin Formation, and San Joaquin Formation from bottom to top) consists of siltstone, sandstone, conglomerate, and rare tuff beds. The sediments making up these rocks were deposited in shallow-marine, marginal- marine, and non-marine environments during the late Neogene regression of the San Joaquin Sea. Shallow-marine facies are dominant in the west-central outcrop belt, where the Etchegoin Group rests conformably on the upper Miocene Reef Ridge Shale. Non-marine facies of the Etchegoin Group occur along the flanks of the Diablo Range in the Priest Valley and Coalinga anticline regions, where the section rests unconformably on Jurassic, Cretaceous, and upper Miocene rocks (Dibblee, 1971). Along the northern, eastern, and southern margins of the San Joaquin basin, the Etchegoin Group occurs in the subsurface, and grades laterally into non-marine strata of the Laguna and Kern River Formations (Bartow, 1987; Foss, 1972).

The Etchegoin Formation is primarily composed of brown silty sandstone and pebbly sandstone, and gray or blue medium-grained to pebbly sandstone. The pebbles are dominantly volcanic (andesitic) in composition, with lesser amounts of sedimentary (siltstone) clasts, and metasedimentary (mica schist) clasts. The thickness of the Etchegoin Formation varies from 1034 to 1672 meters, reaching a maximum thickness in the Zapato Chino Canyon area. Arnold and Anderson (1910) designated Coalinga anticline as the type locality of the Etchegoin Formation.

A time-transgressive blue sandstone facies extends locally from the base of the Etchegoin Formation to the top of the San Joaquin Formation. This facies consists of fine- to coarse-grained to pebbly, cross-stratified blue sandstone that is rich in andesitic volcanic lithic grains. The andesitic detritus was most likely derived from two sources: the Mehrten Formation in the western Sierra Nevada, and the Quien Sabe volcanic province in the western Diablo Range (Lerbekmo, 1956, 1961). The montmorillonite-rich cement within the blue sandstone is derived from the weathering of the andesitic rock fragments, and gives the sandstone its distinctive color (Lerbekmo, 1957). The textural maturity of the blue sandstones (i.e., moderate to well sorted, high porosity, no matrix) is a result of having been reworked, and the fine-grained sediment fraction having been winnowed away, in moderate- to high- energy settings, such as channels and shoals within an estuarine depositional system

The channel deposits are typically lenticular and are separated laterally and vertically by impermeable, fine-grained sedimentary deposits formed in subtidal- to intertidal-flat environments, creating effective seals. Many of these lenticular sandstone units were most likely deformed during the late Pliocene and Pleistocene growth of anticlinal structures in the western San Joaquin Valley (Harding, 1976; Namson and Davis, 1988; Wentworth and Zoback, 1989), thus forming sandstone reservoirs that pinch out into siltstone and shale in an up-dip direction.

3.4 Methods of sampling and sample preparation

Samples of Etchegoin Sandstone were collected from five outcrop locations (Figure 3.1 labeled as ESZ1 to ESZ5). Several other samples were also collected from other formations containing volcanic detritus for comparison, labeled as GVZ1 to GVZ2 (Great Valley) and CSZ1 (Cretaceous). Generally the sandstones from the Etchegoin Formation are gray or blue, medium-grained to pebbly. Pictures of the outcrops and one hand sample are shown in Figure 3.2. Standard petrographic thin sections were cut from the samples. The friable sandstone samples were impregnated with epoxy prior to cutting. Core plugs were also made from the samples to measure porosity and permeability.

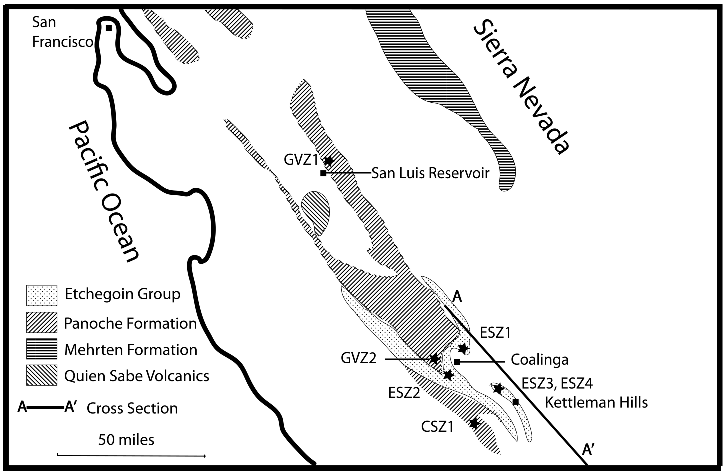

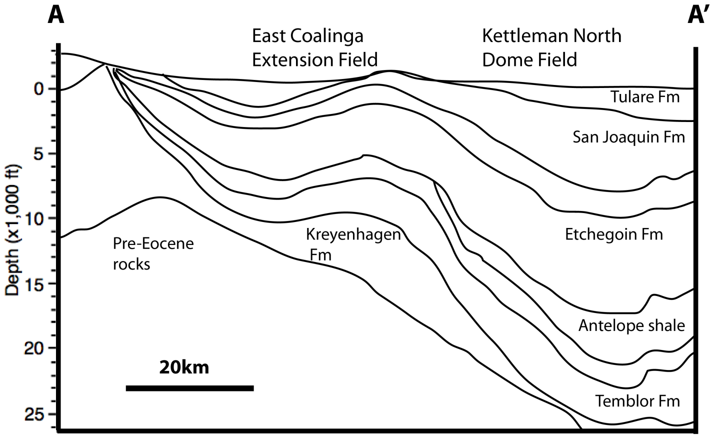

Figure 3.1 Locations of the outcrop samples collected from San Joaquin Basin on a geological map of central California, and a cross section of the Etchegoin formation in the overall sedimentary basin stratigraphy. The locations of Coalinga and Kettleman Hills where the samples are collected are included. The volcanic rock fragments are derived from the Mehrten Formation and Quien Sabe volcanics.

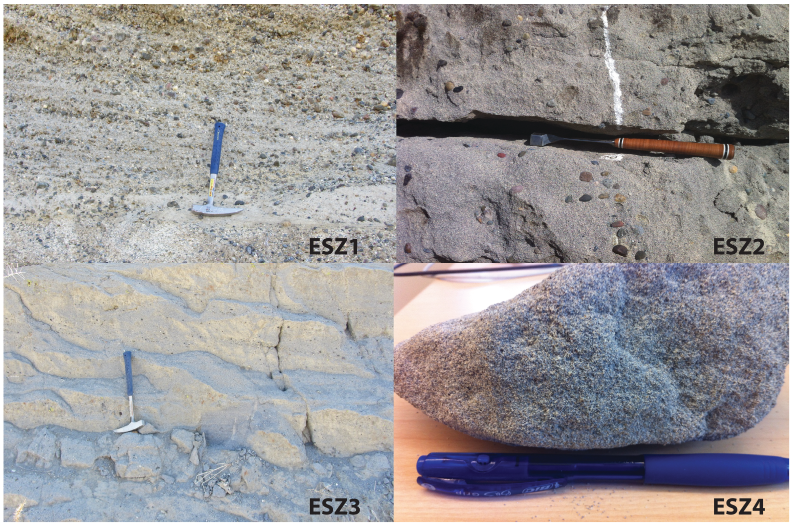

Figure 3.2 Photos of Etchegoin Formation outcrops and a hand sample. Generally the sandstones are gray or blue, medium-grained to pebbly. The blue color is from the montmorillonite cement in the sandstone.

3.5 Permeability and porosity

Permeabilities were measured using a pressure vessel, through which helium gas flowed. A helium gas tank was used to control flow during permeability measurements. The tank was set to provide constant gas pressure (typically about 15 psi) and provide a series of constant flow rates (0.1 to 10 mL/min). Each gas pressure was imposed and maintained until the system achieved a steady state, defined as the pressure differential across the sample reaching a fairly constant value for more than 60 seconds (three consecutive similar readings at 20-second intervals). At least three gas pressures were used in each permeability measurement. Permeability was calculated for each gas pressure, and the averages of these permeabilities are presented in Figure 3.3.

Porosity was measured using the Boyle's Law Method, a gas transfer technique that involves the expansion of gas from the pores of a clean dry sample (Klinkenberg, 1941; Monicard, 1980). Boyle's law states that the volume of a gas varies inversely with pressure under isothermal conditions. The rock sample is placed in the sample chamber at zero gauge pressure and the reference chamber is filled with gas at pressure P_1, then the valve between the two chambers is open and the system is brought to equilibrium. The number of moles of gas remains constant. The solid volume of the sample is calculated using Boyle's Law:

$$P_1 V_{Ref} = P_2 (V_{Ref} + V_{Sam} - V_S)$$

Where V_S is the volume of solids in the rock, V_{Ref} is the volume of the reference chamber, V_{Sam} is the volume of the sample chamber, P_1 is the pressure before opening the valve, and P_2 is the pressure at equilibrium after opening the valve. The solid volume is then subtracted from the bulk volume, measured directly using a caliper, to arrive at the pore volume.

Measured porosities range from 13% to 35%, and permeabilities are 0.02 Darcy to several Darcy (Figure 3.3). Permeability does not depend on pore fluid, therefore permeability measured by gas should be the same as that measure by water. For incompressible media, the linear form of Darcy's Law can be applied.

$$Q/A=k(P_{up}-P_{down})/\eta L$$

Where Q is the volume of fluid measured per unit time, A is the cross section area of the sample, η is the viscosity of the pore fuild, L is the sample length, and P_{up} and P_{down} are pore pressure of the upper and lower ends of the specimen respectively. However, when compressible gas (PV=constant) is used as pore fluid, the average gas permeability k_{gas} is expressed as the following:

$$Q/A= k_{gas}(P_{up}^2-P_{down}^2)/2\eta L P_{down}$$

Therefore, the corrected equation was used to calculate permeability for nitrogen gas in our experiment. It has been argued that permeability to gas is relatively higher than that to water related to the Klinkenberg effect (Klinkenberg, 1941). This is due to the gas slippage phenomenon which is a non-Darcy effect associated with non-laminar gas flow in porous media. This effect occurs when the size of the average rock pore throat radius approaches the size of the mean free path of the gas molecules, thus causing the velocity of individual gas molecules to accelerate or "slip" when contacting rock surfaces. This phenomenon is only significant in tight gas sands that are typically characterized by very small pore throats and when permeability is lower than 10^{-6} darcy and at low differential pore pressures. Since the samples in this study are sandstones with high permeabilities, the Klinkenberg effect is not taken into account for permeability estimation.

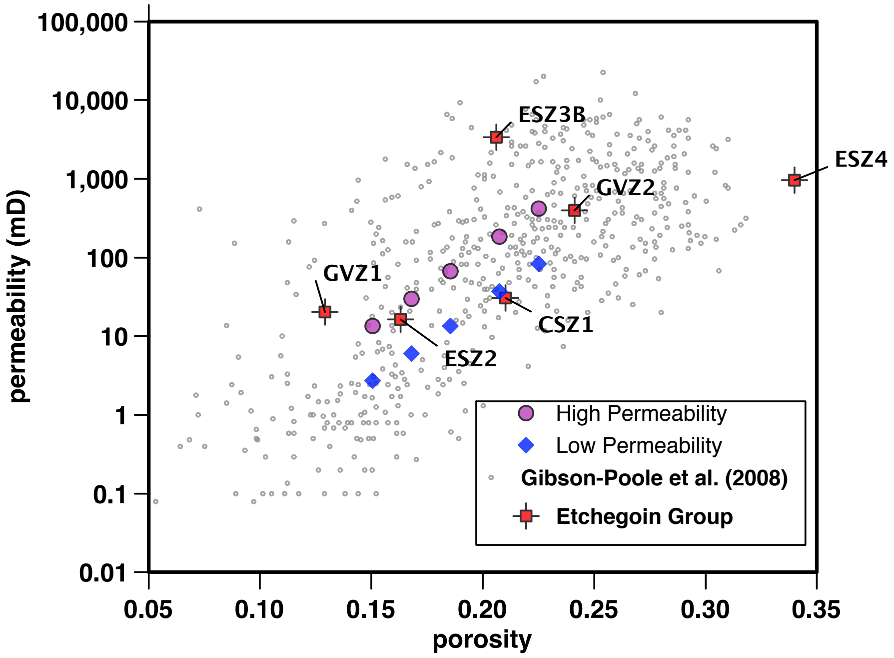

Figure 3.3 Porosity and permeability measurements of core plug samples. The Etchegoin samples all have high porosities from 18%-34%, and high permeabilities from 20 mD to several darcy. The cretaceous samples from the Panoche formation has relatively lower porosities and permeabilities, but can also be as high as 24% and 0.5 darcy.

3.5.2 Mineralogy and reactive surface area determinations

Larger mineral grains of plagioclase, quartz, K-feldspar, amphibole, and pyroxenes can be identified from optical properties. Volcanic fragments are prevalent in thin sections, but the exact mineralogical composition of the fragments cannot be determined under the microscope due to the very fine grain size. We are able to convert the volcanic rock fragment grains into specific minerals by systematic use of electron microprobe and X-ray diffraction data. Elemental abundances of sample ESZ3B and ESZ4 using Electron microprobe analyser (EMPA) are listed in Table 3.1 and Table 3.2. The sum of Fe, Ca and Mg add up to 17%-19%. X-Ray Powder Diffraction (XRPD) analysis of sample ESZ3C is shown in Figure 3.4 and results of mineral identifications and abundances are shown in Table 3.3. Reactive minerals in sample ESZ3C include clinopyroxene (9.1%), amphibole (2.4%), chlorite (1.9%), and Fe-spinel (magnetite, traces, <<1%). A thin section made from sample ESZ4 was analyzed by Scanning Electron Microscope (SEM), in the Earth Science Division, Lawrence Berkeley National Lab. Backscattered Electron Microscope (BSE) images were collected (Figure 3.5). Chemical analyses with an Energy Dispersive X-ray Spectroscopy (EDX) detector were performed within the same region of the sample. Elemental distribution maps from EDX analyses are shown in Figure 3.6.

Table 3.1 Elemental abundances of sample ESZ4 from EMPA analysis

SiO_2	Al_2O_3	Na_2O	K_2O	FeO	MgO	CaO	MnO	TiO_2
66.59	13.09	2.72	0.35	5.51	6.97	4.98	0.22	0.14

Table 3.2 Elemental abundances of sample ESZ3B from EMPA analysis

SiO_2	Al_2O_3	Na_2O	K_2O	FeO	MgO	CaO	MnO	TiO_2
58.4	18.1	3.9	0.5	6.7	5.2	7.1	0.1	0.5

Table 3.3 Weight percent of minerals in sample ESZ3C from XRPD analysis

Mineral	Weight%
Labradorite	8.2
Andesine	60.4
Chlorite	1.9
Quartz	13.2
Amphibole	2.4
Clinopyroxene	9.1
K-Feldspar	2.8
Cristobalite	2.0
Fe-Spinel	<<1%

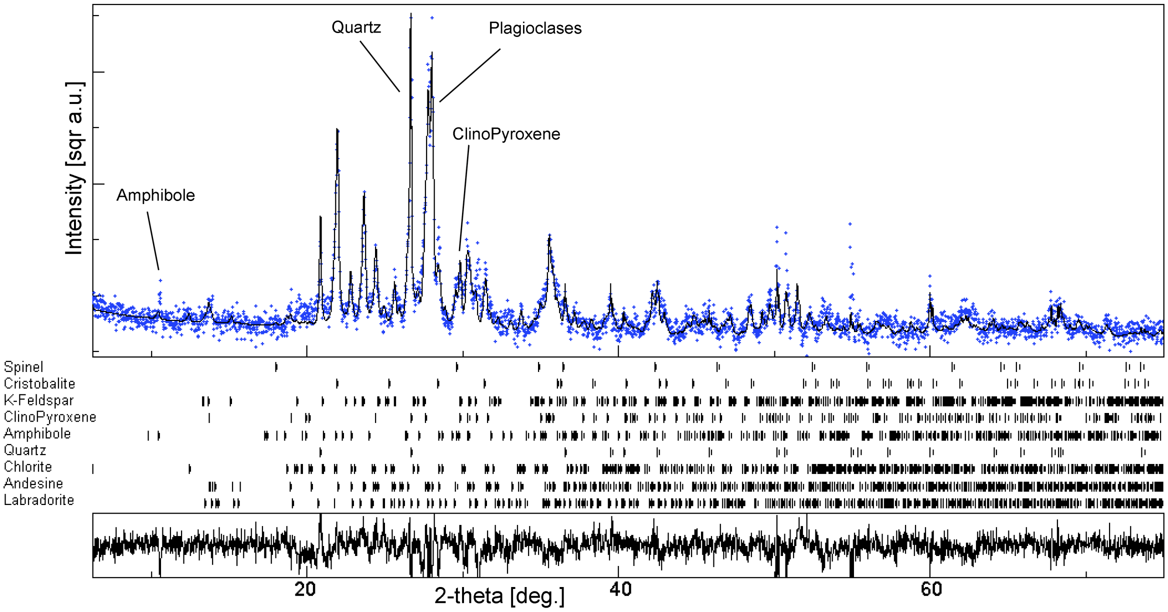

Figure 3.4 Spectrum from XRPD analysis of sample ESZ3C and matching with mineral spectrums. The minerals that fit the profile are spinel, cristobalite, K-feldspar, clinoPyroxene, amphibole, quartz, chlorite, andesine, and labradorite.

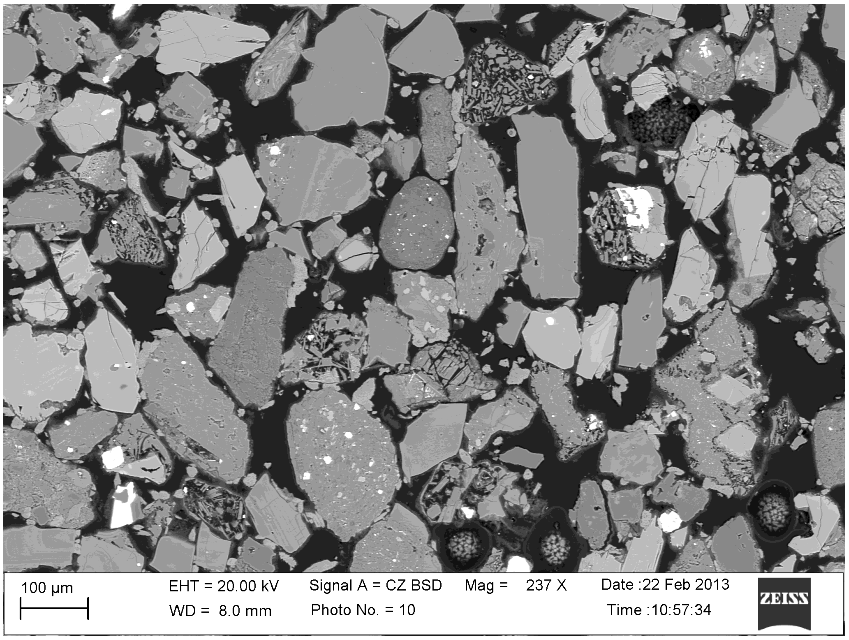

Figure 3.5 Scanning Electron Microscope (SEM) image of sample ESZ4. Some minerals can be identified from texture, but composition information is needed for other minerals and the mixed grains.

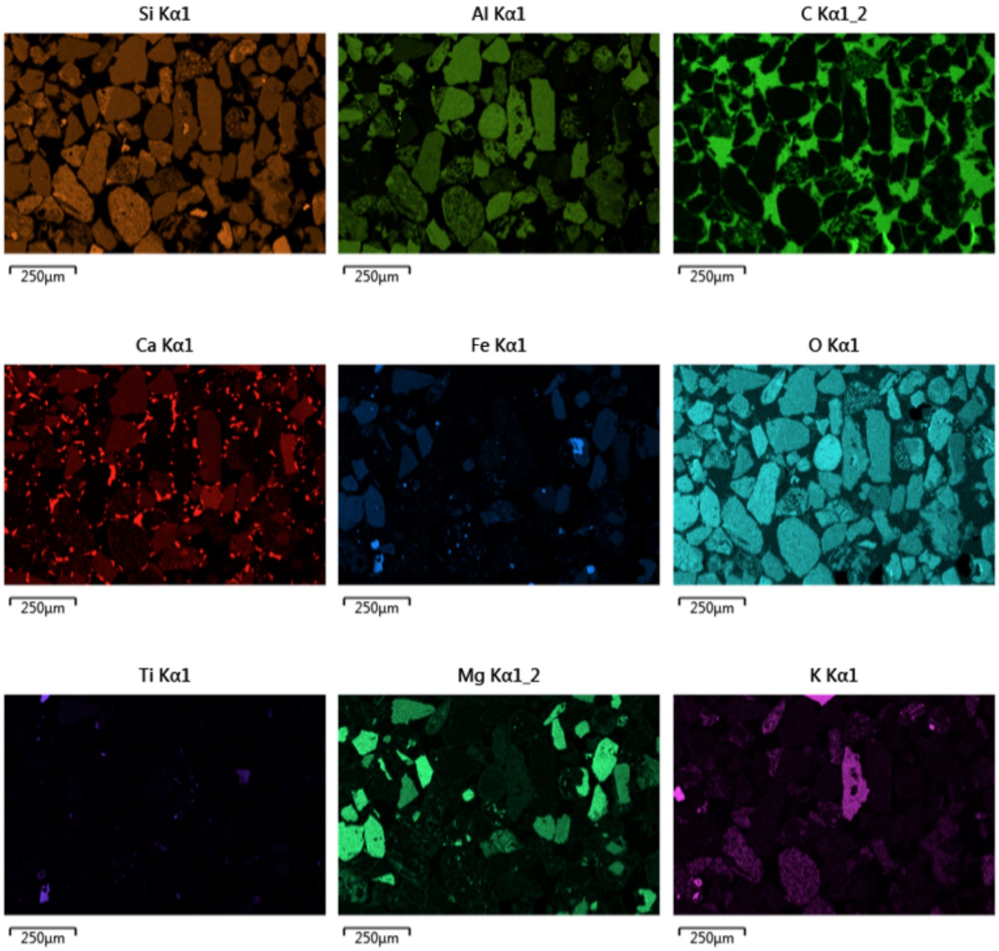

Figure 3.6 Elemental distribution maps of the SEM picture from chemical analyses with an Energy Dispersive X-ray Spectroscopy (EDX) detector

To measure reactive surface area of each mineral, a mineral distribution map is required. Such a mineral map can be generated by combining the elemental maps. A pixel contrast intensity thresholding technique was employed to convert the elemental distribution images from a gray scale format (with pixel values ranging from 0 to 255) to a binary format (with pixel values equal to 0 or 1). A contrast intensity value was chosen as a threshold for each elemental distribution image, which sorts all the pixels into two categories, pixels with intensities larger than the threshold that indicate the existence of this element, and pixels with intensities smaller than the threshold that should be considered as those corresponding to the background level of this element. The determination of the threshold required first considering a set of contrast intensity values in the histogram of the element images, where the pixels corresponding to the element in minerals and those corresponding to the element in the background cross each other. The threshold value to be determined is thus one of the contrast intensity values featured in this region of the histogram. Since the threshold's value determines the number of pixels that are classified in the two categories, the objective is to minimize errors in misclassification, which is to find where changes in the intensity threshold have the least effect on the values of $N_{categoryA}$ and $N_{categoryB}$, where $N_{categoryA}$ and $N_{categoryB}$ refer to the number of pixels in category A and B. The mathematical representation is to find the minimum of the normalized differential changes in each of $N_{categoryA}$ and $N_{categoryB}$ shown in the following equation, where I is the contrast intensity threshold.

$$\frac{1}{N_{categoryA}}\left|\frac{dN_{categoryA}}{dI}\right|+\frac{1}{N_{categoryB}}\left|\frac{dN_{categoryB}}{dI}\right|$$

The result of this equation was calculated after separating category A and B by each contrast intensity. The desired threshold is determined by looking for the contrast intensity that gives the lowest result. All pixels in the images that have a contrast intensity above this threshold indicate that there is this element at this location, and are assigned a value of "1" to the new binary image. All pixels in the elemental images with a contrast intensity equal or below the threshold value correspond to the background element level and are assigned a "0" value in the processed images. The same pixel contrast intensity thresholding approach was employed for all the elemental maps, including the carbon distribution map. The carbon element in the thin section is from the epoxy that the sample was embedded in and only distributes in the pore spaces. Thus the carbon element distribution image is essentially a map of pore space distribution.

From point analysis of EDX, plagioclase, K-feldspar, clinopyroxene, orthopyroxene, quartz, calcite and ilmenite are identified in the thin section. Whether a mineral is present or not at the location of a certain pixel is determined from the elemental maps. Every mineral possesses a certain package of elemental components, which are shown in Table 3.4. The symbol "+" indicates that an element is present in this mineral, while "-" indicates that it isn't. So the mineral distribution is obtained by integrating the element maps marked by "+" and subtracting the element maps marked by "-", and is shown in Table 3.4 .

Volume fraction of each mineral phase is determined by counting the number of pixels of each mineral in Figure 3.7 and divide by the total number of pixels in the image. Surface area of each mineral is determined by measuring the perimeter of each mineral in the 2D map. Then the surface area density in 3D is calculated by multiplying the perimeter density in 2D by $4/\pi$. This is justified by Weibel (1981) that for randomly positioned 2D sections through an isotropic medium, area fractions in 2D image are representative of the volume fractions in 3D, while the 3D surface area density for objects in that medium is on average equal to the objects' perimeter density multiplied by $4/\pi$.

The most reactive minerals in this sandstone are orthopyroxene, clinopyroxene, and ilmenite, which have volume fractions of 10.29%, 2.27% and 1.03% respectively. The surface areas are all around 1 m^2/kg mineral. Reaction kinetics of these minerals are available in the literature. With this information, it is possible to conduct model kinetic geochemical calculations of CO_2 mineralization in this sandstone.

Table 3.4 Elemental assemblages in minerals

	Si	Al	Na	Ca	K	Fe	Mg	Ti
Quartz	+	-	-	-	-	-	-	-
Plagioclase	+	+	+	+	-	-	-	-
K-feldspar	+	+	-	-	+	-	-	-
Orthopyroxene	+	-	-	-	-	+	+	-
Clinopyroxene	+	-	-	+	-	+	+	-
Ilmenite	-	-	-	-	-	+	-	+
Calcite	-	-	-	+	-	-	-	-

Table 3.5 Volume fraction and reactive surface area of each mineral in sample ESZ4 calculated from Figure 3.7

	Volume fraction (%)	Surface area (m^2/kg)
Quartz	12.90	0.86
Plagioclase	32.01	1.33
K-feldspar	13.94	1.11
Orthopyroxene	10.29	0.69
Clinopyroxene	2.27	1.62
Ilmenite	1.03	0.91
Calcite	5.13	1.65
Porosity	19.62	N/A
Total	97.18	N/A

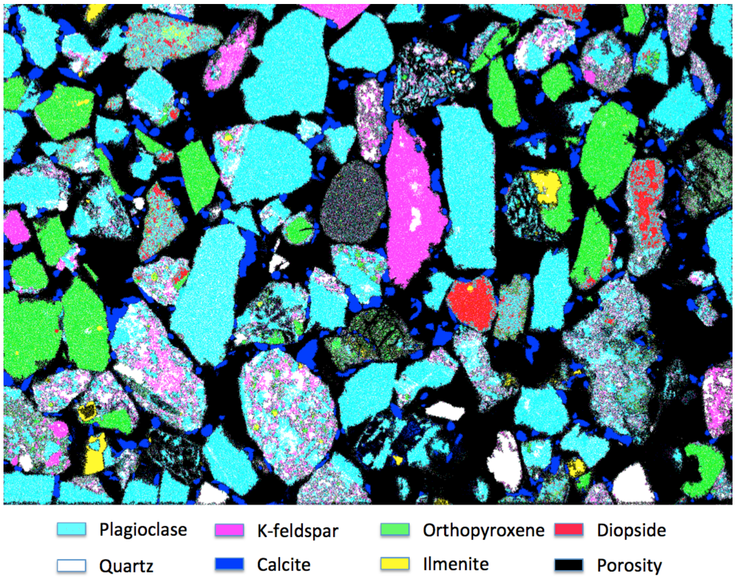

Figure 3.7 Mineral distribution map of the SEM picture by combining the elemental maps in Figure 3.7

3.6 Implications for CO_2 mineralization

3.6.1 Calculation of CO_2 mineralization in Etchegoin sandstone

Zhang et al. (2013) showed that, assuming standard first-order kinetics, with 10-20% volume fraction of reactive, divalent cation-bearing minerals, a 40m-thick homogeneous formation with a radius of 5000 m could accommodate injection of 85 megatons of supercritical CO_2 through a single well in 100 years, with 77 percent of the injected CO_2 being converted to carbonate minerals within 1000 years. That conclusion was based on a model mineralogy and a hypothetical reactive surface area of 1 m^2/kg. In this study, we have shown that the sandstones from the Etchegoin Formation have approximately 10% orthopyroxene, 2.3% clinopyroxene, and 1% ilmenite, which is similar to the reactive mineralogy used for the modeling work of Zhang et al. (2013). The measured reactive surface areas for orthopyroxene, clinopyroxene and ilmenite are 0.69, 1.62, and 0.91 m^2/kg respectively. Using the geochemical information from the current study, reactive transport modeling was conducted to calculate the potential for CO_2 mineralization using the same hydrological model as in Zhang et al. (2013).

The other significant parameters for the reactive transport modeling are porosity and permeability. The average porosity of the measured Etchegoin samples is as high as 24.2%, and the average permeability is 2.19 darcy, which is 100 times larger than used by Zhang et al. (2013). These higher numbers are employed in the model, with a fixed injection rate of CO_2 at 0.85 Mton per year for a hundred years. Simulation was conducted for 1000 years. Details about the model setup is available in Zhang et al. (2013).

Figure 3.8 shows the amount of CO_2 in each phase from reactive transport modeling using the geochemical information obtained in this study. In the model, 85 megatons of supercritical CO_2 is injected through a single well in 100 years, and 92% of the injected CO_2 is converted to carbonate minerals at 1000 years. Most of the mineralization occurs in the first 500 years. Figure 3.9 suggests that the CO_2 affected region is limited to a radial distance of about 4500m, which is close to the result of Zhang et al. (2013) using a model with a much lower permeability. This result indicates that the radial distance of CO_2 flow is not affected extensively by permeability when CO_2 injection rate is fixed. Gas saturation is high close to the CO_2 injection well.

Compared to the model of Zhang et al. (2013), in the current model there are more reactive minerals (mainly pyroxenes), which provides more Ca, Mg and Fe to the aqueous phase. Consequently, there is more precipitation of ankerite ($CaMg_{0.3}Fe_{0.7}CO_3$) in the current model (4% volume fraction change compared to 1% in the previous model). The extensive precipitation of ankerite consumes a large amount of Ca and CO_3^{2-}, making the saturation index of calcite negative. Calcite dissolves in the current model instead of precipitating as it did in the Zhang et al (2013) model.

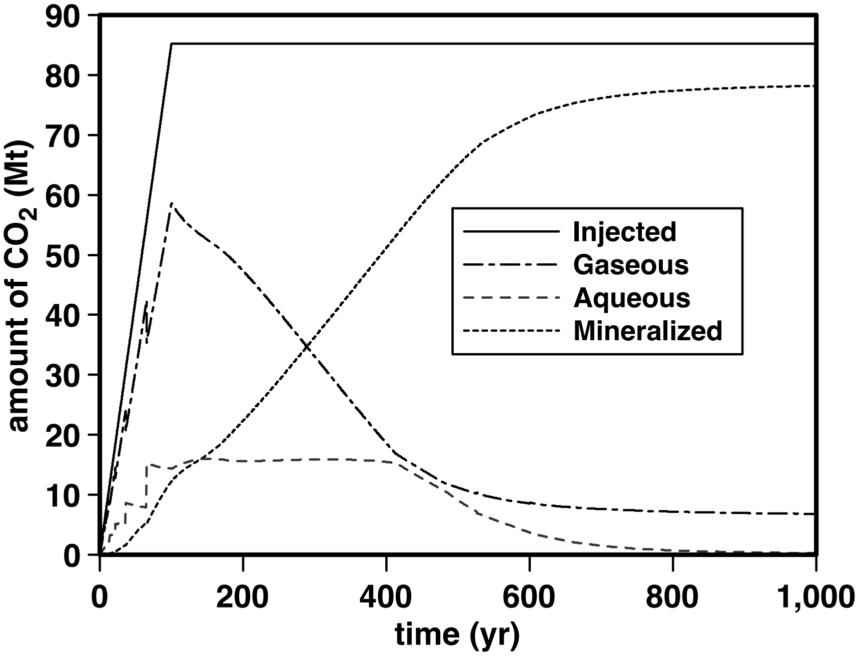

Figure 3.8 Cumulative CO_2 injection and CO_2 mass in different phases calculated by reactive transport code TOUGHREACT using the geochemical and hydrological information from the Etchegoin samples. 92% of injected CO_2 is predicted to be mineralized in 1000 years.

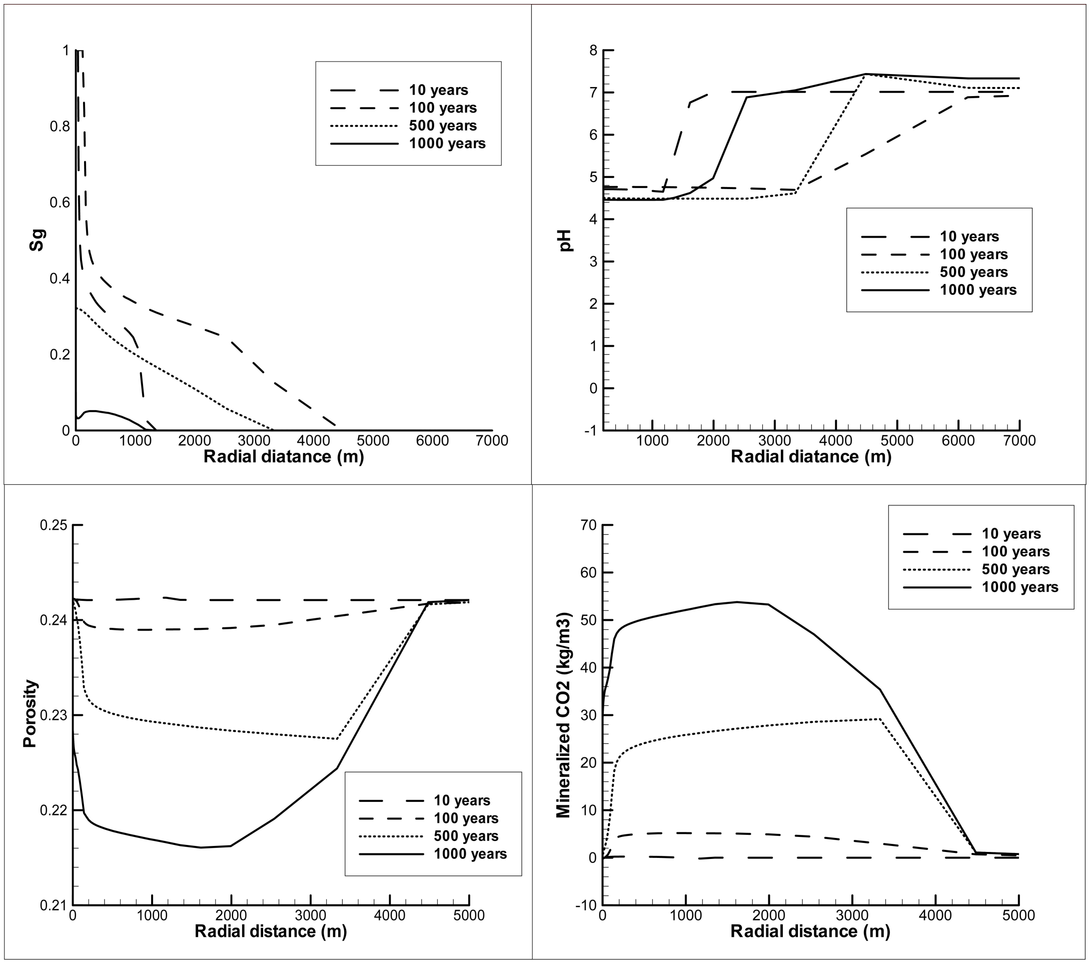

Figure 3.9 Radial distribution of gas saturation, pH, porosity, and mineralized CO_2 per cubic meter of reservoir medium from 10 years to 1000 years. The CO_2-affected region is roughly 5000 meters, within which the parameters are different from background values.

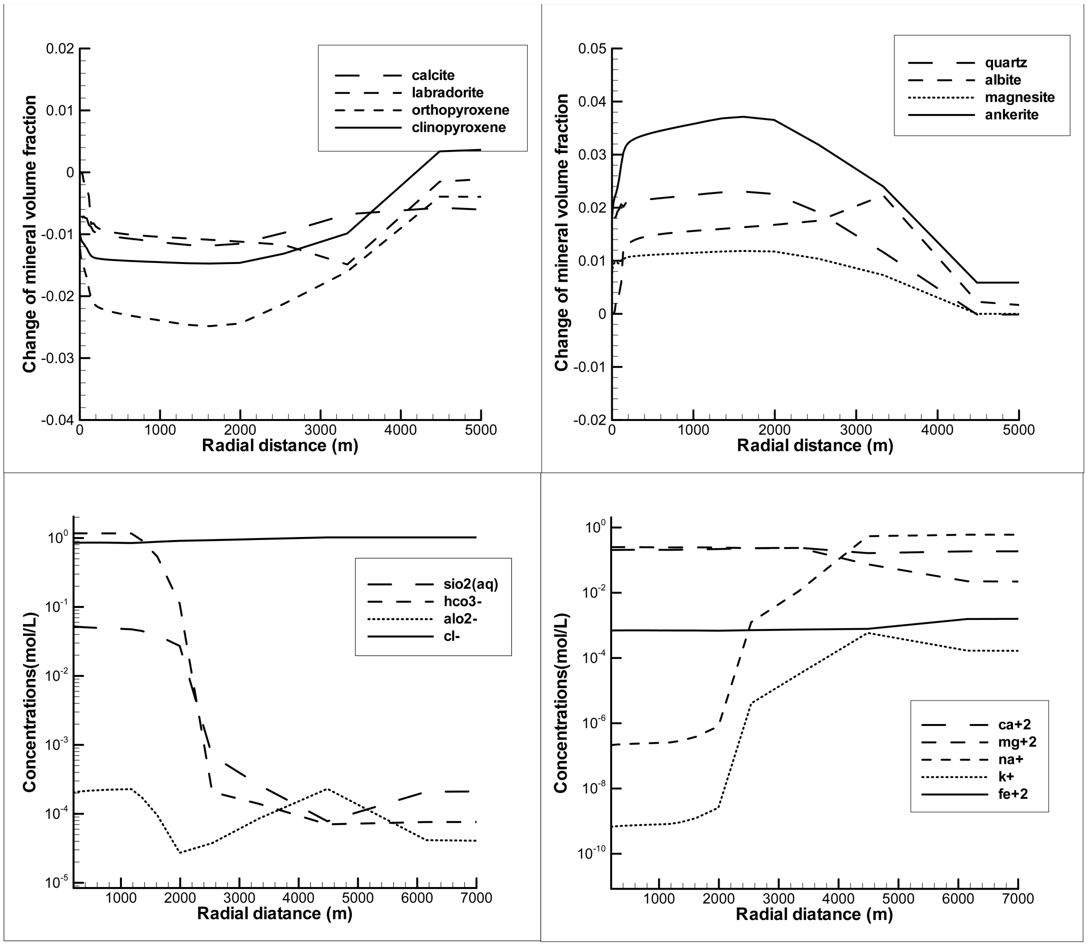

Figure 3.10 Radial distribution of aqueous concentrations and change of mineral volume fractions at 1000 years from reactive transport modeling. Calcite, plagioclase, and pyroxenes dissolve, while ankerite, magnesite, albite and quartz precipitate. The concentrations of K^+ and Na^+ decrease, while the concentrations of HCO_3^-, Ca^{2+}, Mg^{2+}, and $SiO_2(aq)$ all increase in the CO_2-affected region.

3.6.2 Effects of heterogeneity on CO_2 mineralization

Formation heterogeneity might increase or decrease mineralization. To study the effects of heterogeneity on CO_2 injection and mineralization, we conducted simulations using layered models with different permeability values for each layer to simulate different degrees of heterogeneity.

Permeability values of each layer are assumed to follow a log normal distribution, with average log permeability μ equal to 1.8. That is, the permeability is $10^{1.8}$ mD if standard deviation σ is zero (no heterogeneity). The value of the standard deviation of the normal distribution describes the degree of heterogeneity. Larger standard deviation values indicate larger variation of permeability. Values of 0, 0.1, 0.3 and 0.5 are used for the standard deviation of log permeability(Figure 3.11). The 40-meter thick (reservoir formation) model domain is divided into 40 layers vertically, with a thickness of 1 meter per layer. 40 random permeability values are generated for each layer based on the provided log normal distribution. As a result, the log normal distribution with large standard deviation (0.5) has a wider distribution of permeability values than that with a smaller standard deviation (0.1), and thus a larger degree of heterogeneity.

VRF% are calculated for each permeability layer using the relationship between VRF% and permeability in Zhang et al. (2013).

$$\text{Log Permeability} = 2.542 - 0.0342 \times \text{VRF\%}$$

According to this equation, the amount of volcanic rock fragments decreases with increasing permeability. In some cases, for example when standard deviation=0.5 as shown in Figure 3.11, log permeability is larger than 2.542 for some layers, so VRF% would end up smaller than zero. The VRF% values are assigned zero in these cases. Since the amounts of reactive minerals in volcanic rock fragments (18.47% orthopyroxene, and 16.54% clinopyroxene) are proportional to VRF%, reactivity of the formation layer also changes inversely with permeability. Figure 3.13 and Figure 3.14 show examples of permeability and VRF% distribution along the vertical direction for $\sigma = 0.5$.

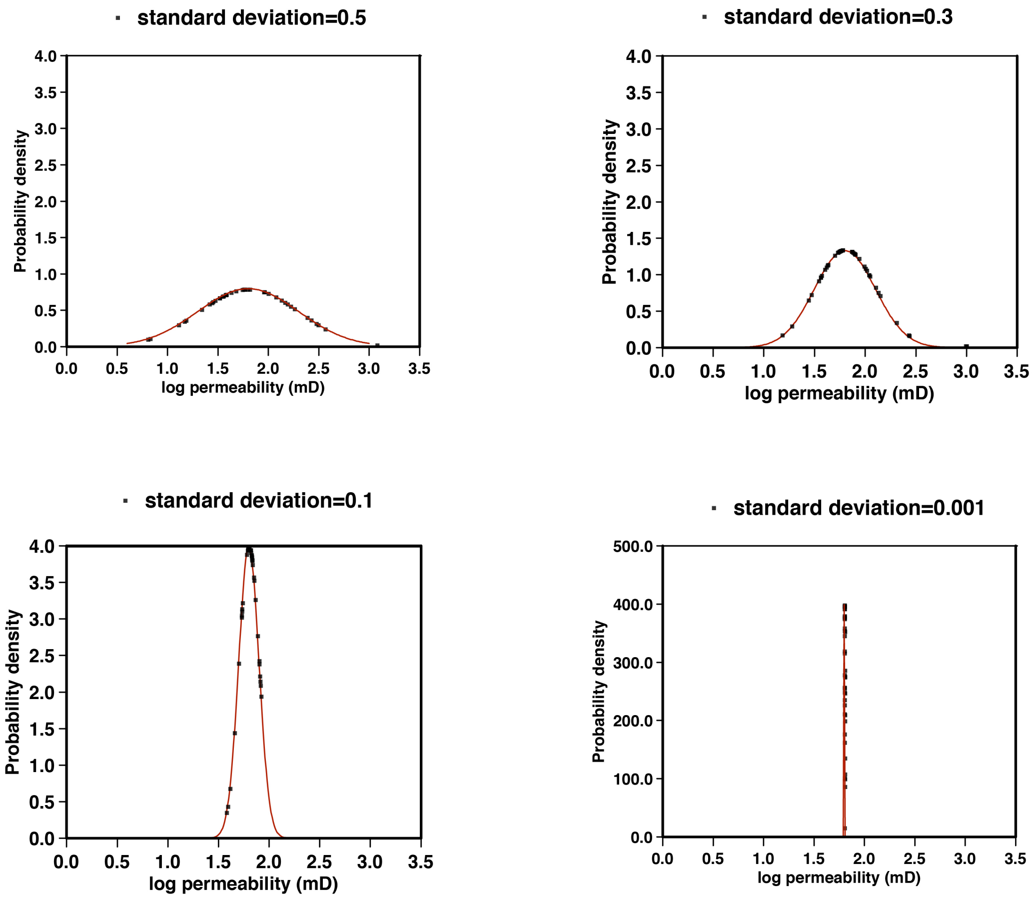

Figure 3.11 Log normal distributions of permeabilities and random permeability values generated based on respective distributions. The permeability sets with larger standard deviation have wider distribution of permeability values, and represent larger heterogeneity.

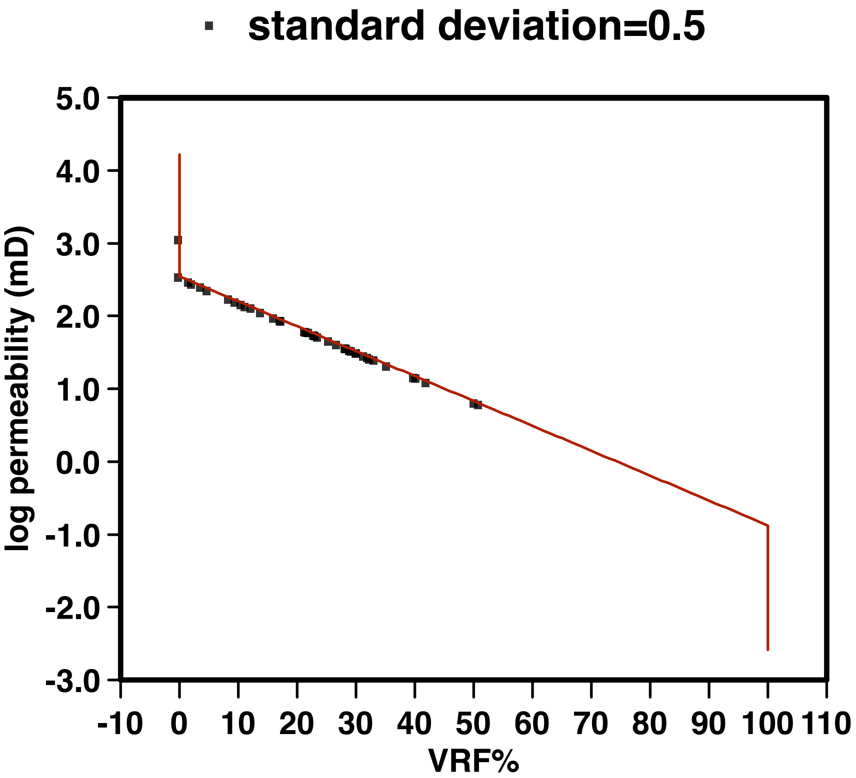

Figure 3.12 Relationship between log permeability and VRF% from Zhang et al. (2013), and the VRF values calculated from permeability based on this relationship for the σ=0.5 case. Permeability decreases with increasing VRF due to more intense compaction and chemical reactions during diagenetic history.

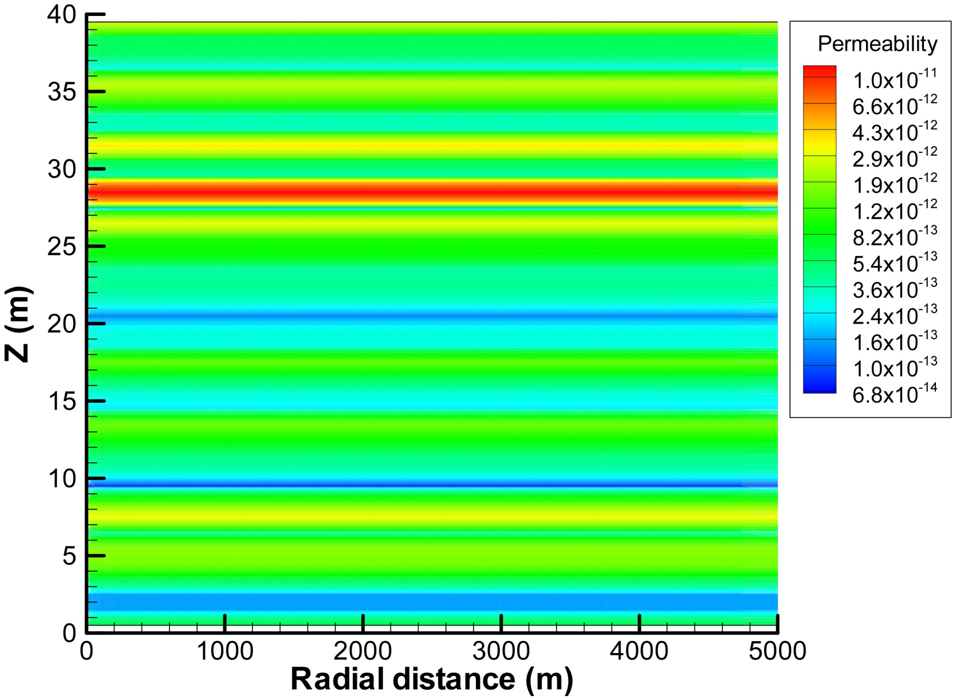

Figure 3.13 Permeability distribution along the thickness of formation in the case of standard deviation=0.5

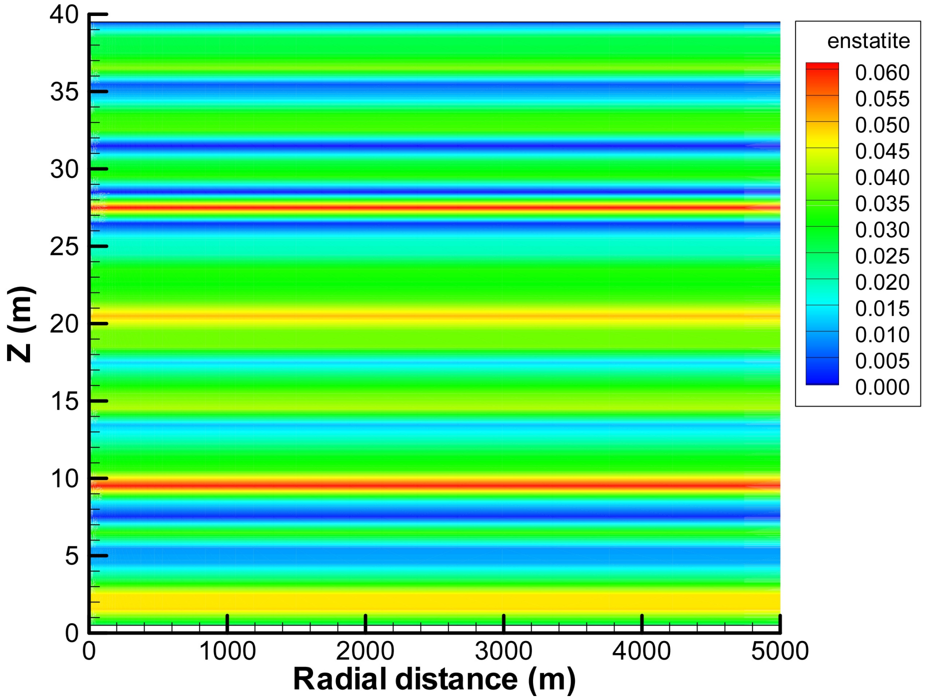

Figure 3.14 VRF distribution along the thickness of formation (represented by the amount of enstatite) in the case of standard deviation=0.5

Figure 3.15 shows the result of injected CO_2, mineralized CO_2 at 10 years, the fraction of CO_2 mineralization and effective permeability as a function of standard deviation. The amount of injected CO_2 increases with increasing standard deviation because the high permeability zones enhance the injectivity and allow more CO_2 to be injected into the formation. For the parallel-layered beds used in the current model, the effective permeability is the weighted-average permeability of all layers. Although all the cases share the same average log permeability, the weighted-average of absolute permeability changes with the standard deviation of the log normal distribution. In fact, the average of the absolute values increases with increasing standard deviation of the log normal distribution. The average permeability for $\sigma=0.5$ is about 100% larger than that for $\sigma=0$ (homogeneous), thus roughly twice amount of CO_2 is injected into the formation in the $\sigma=0.5$ case.

The amount of mineralized CO_2 also increases with increasing heterogeneity. Although in the early stages of system evolution there is some separation of CO_2 from reactive minerals, the CO_2 is not effectively kept away from the reactive minerals due to buoyant upward flow of CO_2. Thus, the low pH conditions in the high-permeability zones are able to penetrate the low permeability zones regardless of the lengthscale of vertical heterogeneity. Figure 3.16 shows the 2D distribution maps of gas saturation, pH, mineral dissolution and precipitation. The largest horizontal flow occurs where permeability is largest, between 28m to 29m vertical coordinate in the example. Mineral dissolution and precipitation is most extensive one layer below, between 27m to 28m, where permeability happens to be lowest, and thus reactivity is highest. There is dissolution of mineral in this reactive layer even though there is virtually no flow affecting that layer. This result clearly shows the effect of diffusion from the permeable layer above that provides CO_2 and/or H^+ for mineral dissolution. Overall, the effect of heterogeneity not only increases CO_2 injectivity, but also the amount of CO_2 mineralization.

The simulations described here were run for only 10 years of simulated time, but since the CO_2 injection and mineralization rate is close to linear over the first several hundred years during and after injection, the conclustions are not expected to change for longer time scales. To summarize, the homogeneous case has a single permeability of $10^{1.8} = 63.1$ mD, while the most heterogeneous case (σ=0.5) has permeabilities of 40 layers ranging from $10^{0.87}$-$10^{3.02}$ mD (7.4md- 1037mD). This vertical heterogeneity of permeability increases the average permeability by about 95% and thus the amount of injected CO_2 also increases by 95%. The amount of mineralized CO_2 increases by 160% because more CO_2 is injected into the formation, and also because there are effectively more reactive minerals in the heterogeneous case, and the diffusion and buoyant flow is effective at exposing the reactive minerals to the CO_2 (and/or H^+).

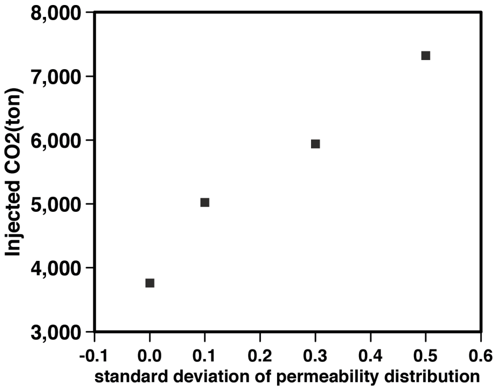

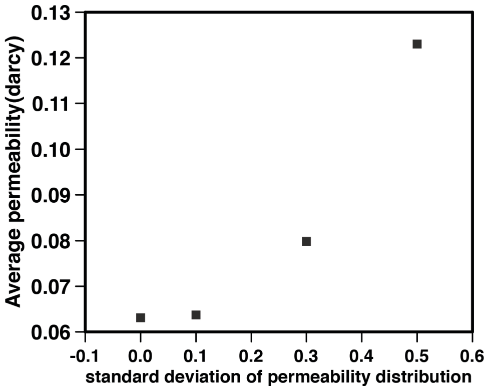

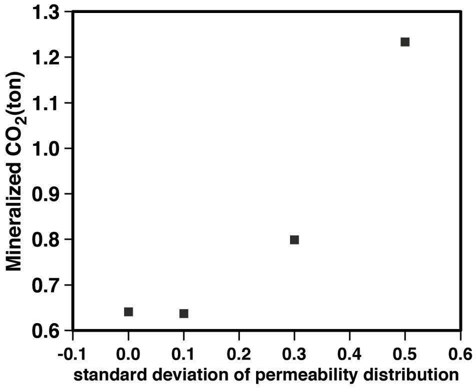

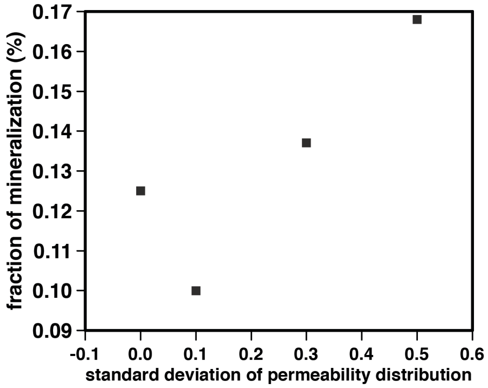

Figure 3.15 The amount of injected CO_2, mineralized CO_2 at 10 years, average permeability and fraction of CO_2 mineralization as a function of standard deviation of log permeability distribution. The homogeneous case (σ=0) has a single permeability of 101.8 = 63.1 mD, while the most heterogeneous case (σ=0.5) has permeabilities of 40 layers ranging from $10^{0.87}$-$10^{3.02}$ mD (7.4md-1037mD). This vertical heterogeneity of permeability increases the average permeability by about 95% and thus the amount of injected CO_2 also increases by 95%. The amount of mineralized CO_2 increases by 160% which is partly because more CO_2 is injected into the formation, and also because that there is effectively more reactive minerals in the heterogeneous case, and the diffusion of chemical species mixes reactive minerals in the reservoir with CO_2 (and or H^+).

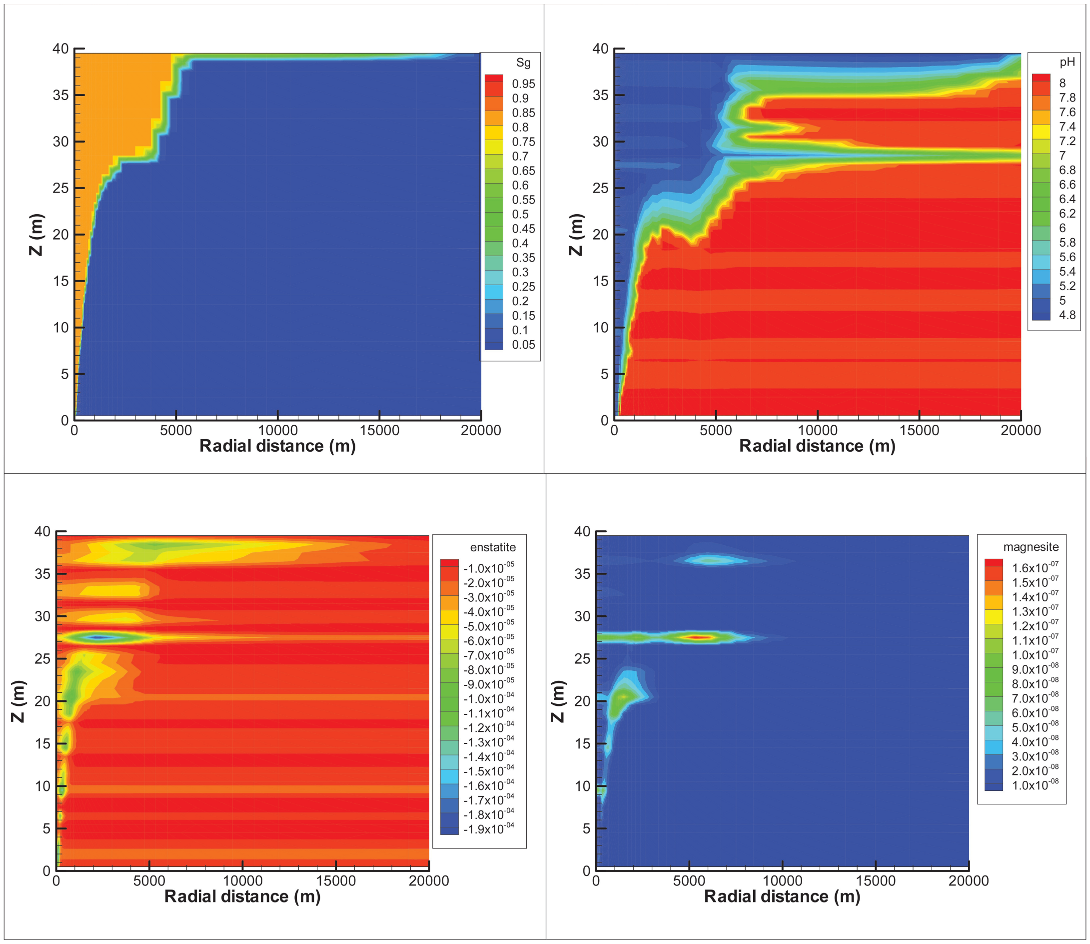

Figure 3.16 2D distribution of gas saturation, pH, enstatite (orthopyroxene) dissolution and magnesite precipitation at 10 years in the case of standard deviation=0.5

3.6.3 How common are volcanogenic sandstones like Etchegoin blue sandstone? Where do they occur?

Volcanogenic sandstones are sedimentary rocks with a volcanic provenance. Such sandstones occur in the vicinity of volcanic provinces, as a result of weathering, transport, and sedimentation. Today, there are at least 26 well defined active volcanic arcs in the world, mostly around the Pacific margin, plus many more inactive ones onshore in Tertiary deposits marginal to the Pacific basin. Each of these areas is rich in volcaniclastic deposits.

Sedimentary basins where volcaniclastics are deposited are usually either forearc or backarc basins. A forearc is a depression in the sea floor located between a subduction zone and an associated volcanic arc. The Cretaceous Great Valley Sequence, and the early Paleogene marine section overlying it in the Central Valley of California are examples of a thick section of sedimentary rocks deposited in a forearc basin. Active back-arc basins are mostly found in the Western Pacific. There are also a number of extinct back-arc basins, such as the Parece Vela-Shikoku Basin, Sea of Japan, and Kurile Basin.

Appendix 1 lists some volcanogenic sandstones from the literature all around the world whose properties have been described. Typical reservoir properties are reported including mineralogy, porosity and permeability when available. Appendix 1 also provides the locations of these volcanogenic sandstones. Most of the cited studies are for the purpose of understanding geology, especially diagenesis of volcanic sandstones, and some of them are related to petroleum assessment. As a consequence, not all aspects are covered for the interest of CO_2 sequestration, such as sealing layers, CO_2-water-rock interaction kinetic parameters, etc. Several reports from the West Coast Regional Carbon Sequestration Partnership (WESTCARB) (Cameron et al., 2005) compiled potential formations and basins in west coastal states of the US for CO_2 sequestration assessment. Several formations in the list have volcanogenic sandstones in them. Brief descriptions of these formations from (Cameron et al., 2005) are listed in Appendix 2. If these formations were to be used for CO_2 sequestration, there would be the benefit of high percent CO_2 mineralization for long term CO_2 storage.

In general, sediments with high VRF fractions tend to be heavily modified during burial diagenesis, including more compaction and secondary mineral precipitation in pore space, and hence have decreased porosity and permeability (Remy, 1994). However, diagenetic processes can lead to volcanogenic sandstone formations that are deeply buried but still relatively porous and permeable. For example, Berger et al (2009) found that in the sandstones of the Sawan gas field, Pakistan, well-developed chlorite rims inhibited quartz cementation, preserved porosities of up to 20%, and good permeabilities. De Ros et al (1994) showed that early cementation by hematite, smectite, quartz and calcite, and the relatively limited burial in the Guaritas Sequence, southern Brazil, prevented strong compaction and preserved some primary macro-porosity in most of the sandstones, whereas the absence of early cements and/or abundance of ductile grains promoted substantial porosity destruction by compaction and the inhibition of further diagenetic modifications.

Reed et al (1993a) presented core description and petrographic analyses of the East Slovakian Basin sandstone reservoirs. The sandstones are texturally and mineralogically immature lithic and feldspathic arenites. The presence of unstable lithic grains and feldspars contributes to low, irregular reservoir porosity, due to deformation by compaction, and susceptibility to chemical alteration. Reservoir quality is also influenced by the subsequent diagenesis of the sandstones, which is driven by high heat flow. Lithic fragments and feldspars alter readily to form authigenic diagenetic mineral suites, which tend to occlude porosity. However, dissolution of some of these grains also enhances secondary porosity development. Most observed porosity in the basin sandstones is secondary, developing from dissolution of both carbonate cement and unstable framework grains.

Overall, diagenetic processes in volcaniclastic rocks can affect the reservoir quality favorably or unfavorably. The presence of mineralogically unstable particles that are readily subjected to dissolution and in-situ precipitation of cement results in early reservoir quality destruction. However, under favorable circumstances (e.g. devitrification at shallow depth before severe compaction, fracturing or secondary porosity created by leaching at depth where the sediment framework is sufficiently consolidated to sustain the overburden stress), volcaniclastic rocks can form attractive reservoirs for CO_2 sequestration with high porosity and permeability.

In the current study, we also collected samples from the Cretaceous Panoche formation (GVZ1, GVZ2, CSZ1). These samples are generally light gray to light brown, bedded, hard, and fine to medium grained. Some samples contain large hard dark brown concretions, and include interbedded clay shales. Petrographic studies show that they are of arkosic compositions, but most of the reactive minerals (mainly pyroxenes) are gone. This is because volcanic rock fragments are altered most easily due to chemical instability, particularly as burial depth and temperature increase. The primary volcanic minerals are replaced preferentially by authigenic minerals such as chlorite and clays. These Cretaceous volcanogenic sandstones would not have the advantage of fast CO_2 mineralization if CO_2 is injected, since most of the fast dissolving minerals like pyroxenes have reacted away during diagenesis. However, the secondary minerals such as chlorite and clays are also sources of cations for CO_2 mineralization, and might dissolve almost as fast as pyroxenes given their high reactive surface areas (Landrot et al., 2012).

One pilot-scale CO_2 injection project that involves volcanogenic sandstone is located at the Minami Nagaoka gas field in Japan, where the target formation is a porous volcanic sandstone bed of the Pleistocene Haizume Formation at a depth of 1100 m. Permeability of this formation range from less than one millidarcy to several tens of millidarcy (Kampman et al., 2009). The formation sandstone is rich in volcanic minerals, mainly pyroxene, chlorite, biotite and amphibole. Formation water was collected prior to CO_2 injection and after cessation of CO_2 injection. Results show that the concentrations of HCO_3^-, Ca, Mg, Fe, Mn and Si increased from those of pre-CO_2 injection, suggesting that geochemical reactions in the reservoir occur at an early stage of CO_2 storage. The modeling study by Mito et al (2013) predicts that 50% of injected CO_2 would be mineralized in a time scale of 1000 years. This example shows the great potential of volcanogenic sandstones as CO_2 sequestration targets in mineralizing and immobilizing CO_2 if used for CO_2 sequestration.

Appendix 1: Volcanogenic sandstones around the world and related properties

Volcanogenic sandstones	Reference:	Mineralogy	Porosity	Permeability
Cretaceous sandstones of the Sawan gas field, Pakistan	(Berger et al., 2009)	1-23%VRF	8.8-26.94%	0.03-1252.07 mD
Cambro-Ordovician Guaritas Sequence, Southern Brazil	(De Ros et al., 1994)	5.5%VRF Average	5.9%	N/A
Upper Triassic Stuttgart Formation in the Northeast German Basin	(Forster et al., 2010)	2.3-10.3%VRF	13-26%	500-1000 mD
Neogene east Slovakian BAsin	(Reed et al., 1993b)	7-23%rock	8-30%	9 to

		fragments		several hundred mD
Middle Park Basin, Colorado	(Remy, 1994)	70-100%VRF	2.1-15.7%	N/A
Cretaceous Windsor,Hanover and Sunderland Formations, Eocene Richmond and Chapelton Formations, Jamaica	(Rodrigues, 1991)	37-83%VRF	13%	6mD
Murihiku Terrane, New Zealand	(Roser et al., 2002)	45-74%VRF	N/A	N/A
Eocene Tyee Basin, southern Oregon Coast Range	(Ryu, 2003)	6.93-36.62%VRF	10.80%	2.76 mD
Lower Cretaceous Kanmon Group sandstones, SW Japan	(Sur et al., 2002)	12.7-31.3%, 8.0-35.7%rock fragments, ~50%volcanic	N/A	N/A
Blue Nile Basin, Ethiopia	(Wolela, 2010)	0.2-10%rock fragments	0.4-20.4%	10-710mD
southern Junggar basin, northwestern China	(Tang et al., 1997)	50-82%VRF	12.9-23.7%	1.2-204.3mD
Warrawoona Group, Pilbara Block, Western-Australia	(Dimarco and Lowe, 1989)	58-86%VRF	N/A	N/A
Thakkhola region (Chukh and Tangbe Formations), central Nepal	(Durr and Gibling, 1994)	1.8-42.8%mafic VRF	N/A	N/A
Southern Alps, Italy	(Garzanti, 1985)	60-65%VRF	N/A	N/A
Surat Basin, Australia	(Hawlader, 1990)	9.3-51.0%rock fragments, ~90%volcanic	22-27%	34-647mD
East Java, Indonesia	(Smyth et al., 2008)	2-35.4%rock fragments	N/A	N/A
the Murihiku and Waipapa Terranes, North-Island, New-Zealand	(Black et al., 1993)	N/A	N/A	N/A
Cretaceous and Miocene sequences of the NW African margin	(De Ros et al., 1997)	N/A	N/A	N/A

Appendix Figure 1: Locations of volcanogenic sandstones reported in the literature

Appendix 2: Potential volcanogenic sandstones for CO_2 sequestration in western US

Formation	Basin	Description
Purisima	La Honda	The Purisima Formation is widespread throughout the basin, resting on granitic basement rocks to rocks as young as the Santa Cruz mudstone. The Purisima includes arkosic and *volcanic sandstones*, conglomerate and mudstone. Sandstones are generally lenticular stringers but may reach as much as 30 m (100 feet) thick. Shallow Purisima sandstones between 245–825 m (800 and 2,700 feet) deep exhibit porosities of 22–34 percent and permeabilities of 1–40 md (DOGGR, 1991).
	Surprise	Surprise Basin is a large complexly faulted graben straddling the Nevada state line in northeast California's Modoc County. The basin is approximately 80 km (50 mi.) long by 20 km (12 mi.) wide, the California portion comprising about 857 km2 (331 sq. mi.). The valley is bounded on all sides by normal faults including the Surprise Valley Fault on the west and the Hays Canyon Fault on the east. Smaller faults mark its northern and southern ends. Surface deposits are coalesced alluvial fan and near-shore lake deposits. While the depth to bedrock is unknown, several geothermal exploratory wells penetrated 2,139-m (7,015-foot) thick sequence of interbedded volcanic breccias, tuffs, *volcanic sandstones* and conglomerates, clays, rhyolite, andesite, and basalt. Sample logs and lost circulation problems while drilling suggest that the igneous rocks may be highly fractured, but lacustrine clay beds and altered argillaceous tuffs might provide seals for underlying sandstones where structural closure or stratigraphic containment could

		be demonstrated.
	Big Valley	Big Valley Basin is a broad flat plain comprising about 319 km^2 (123 sq. mi.) in southwest Modoc and northwestern Lassen Counties. The basin consists of a series of downthrown grabens surrounded by tilted fault block ridges. To the north, south, and east are Pleistocene and Pliocene basalt and Tertiary pyroclastic rocks of the Turner Creek Formation, and to the west are Tertiary rocks of the Big Valley Mountain volcanic series. Basin depth is unknown, but a single geothermal exploratory well drilled near the basin center provides some insight into the basin's stratigraphy. The well encountered 2,134 m (7,000 feet) of interbedded medium to coarse arkosic and *volcanic sandstone* and conglomerate interbedded with tuffaceous claystone, green-gray claystone, tuff, and siltstone. The lateral extent of these facies is unknown, but the vertical facies relationships suggest that at least aquifers and seals may be present.
Northcraft	The Willapa Hills	The Willapa Hills Basin comprises topographic hills that rise to about 950 m (3,100 ft) above sea level and are situated between the Olympic Mountains to the north and the Columbia River to the south. The Willapa Hills (Grays Harbor) Basin contains up to 4,600 m (15,000 ft) of upper Oligocene to Quaternary strata overlying basement/broken mélange of mid-Miocene to early Oligocene age. Eocene and Oligocene sediments consist predominantly of deep-water siliciclastics, and arkosic sandstones; interbedded *volcaniclastic sandstones* are contained within thick marine shale sequences.
Blakeley and Blakeley Harbor	Everett-Seattle-Tacoma	Oligocene - Eocene (OEm(b)), marine sedimentary rocks in the northern Puget Sound area of interbedded *volcaniclastic sandstone*, siltstone, shale, and conglomerate.
Tukmila	Everett-Seattle-Tacoma	*volcaniclastic rocks*/deposits (sandstone, siltstone, and conglomerate).
Sub-Columbia River Basalt Sedimentary Basin	Wildcat Creek	Oligocene (Ovc(wc)); more than 300 m (1,000 ft) of tuffs and *volcaniclastic sandstones.*
Sub-Columbia River Basalt Sedimentary Basin	Ohanapecosh	Eocene (Ohm(oh)); tuffs and *volcaniclastics*.
Methow	Newby Group	Jurassic-Cretaceous (KJm(n)). *Volcanic lithic sandstone*, conglomerate, siltstone, black shale, argillite, carbonate pods, and andesitic-dacitic volcanic rocks. Total thickness estimated as at least 1,830 m (6,000 ft).
	Kittatas-Yakima-Selah	These three unconsolidated basins extend eastward from the foothills of the Cascade Ranges Mountains onto the western edge of the Columbia Plateau Basin. The eastern portion of the basin (east of Cle Elum) transitions into the Yakima fold belt, consisting of structural basins filled with sedimentary and *volcaniclastic sediments*, and upland areas of volcanic rocks such as basalt.

	Klamath Lake	The Klamath Lake Basin is located on the eastern flank of the Klamath Mountains. The basin contains unconsolidated fluvio-lacustrine deposits of diatomite, water-lain *volcanic sediments*, and tephra with localized alluvium, alluvial fans, and tallus. Sediments are generally thin (~10 m (tens of feet)) but can be up to ~100 m (hundreds of feet) near fault escarpments. The sediments are generally above the water table, though minor amounts of perched water do occur. The basin also includes a continental sedimentary unit, often referred to as the Yonna Formation. The unit consists of bedded sandstone, siltstone, laminated mudstone, and conglomerate and tuff, underlain and overlain by Miocene lava flows. The geologic sections in Sherrod and Pickthorn (1992) illustrate the formation to have a thickness of up to 760 m (2,500 ft).

Chapter 4 Chemical affinity and pH effects on chlorite dissolution kinetics under geological CO_2 sequestration related conditions

4.1 Introduction

Minerals that are sources of divalent cations and common in impure sandstones are biotite, chlorite, glauconite, amphibole, epidote, and montmorillonite. Chlorite (sheet-structured aluminosilicates containing variable amounts of magnesium and iron) is found to be the most abundant and reactive mineral that contains the cations in one of the CO_2 sequestration pilot sites in Cranfield, Mississippi (Landrot et al., 2012). Chlorite minerals are also common constituents of numerous formations and typically occur as grain-coating or pore-filling growths in sedimentary sandstones, alteration products of mafic minerals in basaltic units, or as products of low-grade metamorphism of many prior assemblages. Although chlorite dissolution rates are not as high as those of mafic minerals such as pyroxene and olivine, the extent of water-chlorite reaction is expected to be significant because (1) the brine in contact with rocks will be acidified with dissolved CO_2, (2) the time scale for safe storage of CO_2 in a sequestration site may be of order thousands of years, and (3) the reactive surface area of chlorite-rich sandstones is relatively large (11.62×10^{-2} m^2/g for the Cranfield sandstone (Landrot et al., 2012)).

Geochemical reactive transport simulations are currently used to model the reaction and evolution of CO_2 containing fluids with bedrock minerals during CO_2 sequestration. In order to make accurate predictions of the evolution of such subsurface systems with modeling, it is critical to know the mineral/fluid reaction kinetics for the relevant phases. Most treatments of mineral dissolution and precipitation reaction kinetics in the reactive transport simulators, however, have relied on rate laws based on linear transition state theory formulations (Aagaard and Helgeson, 1982; Lasaga, 1984). For the purposes of modeling CO_2 injection and sequestration and its effects on geochemistry and mineral evolution, it is critical to provide experimentally verified kinetic rate equations over the full range of relevant conditions. Some studies of chlorite mineral dissolution kinetics have been published (Brandt et al., 2003; Lowson et al., 2007; Malmström et al., 1996; Rochelle et al., 1994; Smith et al., 2013), although none of these have explored the dependence of chlorite dissolution kinetics on the departure from equilibrium (or chemical affinity), despite the demonstrated importance of this effect in natural systems (Maher et al., 2009; Steefel et al., 2005). The dependence of the rate on the chemical affinity becomes particularly important if the transition to the maximum far from equilibrium rate (the so-called "dissolution plateau) is broad, i.e., it does not show a linear dependence on the departure from equilibrium (Maher et al., 2009).

In this chapter, laboratory experiments were conducted to understand the dissolution rate dependence of chlorite with respect to the chemical affinity or Gibbs free energy of the reaction. We used well-stirred flow-through reaction vessels in which steady-state rates were determined at specific solution saturation states, and at elevated temperature and pressure relevant for CO_2 sequestration. Our two major objectives are: 1) to examine the effect of chemical affinity on chlorite dissolution rate within the framework of transition state theory, and 2) to obtain a complete kinetic dissolution rate equation on mineral chlorite that is applicable for subsurface CO_2 sequestration modeling. The content based on this chapter is submited to the journal of Chemical Geology, titled *Chemical affinity and pH effects on chlorite dissolution kinetics under geological CO_2 sequestration related conditions*.

4.1.1 Previous studies

Most previous studies of chlorite dissolution have been conducted at room temperature and pressure, although at various pH values (Banfield and Murakami, 1998; Brandt et al., 2003; Hayashi and Yamada, 1990; Lowson et al., 2007; Lowson et al., 2005; Malmström et al., 1996; Rochelle et al., 1994). Lowson et al. (2005) summarized results reported in the literature and concluded that the dissolution of chlorite is enhanced in acidic solutions and alkaline solutions and is independent of pH in the neutral pH region. In CO_2 saturated water with a pH of 3-4, these studies suggest the dissolution rate of chlorite would be 10^{-12}-10^{-11} mol/m^2/s at 25 ºC assuming that the effect of CO_2 on dissolution kinetics is only via its effect on pH.

Smith et al. (2013) measured chlorite ($(Mg_{4.29}Al_{1.48}Fe_{0.10})(Al_{1.22}Si_{2.78})O_{10}(OH)_8$) dissolution kinetics under far from equilibrium conditions using a mixed-flow reactor over temperatures of 100-275 °C at pH values of 3.0-5.7 in a background solution matrix of 0.05 m NaCl. Over the investigated range of far-from-equilibrium experimental conditions, the surface area normalized rate of Mg-rich chlorite dissolution was described as (Smith et al., 2013):

$$rate = k_{acid}\exp[(\frac{-E_{acid}}{R})(\frac{1}{T}-\frac{1}{298K})]a_{H^+}^{n} \tag{4.1}$$

where the apparent acid rate constant at 25 °C is $k_{\text{acid}} = 10^{-9.91}$ mol/m^2/s, the reaction order n with respect to H^+(aq) is 0.49, and the activation energy for the acid mechanism is $E_{\text{acid}} = 25.1$ kJ/mol.

Lowson et al (2007) measured dissolution rates of an iron rich chlorite $(Mg_{2.76}Fe(II)_{1.90}Fe(III)_{0.07}Al_{0.97})[Si_{2.48}Al_{1.52}O_{10}](OH)_8$ as a function of pH over the range from 3.0 to 10.5 and at temperatures between 25 and 95°C. They fitted their dissolution rates as a function of pH at room temperature as

$$R = 10^{-9.79}a_{H^+}^{0.49} + 10^{-13.00} + 10^{-16.79}/a_{H^+}^{0.43} \tag{4.2}$$

To date, no experiments have been reported that determine the chlorite dissolution rate under near equilibrium conditions. However in natural systems, close-to-equilibrium conditions are prevalent, so it is critical to investigate the effect of chemical affinity in order to have a dissolution rate law that is applicable over the full range of conditions. In this chapter, we conducted experiments under both far-from-equilibrium and near-equilibrium conditions, and observed significantly different behavior of chlorite dissolution under these two conditions. Measured dissolution rates are expressed in terms of both a pH and a chemical affinity term, thus providing a complete kinetic expression of chlorite dissolution kinetics at 100 °C.

4.1.2 Effect of environmental variables on mineral dissolution kinetics

A general rate law for dissolution and precipitation can be written as (Lasaga, 1995):

$$rate = k_0 \exp(\frac{-E_{app}}{RT}) a_{H^+}^{n_{H^+}} \Pi a_i^{n_i} g(I) f(\Delta G_r) \qquad (4.3)$$

where k_0 is a constant, E_{app} is the apparent activation energy of the overall reaction, R is the gas constant, T is the absolute temperature, a_i and a_{H+} are the activities in solution of species i and H^+ respectively, n_i and n_{H+} are the orders of the reaction with respect to these species, $g(I)$ is a function of the ionic strength(I) and $f(\Delta Gr)$ is a function of the Gibbs free energy to account for the chemical affinity effect. This formulation is semi-empirical, and its primary usefulness is to remind the user that mineral-fluid reaction rates are complicated, and are typically affected by several environmental variables. A quantitative understanding of the effects of all the above variables is needed to accurately model the geochemical reactions resulting from CO_2 sequestration via a coupled reaction-transport model.

The dependence of $f(\Delta Gr)$ is ofter presented in a generalized form derived from transition state theory(TST) (Lasaga, 1998):

$$f(\Delta G_r) = 1 - \exp(\frac{\Delta G_r}{RT}) \qquad (4.4)$$

where R is the gas constant and T is the absolute temperature. This expression is based on the assumption of detailed balance (or reversibility) and for mineral-fluid reactions is difficult to predict *a priori* (or to justify). The equation may be generalized to (Aagaard and Helgeson, 1982):

$$f(\Delta G_r) = 1 - \exp(\frac{\Delta G_r}{\sigma RT}) \qquad (4.5)$$

where σ is a coefficient that is not necessarily equal to 1. Usually this is considered as the Temkin coefficient that relates the stoichiometry of the rate-limiting step to the stoichiometry of the mineral-water reaction. For small deviations from equilibrium, i.e., $/\Delta Gr/ << \sigma RT$, a Taylor series expansion of the exponential term leads to a linear relation between rate and ΔGr

$$f(\Delta G_r) = \frac{\Delta G_r}{\sigma RT} \qquad (4.6)$$

However, experiments have shown that dissolution is not a linear function of the Gibbs free energy in many cases.(Burch et al., 1993; Cama et al., 2000; Carroll et al., 1998; Hellmann and Tisserand, 2006;

Nagy et al., 1999; Nagy and Lasaga, 1992). Nagy and Lasaga (1992) propsed to use the following equation to describe gibbsite dissolution rate as a function of ΔGr:

$$f(\Delta G_r) = 1 - \exp[m(\frac{\Delta G_r}{\sigma RT})^n] \tag{4.7}$$

where m and n are experimentally determined coefficients.

In this study, a series of experiments was conducted at different CO_2 partial pressures (0-60 bars) and different flow rates (0.01-0.25ml/min) to control the departures of the experimental system from equilibrium and study the effects of Gibbs free energy on mineral chlorite dissolution kinetics. We show that the chemical affinity effect on the kinetics of chlorite dissolution cannot be described by a simple linear TST rate law, but can be fitted with an empirical TST based equation such as Equation 4.7 from Nagy and Lasaga (1992).

4.2 Experimental methods

4.2.1 Sample

Chlorite schist from Flagstaff Hill, California, the standard Mg-rich chlorite source mineral (CCa-2) from the Clay Minerals Society, was used in this experimental study. The average chlorite composition based on electron microprobe analysis was $(Mg_{4.55}Al_{1.23}Fe_{0.12})(Al_{1.04}Si_{2.96})O_{10}(OH)_8$, derived by distributing aluminum first in the tetrahedral site and the remainder in octahedral sites, and assuming all iron as ferrous, following the recommendations and observations of Foster (1962).

The chlorite sample was mechanically broken into pieces of cm-range and then grounded and sieved to a particle size of 90 to 105 micron. Samples were then rinsed clean of small particle debris prior to dissolution experiments by washing with ultra-pure H_2O and vacuum filtration through 0.1 micron polycarbonate membrane filter. The cleaned samples were dried at 50 ^oC in an oven, gently crushed and stored in a HDPE bottle for experimental use. The BET surface area determined for the chlorite samples prepared in this way was 8.44 m^2/g, as measured on a Quantachrome Autosorb-1 surface area analyzer with N_2 as absorption gas.

4.2.2 Flow through experiments

Figure 4.1 is a schematic illustration of the experimental system that was used to investigate chlorite dissolution kinetics when reacting with CO_2 saturated fluids under high-temperature and high-pressure conditions. A mixed flow-through reactor (Series 4560 Mini Reactor 300 mL) manufactured by Parr Instruments Company was used in the study. All parts of the reactors that were in contact with the high temperature aqueous solution are made of Hastelloy or 316 Stainless Steel. Flow rates were controlled by a HPLC pump (labeled 'brine pump' in Figure 4.1) and were varied from 0.25 ml/min to 0.01 ml/min, yielding a residence time within the stirred flow-through reactor of 20 h to 20 days. A few hundred hours are usually maintained for each experiment, corresponding to 6 to 1 residence volumes.

Stirring of chlorite and the reacting fluids was through a mechanically driven stirrer placed inside the Parr reactor. CO_2 in the experiment study was injected through a supercritical CO_2 pump at a flow rate of 0.01 to 0.1 ml/min so as to obtain the desired pCO_2 conditions. Total DIC was measured for random samples to verify that desired pCO_2 is achieved. The experimental system pressure was kept constant with a Jasco BP-2080 adjustable automatic back pressure regulator at given pressures. The temperature was controlled in the experiments using an automatic temperature controller supplied with the Parr reactor.

During each of the experiments, one gram of the sieved chlorite sample was transferred into the reactor. CO_2 and saline water (0.01 M NaCl) were first pumped into a mixing tee where they were mixed and brought to the experimental temperature of 100 ^{o}C. The mixing tee has a volume of ~10 ml, while CO_2 and saline water are pumped through it at a rate of 0.01 ml/min to 0.25 ml/min, yielding a residence time of 1000 minutes to 40 minutes. For experiments with low partial pressure of CO_2 (0~0.1 bar), high purity CO_2 gas was purged directly into the reaction stock solutions through a two stage regulator and allowed to equilibrate overnight before injections into the experiment reactor. The brine saturated with CO_2 was then pumped into the reactor while maintaining the experimental system at the designated pressures. The solution inside the reactor chamber was constantly stirred during the experiment.

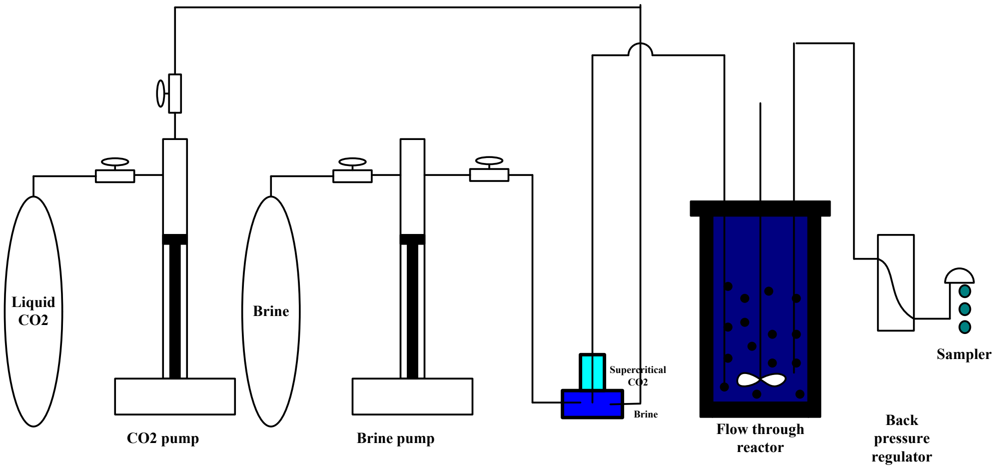

Figure 4.1 Schematic drawing of the flow-through batch experiment setup. The CO_2 and saline water are first pumped into a tee where they are mixed and brought to experimental temperature. The CO_2 saturated brine is then pumped into the reactor and mixed with chlorite particles, while continuously stirring the reactor volume. Samples are collected after the back pressure regulator and their elemental concentrations are measured using ICP-MS

4.2.3 Solutions and analyses

Solutions were filtered through a 10 micron Hastelloy filter on the effluent port of the Parr reactor and passed through the automatic back pressure regulator before dripping into the sample collection vials. Filtered effluents were collected in clean low-density polyethylene bottles or polypropylene vials. The solutions collected were analyzed for Mg, Fe, Al and Si by a Perkin Elmer DRCII inductively coupled plasma mass spectroscopy (ICP-MS) after acidification with 2% ultra-pure HNO_3. The solution pH was measured with an Acute pH electrode with a reported accuracy of 0.02 pH units. The solution pH was then corrected to experimental conditions at high temperature and high pressure using the modeling code PHREEQC.

4.3 Dissolution reaction and equilibrium constant

The chemical reaction describing dissolution of the Clay Minerals Society chlorite used in this study under acidic conditions can be expressed as:

$$(Mg_{4.55}Al_{1.23}Fe_{0.12})(Al_{1.04}Si_{2.96})O_{10}(OH)_8 + 16.15H^+$$
$$<=> 2.27\,Al^{3+} + 0.12\,Fe^{2+} + 4.55\,Mg^{2+} + 2.96\,SiO_2 + 12.075\,H_2O \quad (4.8)$$

The equilibrium constant for this reaction is given by:

$$K_{eq} = \frac{(a_{Al^{3+}})^{2.27}(a_{Fe^{2+}})^{0.12}(a_{Mg^{2+}})^{4.5}(a_{SiO_2})^{2.96}(a_{H_2O})^{12.075}}{(a_{H^+})^{16.15}} \quad (4.9)$$

where a_i represents the thermodynamic activity of the dissolved species.

Based on mass balance, the surface area normalized mineral dissolution rate is calculated from the measured difference between the outflow and injection solution concentration of element *i*, ΔC_i (mol/g solution) according to the expression:

$$R_i^d = \frac{Q\Delta C_i}{mA\nu_i} \quad (4.10)$$

where R^d_i = reaction rate (mol/m^2/s); Q = flow rate (g/s); m = mass of mineral (g); A = specific surface area (m^2/g); and v_i is the stoichiometric factor (moles of element/moles of mineral). This is valid when steady state is reached, i.e., the concentration in the output solution reaches a constant value.

The solution saturation state with respect to chlorite is expressed in terms of the Gibbs free energy of reaction,

$$\Delta G_r = RT\ln[\frac{IAP}{K_{eq}}] = RT\ln[\Omega] \quad (4.11)$$

where R is the gas constant, T is the absolute temperature (K), IAP and K_{eq} are the ion activity product and the equilibrium constant respectively, and $\Omega = IAP/K_{eq}$. The geochemical computer code PHREEQC (Parkhurst, 1999) was used to calculate the activities of solution species and the corresponding ion activity product at experimental conditions.

4.4 Results

A series of experiments was run at different CO_2 partial pressures (0bar, 0.1bar, 20bar, and 60bar) and different flow rates (0.25ml/min, 0.05ml/min and 0.01 ml/min) to study the Gibbs free energy effect on the chlorite dissolution kinetics. All experimental conditions, measured concentrations of solution specie, corrected pH values, the Gibbs free energies and dissolution rates obtained are summarized in Table 1. Reaction rates are calculated from the steady state concentration profiles of Si.

Table 4.1 Corrected pH under experimental conditions, flow rates, measured steady state concentrations and calculated ΔGr values and chlorite dissolution rates

CO_2 pressure	pH	flow rate (ml/min)	Mg (10^{-5} mol/L)	Al (10^{-5} mol/L)	Si (10^{-5} mol/L)	Fe (10^{-5} mol/L)	ΔG (kJ/mol)	Rate(Si) (10^{-12} mol/m^2/s)
0bar	6.427	0.05	8.41	0.03	6.45	0.09	-90.72	3.70
0bar	6.402	0.01	10.10	0.32	8.89	1.31	-28.36	1.02
20bar	3.606	0.25	3.44	1.89	3.51	1.79	-155.44	10.10
60bar	3.321	0.25	4.89	0.17	3.04	0.01	-226.66	8.77
60bar	3.433	0.05	19.80	0.06	9.98	0.01	-197.37	5.77
60bar	3.756	0.01	78.20	0.06	29.50	0.01	-161.87	3.41
0bar	6.842	0.25	7.32	0.07	0.38	0.32	-78.15	1.25
0bar	7.257	0.05	8.45	0.34	0.98	0.70	-46.50	0.64
0bar	7.508	0.01	12.20	0.03	1.81	2.90	-15.07	0.24
0.1bar	4.885	0.25	1.09	0.06	1.11	0.28	-113.94	3.21
0.1bar+Mg	5.186	0.25	11300.00	0.14	0.56	0.26	-68.00	1.60

4.4.2 Equilibrium constant of chlorite dissolution reaction

In order to determine the effect of solution chemical affinity on chlorite dissolution kinetics, an accurate value of the equilibrium constant on the chlorite sample studied is required. For this purpose, we have run a batch experiment to determine an apparent equilibrium constant as a proxy for the required thermodynamic constant. The batch experiment reactor was stirred for two months at constant temperature to determine the equilibrium constant for the chlorite mineral used in the study. According to the corresponding fluid chemistry analyzed by ICP-MS, the ion activity product obtained from the batch experiments was calculated and used as the equilibrium constant for the chlorite dissolution reaction at 100°C. The K_{eq} obtained from our batch experiments was determined to be $10^{-45.57}$. In the PHREEQC LLNL database, the end-member of the chlorite mineral group that has the closest composition to our sample is Clinochlore-14A, which contains no Fe. Using the analytic equation for K_{eq} of Clinochlore-14A, the equilibrium constant at 100°C is $10^{-45.27}$, which is quite close to the measured K_{eq} from our experiments. Also, as pointed out by Burch et al. (1993), substituting apparent equilibrium constant K^*_{eq} for K_{eq} would only shift the values of the Gibbs free energy, but would not affect the functional dependence of rate on the degree of saturation. Thus the measured equilibrium constant should be a good reference number for calculating chemical affinities of all the kinetic dissolution experiments conducted.

4.4.3 Congruency of chlorite dissolution

Congruent dissolution of chlorite is indicated if the reaction rate calculated from Equation 4.10 is identical using the outflow concentrations of magnesium, aluminum, iron, or silica. Nonstoichiometric dissolution, if it occurs, may reflect chemical zonation within the mineral, e.g., the development of a leached layer or the presence of non-homogenous defects or impurities, such that the stoichiometry of the dissolving surface regions is different from the average composition of the mineral. Nonstoichiometric dissolution may also be the result of precipitation of secondary phases during the experiment. To ascertain that the dissolution rate obtained is reliable, it is important to show that the rate calculated from Equation 4.10 reflects the destruction of the whole crystallographic framework of the chlorite. Chlorite dissolution rates were calculated based on the release of silicon, aluminum, iron and magnesium at steady state, for each of the flow-through experiments. Figure 4.2 plots the dissolution rates evaluated based on the release of Al and Mg versus those obtained based on the release of Si. The solid line in Figure 4.2 is the 1/1 diagonal.

Taking into account of the uncertainties in the rates obtained, Figure 4.2 shows a good agreement between dissolution rates calculated from the effluent concentrations of Mg and Si. The calculated dissolution rates based on the concentrations of Al and Fe are substantially lower. This discrepancy indicates that either the release rates of Fe and Al are less than the stoichiometric or that the Fe and Al are reprecipitated in another phase. Taking into account the low solubility of Fe and Al phases in solution, the latter explanation seems to be most probable. To evaluate this, the saturation index for relevant phases that might precipitate during the mixed-flow reactor experiments was calculated for each experimental condition using the speciation program PHREEQC(Parkhurst, 1999). Calculated saturation index values for possible secondary phases in Table 4.2 indicate that the experiment was supersaturated or close to saturated with respect to several hydrous Al phases. Based on the calculations, it appears likely that the low Al concentrations may be controlled by equilibrium with gibbsite. Since the release of Mg and Si appeared to be stoichiometric, we assume that the release of Fe and Al was stoichiometric as well. In addition, brown-colored Fe-bearing secondary mineral phases were observed in the vessel after the experiment. However, based on SEM images of chlorite particles before and after reaction, there was no detectable secondary mineral precipitation on the surface of the sample and there was no distinguishable alteration of the chlorite mineral surface. Mass balance calculation indicates that only about 1% of the chlorite sample was dissolved during the experiment. Since Al and Fe was minor constituents of the chlorite mineral, the volume fraction of secondary minerals precipitated from the Al and Fe released in solution during the experiment would be much less than 1% of the volume of the original chlorite. Such a small amount of precipitate is difficult to detect with Scanning Electron Microscopy. So the precipitated secondary phases should not block the primary mineral surface or affect the chlorite dissolution kinetics during the experiment.

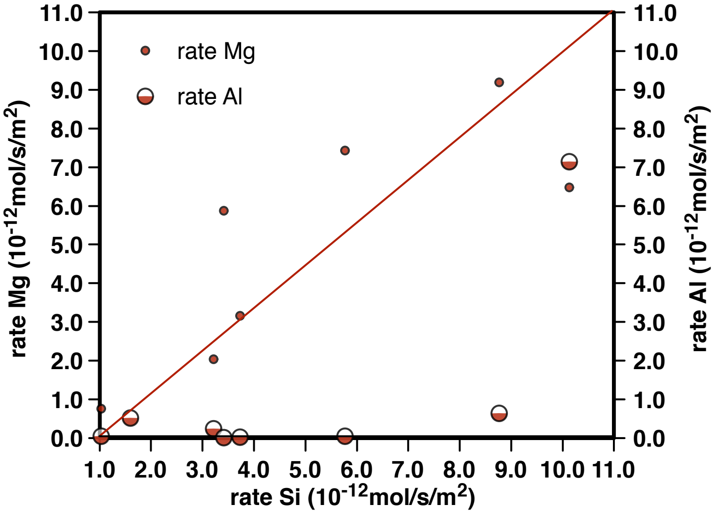

Figure 4.2 Comparison of the chlorite dissolution rates calculated from the release of Si, Mg, and Al compared to the 1/1 diagonal. The dissolution rates calculated from the effluent concentrations of Mg and Si show good agreement, while the calculated dissolution rates using Al are substantially lower. The most likely explanation is that low Al concentrations reflect reprecipitation of secondary hydrous Al phases, such as gibbsite.

Table 4.2 Saturation index for possible secondary minerals for each experiment

SI	0bar 0.25ml/min	0bar 0.05ml/min	0bar 0.01ml/min	20bar 0.25ml/min	60bar 0.25ml/min	60bar 0.05ml/min	60bar 0.01ml/min	chemical formula
Diaspore	0.23	-0.13	0.31	0.76	1.02	-0.06	0.57	$AlHO_2$
Boehmite	-0.06	-0.43	0.01	0.47	0.73	-0.36	0.28	AlO_2H
Gibbsite	-0.53	-0.90	-0.46	0	0.25	-0.83	-0.19	$Al(OH)_3$
Kaolinite	-4.89	-4.84	-3.44	-2.07	-1.4	-2.66	-0.45	$Al_2Si_2O_5(OH)_4$

4.4.4 Differing effluent concentrations under far from and near equilibrium conditions.

According to linear transition state theory, the chemical affinity term $f(\Delta Gr)$ is 1 minus an exponential term that has a value between 0 to 1 (Equation 4.4). When $/\Delta Gr/$ is large (which indicates far-from-equilibrium conditions), the exponential term is close to zero, and the chemical affinity $f(\Delta Gr)$ is approximately equal to 1. In the linear TST formulation, the chemical affinity term begins to decrease toward zero (chemical equilibrium) when $/\Delta Gr/$ decreases to a value of about 4RT, which under our experimental conditions is about 12.4 kJ/mol. The value of $f(\Delta Gr)$ approaches zero only when ΔGr is less than about 0.1RT, which corresponds to about 0.31 kJ/mol. Consequently, the chemical affinity term takes effect only when Ω is barely distinguishable from unity.

To investigate the effects of chemical affinity on chlorite dissolution rates, our approach was to increase the dissolved species concentrations (and hence *IAP*) systematically in a continuous set of experiments while keeping pH and other variables constant. The increase in concentrations of dissolved species were achieved either by decreasing flow rate or by adding additional Mg to the injection solution. Under far-from-equilibrium conditions where the dissolution rate is insensitive to ΔG_r, a decrease in flow rate, thus increasing the residence time in the reactor, should result in a proportional increase in Mg and Si concentrations according to Equation 4.10. Figure 4.3 and Figure 4.4 show the behavior of solution chemistry and calculated dissolution rates in the first experiment set carried out at low pH and without any cations added to the injection solution. The effluent Mg and Si concentrations initially reached steady state in about 100 hours at a high flow rate of 0.25 ml/min. The concentrations increased when the flow rate was decreased to 0.05 ml/min, finally reaching a new steady state values about 5 times higher than in the fast flow rate (short residence time) case. The saturation index of chlorite was thus higher in the slow flow rate condition than in the high flow rate condition, but the measured dissolution rate remained unchanged. The transition from 0.05ml/min to 0.01 ml/min showed similar behavior. This was consistent with transition state theory where mineral dissolution rate is constant at far from equilibrium conditions, and therefore not sensitive to the thermodynamic driving force (chemical affinity) of the system. The ΔG_r value was -227 kJ/mol at 0.25 ml/min flow rate, -197 kJ/mol at 0.05 ml/min, and -162 kJ/mol at 0.01 ml/min. The wide range of ΔG and near-constant dissolution rate indicated that all of these experiments were conducted under far-from-equilibrium conditions.

Figure 4.5 shows the measured effluent concentrations of elements in pH ~7 water with no added CO_2. Satisfactory steady state dissolution conditions were reached under both 0.05 ml/min and 0.01 ml/min flow rates. In comparison with the experiments described above carried out at low pH, the effluent elemental concentrations increased only by about 1.25 times, corresponding to a dissolution rate decrease of a factor of 4, rather than the 5 times predicted by the change in flow rate and far-from-equilibrium conditions. This result indicates that the solution was in the "near equilibrium" regime where a change in ΔGr has caused a change in dissolution rate. The calculated ΔGr is -46.5 kJ/mol at 0.05 ml/min and -15.1 kJ/mol at 0.01 ml/min. These values were much lower than those at the low-pH conditions, but still large relative to RT (≈ 3.1 kJ/mol).

Figure 4.6 showed the results from another set of experiments where the solution chemical affinity was changed by adding additional Mg^{2+} in brine saturated with CO_2 at 0.1 bar pressure. After completion of the experiment with 0.01M NaCl brine solution only, the injection solution was switched to a new composition consisting of 0.1M $MgCl_2$ and 0.01M NaCl to drive the solution closer to equilibrium with mineral chlorite. If the experiment were still at far from equilibrium conditions after addition of Mg, change of chemical affinity would not affect the dissolution rate of chlorite. However, we observed a decrease in the effluent Si concentration, indicating a decrease of the dissolution rate of chlorite under near-equilibrium-conditions. Calculated ΔGr values were -113.94kJ/mol and -68.00kJ/mol before and after switching to injecting stock solutions with added Mg^{2+}.

In summary, we controlled the chemical affinity of the experiment system by changing flow rates in both acidic and neutral brines, and by adding dissolved Mg^{2+} to near-neutral brine. With those approaches, we were able to measure the chlorite dissolution rate at ΔG_r values varying from -227 to -15 kJ/mol. We observed that the chlorite dissolution rate was insensitive to changes of ΔG_r when the value was larger than -100 kJ/mol, but showed variation with ΔG_r when the value was lower than -100 kJ/mol. This observation suggests that chlorite dissolution exhibits "near equilibrium" behavior when ΔG_r is between -100 and 0 kJ/mol.

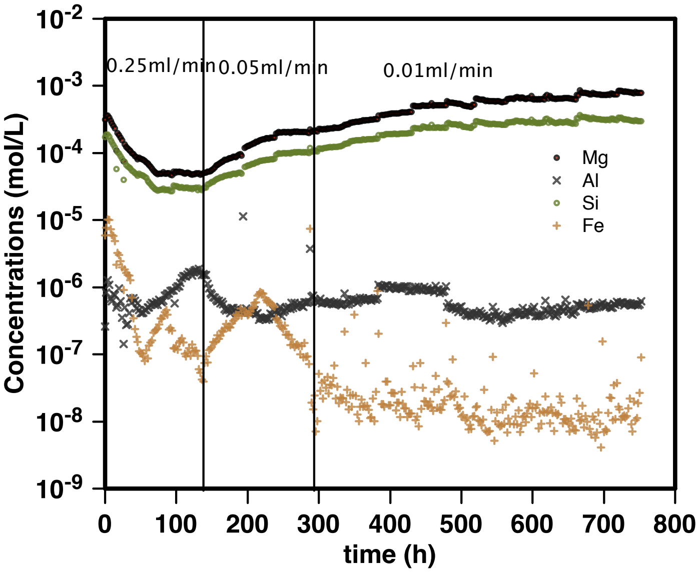

Figure 4.3 Concentrations of effluent elements for chlorite dissolution in 60 bar CO_2-saturated water at 100 °C. Steady states are achieved under three flow rates, 0.25ml/min, 0.05ml/min, and 0.01ml/min. Steady state concentrations of Mg and Si are inversely proportional to flow rates

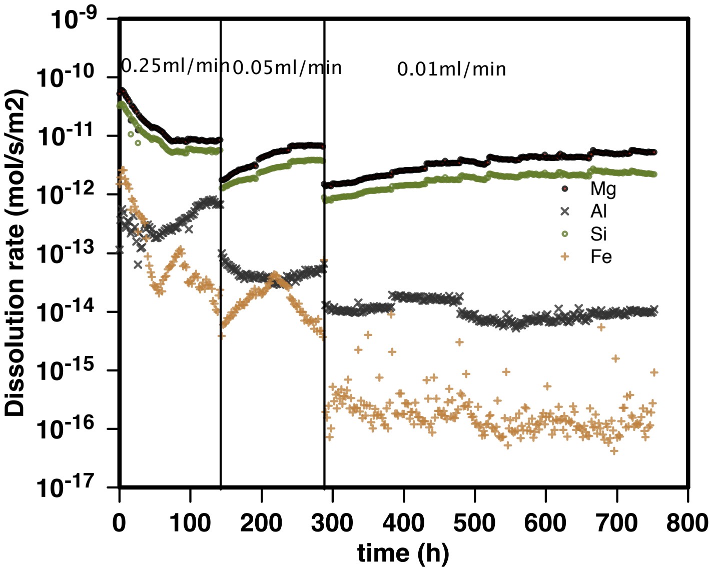

Figure 4.4 Dissolution rates determined by individual elements in 60 bar CO_2- saturated water at 100 °C. The calculated dissolution rates generally remain unchanged at steady states, despite the saturation index of chlorite being larger in the slow flow rate condition than in the high flow rate condition. This indicates that the mineral is at far from equilibrium conditions at all three flow rates, and the dissolution rate is not sensitive to the thermodynamic driving force for the conditions of these experiments.

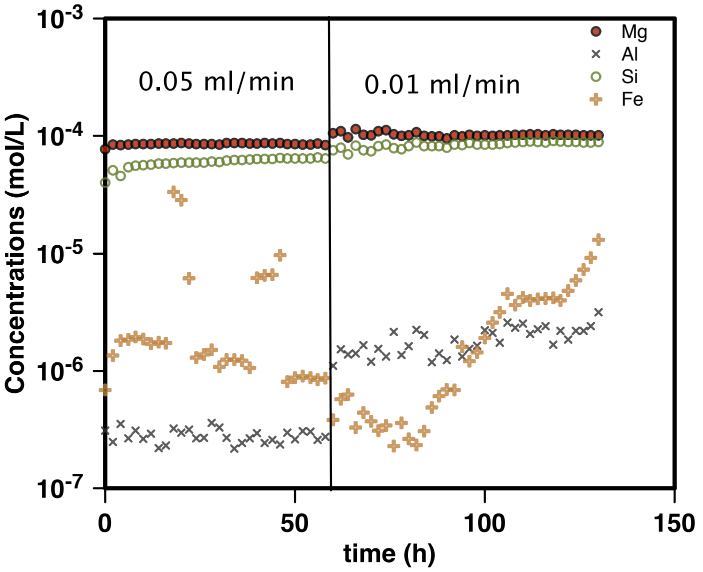

Figure 4.5 Concentrations of effluent elements for chlorite dissolution in 0.01M NaCl water at pH ~7 and 100 ^{o}C. In comparison with Figure 4.3, the concentration profiles of Mg and Si at steady states showed an increase of 1.25 times rather than the proportional increase of 5 expected from the decrease in flow rate expected if far from equilibrium conditions applied.

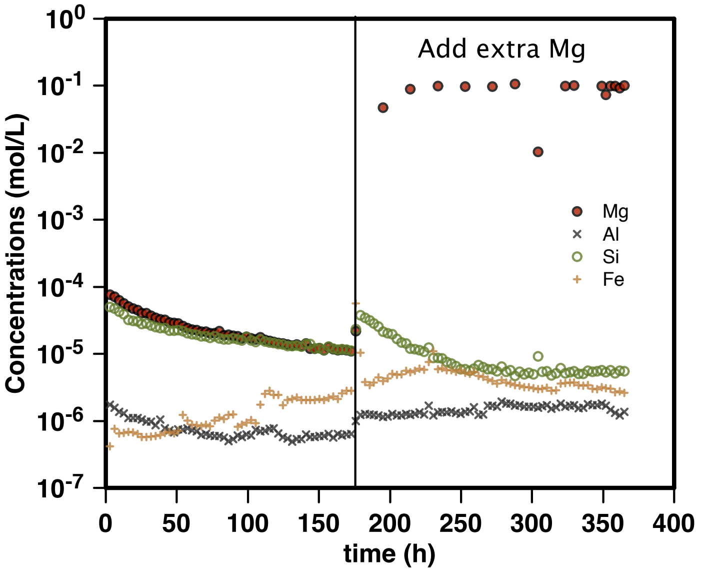

Figure 4.6 Change of effluent concentrations in experiments where extra $MgCl_2$ is added after near-steady state conditions are achieved. Decreased outflow Si concentrations at steady state are observed, which indicates a decrease of the dissolution rate of chlorite due to the increase in the saturation index of chlorite generated by the added Mg^{2+}.

4.4.5 Dependence of chlorite dissolution rate on pH

Since the pH and Gibbs free energy effects are intertwined in the overall kinetic rate expression, in order to evaluate the effect of Gibbs free energy on chlorite dissolution kinetics, we need to first determine the dependence of dissolution rate on pH so as to normalize and isolate its effects. Similarly, the effects of Gibbs free energy have to be isolated during pH dependence determination. For this purpose, we used experimental data that were all at far-from-equilibrium conditions, where the Gibbs free energy terms $f(\Delta G_r)$ were all at one, to obtain the pH dependence. Following Chou and Wollast (1985), the relationship between the rate and pH can be described by:

$$R_d = k_H a_H^n + k_{H_2O} + k_{OH} a_{OH}^m = k_H a_H^n + k_{H_2O} + k_{OH}^* / a_H^m \tag{4.12}$$

where R_d is the overall dissolution rate of chlorite [$mol(mineral)/m^2/s$], k_H, k_{OH} and k_{H2O} are the acid enhanced, hydroxide enhanced and water hydrolysis dissolution rate constants with k^*_{0H} representing the hydroxide-enhanced dissolution rate constant expressed in terms of hydrogen ion. The terms a_H and a_{OH} are the activities for the hydrogen and hydroxide ions, respectively, and n and m are the reaction orders with respect to the hydrogen and hydroxide ions.

As shown above (Equation 4.2), Lowson et al. (2005) fitted their dissolution rates as a function of pH at room temperature with the equation:

$$R_d = 10^{-9.79} a_{H^+}^{0.49} + 10^{-13.00} + 10^{-16.79} / a_{H^+}^{0.43}$$

Smith et al. (2013) expanded the equation to high temperature, but only within the acidic region, where they found

$$rate = k_{acid} \exp[(\frac{-E_{acid}}{R})(\frac{1}{T} - \frac{1}{298K})] a_{H^+}^n \tag{4.13}$$

$log\ k_{acid,298K} = -9.91\ mol/m^2/s,\ E_{acid} = 25.1\ kJ/mol,\ n = 0.488$

In fitting the measured dissolution rates as a function of pH, the assumption is that all rates are at far-from-equilibrium conditions and hence there are no chemical affinity effects. However, if the dissolution rates do not correspond to far-from-equilibrium conditions, the pH effects are intertwined with the chemical affinity effects. After careful examination, we found that the experiments of Smith et al (2013) were indeed at far-from-equilibrium conditions. The values of ΔG_r in Smith et al. (2013) are estimated using their reported dissolution rates, and assuming that all the other elements are released congruently. This might overestimate the concentrations of Al and Fe in the solution, but since the results are already far from equilibrium, and lower concentrations of Al and Fe would only result in more undersaturation, which would not affect the conclusion of this study.

However, not all of the experiments from Lowson et al. (2007) were at far-from equilibrium conditions, even though the saturation index log(IAP/K) in their experiments at 95 °C were thought to be in the range -13.5 to -55.0. Although these values would correspond to far-from-equilibrium conditions according to the standard linear form of the transition state theory rate formulation, our results and the following considerations suggest that these ΔG_r values are not on the dissolution plateau and therefore not far from equilibrium.

(1) Studies of the dependence of the dissolution rate of clay minerals on chemical affinity have shown that dissolution begins to be slowed at values of $\Delta G_r \approx -125.5\ kJ/mol$ for both smectite and montmorillonite (Cama et al., 2000). This corresponds to a saturation index of approximately $log(IAP/K) \approx -17$. Since chlorite, smectite and montmorillonite are all phyllosilicates (or sheet silicates), it is possible that chlorite dissolution could behave in a similar way.

(2) The reaction equilibrium constant K_{eq} was not well defined in previous studies, especially for intermediate Mg, Fe chlorite compositions used in the study of Lowson et al. (2007). Lowson et al. (2007) used the data from Kittrick (1982) who measured the solubility of two chlorites and determined that $logK_{eq}=42.3$ at 25 °C. However, the chlorite composition in Lowson et al. (2007) is

$(Mg_{2.76}Fe(II)_{1.90}Fe(III)_{0.07}Al_{0.97})[Si_{2.48}Al_{1.52}O_{10}](OH)_8$

while none of the samples in Kittrick (1982) has a composition close to this. For example, the stoichiometric number of Fe^{2+} in Lowson et al. (2007) is 1.90, while the samples in Kittrick (1982) have Fe^{2+} of 0.99, 0.57, 3.29, 2.61 respectively. There are only a few measured thermodynamic data available for chlorite minerals to our knowledge. The structural formulas of chlorite reported in available thermodynamic studies are listed in Table 4.3. Among them, Gailhanou et al (2009) used a chlorite that has the closest composition to that from Lowson et al. (2007)

($(Mg_{2.952}Fe(II)_{1.712}Fe(III)_{0.215}Al_{1.116})[Si_{2.633}Al_{1.367}O_{10}](OH)_8$ (compared to

$(Mg_{2.76}Fe(II)_{1.90}Fe(III)_{0.07}Al_{0.97})[Si_{2.48}Al_{1.52}O_{10}](OH)_8)$).

Table 4.3 Structural formula of chlorite reported from previous kinetic and thermodynamic studies compared with the one in the current study

	Current study	(Smith et al., 2013)	(Lowson et al., 2007)	(Gailhanou et al., 2009)	(Kittrick, 1982)				(Saccocia and Seyfried Jr, 1994)		(Aja, 2002)		
Si	2.96	2.78	2.48	2.633	2.97	2.99	2.47	2.84	2.945	2.56	2.83	2.815	2.63
Al	2.27	2.7	2.49	2.483	2.47	2.4	3.13	2.91	2.058	2.642	2.335	2.675	2.34
Fe^{2+}	0.12	0.1	1.9	1.712	0.99	0.57	3.29	2.61	0.454	2.297	0.5	0.3	3.08
Fe^{3+}	0	0	0.07	0.215	0.07	0.21	0	0.12	0.131	0.277	0.07	2.715	0.28
Mg	4.45	4.29	2.76	2.952	3.24	3.52	1.05	1.16	4.357	2.162	4.2	1.15	1.025
Mn	0	0	0	0.012	0	0	0	0	0.009	0.033	0.005	0.025	0.025
Ca	0	0	0	0.011	0	0	0	0	0	0	0.01	0.015	0.155

Gailhanou et al.(2007) obtained a Gibbs free energy of formation for chlorite to be -7607.1 kJ/mol at room temperature and pressure based on corresponding enthalpy and entropy of formation (-8253.70kJ/mol and -2170J/mol/K respectively). Thermodynamic parameters of this chlorite are listed in Table 4.4together with those for aqueous species from Anderson(2005). The dissolution Gibbs free energy of the chlorite used in the study of Lowson et al. (2007) is calculated to be -310.2 kJ/mol at standard state using those parameters. This corresponds to $logK_{eq}=52.3$ at 25°C. The corresponding equilibrium constant at 95°C is calculated to be $logK_{eq}(95^{o}C)=33.6$ using the Van't Hoff equation.

Table 4.4 Thermodynamic calculations of the ΔGr value at 25 °C of the chlorite sample from Lowson et al. (2007) using thermodynamic data from Gailhanou et al.(2007) for chlorite and Anderson(2005) for aqueous species.

	Chlorite	H^+	SiO_2(aq)	Al^{3+}	Mg^{2+}	Fe^{2+}	Fe^{3+}	Mn^{2+}	Ca^{2+}	H_2O	SUM
stoichiometric	-1	-17.468	2.633	2.483	2.952	1.712	0.215	0.012	0.011	12.734	
S_o (J/mol)	468.4	0.0	75.3	-321.7	-138.1	-137.7	-315.9	-73.6	-53.1	69.9	
ΔrS_o (J/mol)	-468.4	0.0	198.3	-798.8	-407.7	-235.7	-67.9	-0.9	-0.6	890.2	-891.5
ΔfH_o (kJ/mol)	-8253.7	0.0	-877.7	-531.0	-466.9	-89.1	-48.5	-220.8	-542.8	-285.8	
ΔrH_o (kJ/mol)	8253.7	0.0	-2311.0	-1318.5	-1378.1	-152.5	-10.4	-2.6	-6.0	-3639.8	-565.2
ΔfG_o (kJ/mol)	-7607.1	0.0	-833.4	-485.0	-454.8	-78.9	-4.7	-228.1	-553.6	-237.1	
ΔrG_o (kJ/mol)	7607.1	0.0	-2194.4	-1204.3	-1342.6	-135.1	-1.0	-2.7	-6.1	-3019.6	-298.6

We used this lower value of the equilibrium constant at 95°C to recalculate the chemical affinity of the experiments in the Lowson et al. (2007) study. Table 4.5listed all the experimental runs in Lowson et al. (2007) that were carried out under acidic to neutral pH values at 95°C. The first two runs at pH 3.26 and 4.21 in acid solutions were indeed quite far from equilibrium (*log Q/K=-55.0* and *-45.2* respectively). The experimental run at pH 6.59 was not recalculated due to lack of stability constant values for the buffer phthalate. The experiments at pH 5.56 and 6.9 were recalculated using the same PHREEQC code and database as in Lowson et al. (2007) and the new $logK_{eq}(95^{o}C)$ *of 33.6*. The new saturation indices with respect to chlorite were calculated to be -3.74 and -0.92 respectively, which were actually closer to equilibrium. Under these conditions, one expects a dependence of the rate on chemical affinity.

Table 4.5 Recalculation of saturation indices for the experiments in Lowson et al. (2007)

Buffer concentration	pH	Al (mg/L)	Fe (mg/L)	Mg (mg/L)	Si (mg/L)	log R (mol/m^2/s)	Log(Q/K) Lowson et al.	Log(Q/K) current
0.05M KHPhth	3.26	3.6	9.18	6.08	6.84	-10.9	-54.99	N/A
0.05M KHPhth	4.21	1.79	1.79	1.93	2.53	-11.49	-45.2	N/A
0.1 M H_3BO_3	5.56	0.03	0.03	0.32	0.58	-11.905	-18.72	-3.75
0.05M KHPhth, 0.02M NaOH	6.59	0.06	0.06	0.25	0.58	-12.123	-32.14	N/A
0.025M KH_2PO_4, 0.025M Na_2HPO_4	6.9	0.11	0.02	0.34	0.93	-12.171	-17.34	-0.93

To summarize, after a careful review of our experimental results and available literature data, only those data at far from equilibrium condition were used to determine the pH dependent dissolution rate expression. The data used for this purpose include all of those measured at acidic conditions (pH<4), two at $pH=4.16$ and 5.69 from Smith et al.(2013), one at $pH=4.21$ from Lowson et al. (2007), and two from our current study at $pH=4.89$ and 6.43 (squares in Figure 4.7). Using the equation in Chou and Wollast (1985), parameters k_H, n and k_{H2O} are determined using a least square method. According to these data, the pH dependence of the rate of chlorite dissolution under far from equilibrium conditions can be expressed as

$$R = 10^{-7.64} a_{H^+}^{1.05} + 10^{-11.56} \tag{4.14}$$

at 100 °C in acidic to neutral conditions.

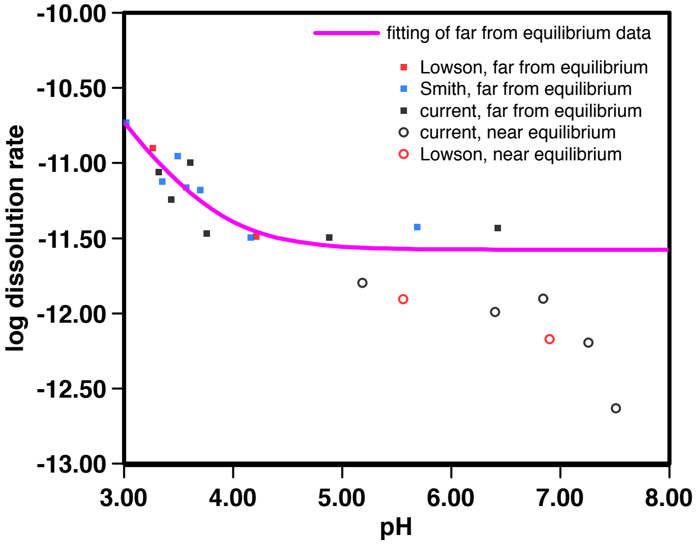

Figure 4.7 Fitting of chlorite dissolution rates as a function of pH. Only experimental data at far from equilibrium conditions (solid squares) are used for the fitting purpose to make sure that the equilibrium effects are not intertwined. Dissolution rates under near equilibrium conditions are smaller than expected from the pure pH curve.

4.4.6 Dependence of chlorite dissolution rate on Gibbs free energy

The effect of Gibbs free energy (chemical affinity) on the chlorite dissolution kinetic rate equation ($f(\Delta G_r)$ term in Equation 4.3) was evaluated by isolating the corresponding pH effects first and then compared and fitted within the framework of general transition state theory. To do this, the experiment dissolution rates measured were normalized first by dividing against the calculated rates at corresponding pH values from far-from-equilibrium conditions (with chemical affinity term, $f(\Delta G_r)$, as 1) according to the pH effect equation obtained above (Equation 4.14). The results obtained then were the pure $f(\Delta G_r)$ effect term in the rate equation with its value close to 1 representing the far-from-equilibrium condition and a value less than 1 showing the corrections from Gibbs free energy effects (the departure from equilibrium). The ΔG_r values were calculated for each experiment using

PHREEQC considering the same species as in Table 3 of Lowson et al. (2007). The corrected pH under experimental conditions is used in the calculation of ΔG_r . The chemical affinity term $f(\Delta G_r)$ and the corresponding Gibbs free energies of reaction for the steady state of each experiment are listed in Table 4.6 and plotted in Figure 4.8.

Table 4.6 Data used to determine the relationship between f(ΔGr) and ΔGr in Figure 4.8

	pH	ΔGr(kJ/mol)	Measured rate (10^{-12} mol/m^2/s)	Corresponding far-from-equilibrium rate (10^{-12} mol/m^2/s)	f(ΔGr)
0bar0.25ml/min	6.842	-78.15	1.25	2.77	0.45
0bar0.05ml/min	7.257	-46.50	0.64	2.77	0.23
0bar0.01ml/min	7.508	-15.07	0.24	2.77	0.084
0.1bar0.25ml/min	4.89	-113.94	3.19	2.94	1.08
0.1bar0.25ml/min($MgCl_2$)	5.19	-68.00	1.59	2.85	0.56
0bar0.01ml/min	6.402	-28.36	1.02	2.78	0.37
Lowson et al (2007)	5.56	-26.77	1.24	2.81	0.44
Lowson et al (2007)	6.90	-6.63	0.68	2.77	0.24
Smith et al (2013)	4.16	-139.15	3.19	3.75	0.85
Smith et al (2013)	3.70	-174.87	6.60	5.76	1.15
Smith et al (2013)	3.57	-181.80	6.84	6.86	1.00
Smith et al (2013)	3.02	-200.37	18.60	18.2	1.02

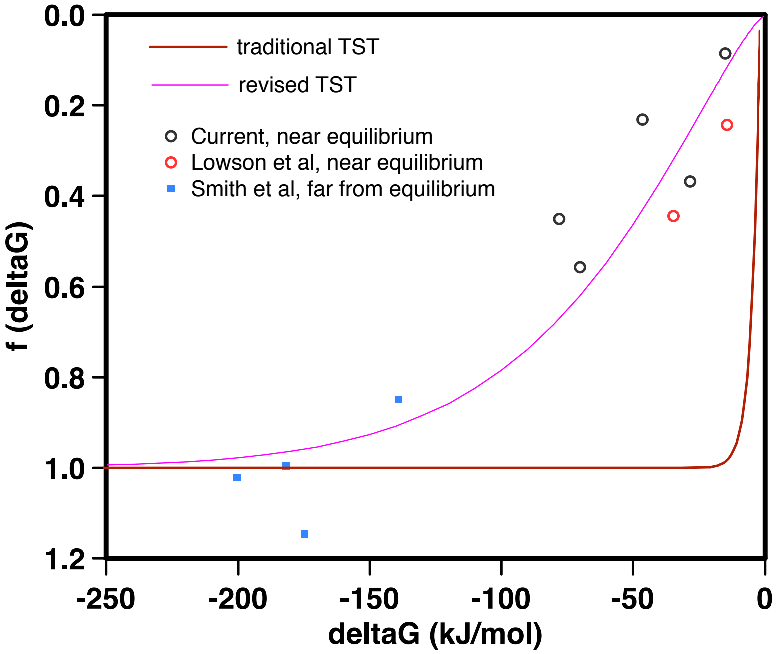

Figure 4.8 Fitting of rate reduction factor f(ΔGr) as a function of ΔG determined from the pressent study using the empirical law of Nagy and Lasaga (1992) compared with the linear transition state theory kinetic law. The chlorite dissolution rate increases as a function of the Gibbs free energy over a larger range than expected from linear TST.

The *f(ΔG$_r$)* determined in this way (Figure 4.8) decreased gradually from 1 to 0 between $\Delta G_r = 0$ and $\Delta G_r \approx -100$ kJ/mol. This behavior contrasts with that expected from a linear transition state theory (red curve in Figure 4.8). Following the approach by Nagy and Lasaga (1992), we described the chlorite rate dependence on the degree of undersaturation by fitting the experimental data to Equation 4.7.

$$f(\Delta G_r) = 1 - \exp[m(\frac{|\Delta G_r|}{RT})^n] \tag{4.7}$$

The coefficients: *m,* and *n* were calculated from a nonlinear least square regression fitting. The regression coefficient $R^2=0.83$ and the resulting coefficients are $m=-0.01677$ and $n=1.3$. Substituting the resulting coefficients gives

$$f(\Delta G_r) = 1 - \exp[-0.01677(\frac{|\Delta G_r|}{RT})^{1.3}] \tag{4.15}$$

The good comparison of the prediction from Equation 4.15 and the experimental data is shown in Figure 4.8. The shape of the curve and the critical free energy where dissolution rate starts to decrease (the edge of the dissolution plateau) were determined primarily by the data at near equilibrium conditions. In Figure 4.8, those data include 5 points from our current experiment study and two experimental points from Lowson et al. (2007) at close to equilibrium conditions ($\Delta G_r=-6.63 kJ/mol$, and $-26.77 kJ/mol$). Figure 4.8 shows that the chemical affinity term starts to show significant effects when the reaction Gibbs free energy, $/\Delta G_r/$, falls less than 100kJ/mol.

Combining the effects of Gibbs free energy and pH, we obtained a general rate law for chlorite dissolution at 100 °C in acidic to neutral conditions as:

$$R = (10^{-7.64} a_H^{1.05} + 10^{-11.56})\{1 - \exp[-0.01677(\frac{|\Delta G_r|}{RT})^{1.3}]\} \tag{4.16}$$

The comparison of measured dissolution rates and predicted rates using both the current rate law and the rate law from Smith et al (2013) are plotted in Figure 4.9. Since the rate law in Smith et al (2013) is for far-from-equilibrium dissolution of chlorite, the predicted rates are larger than the experimental rates. The addition of the modeled f(ΔGr) term in the current rate law improves the predicted dissolution rates for the near-equilibrium data.

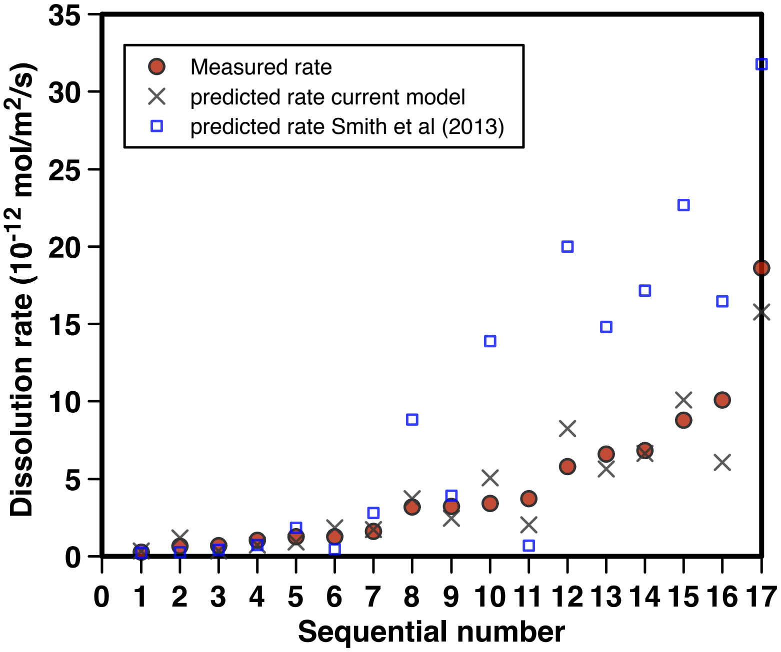

Figure 4.9 Comparison of measured dissolution rates and predicted rates using both the current model and the model from Smith et al (2013). Since the model in Smith et al (2013) is for far-from-equilibrium dissolution of chlorite, the predicted rates are larger than the experimental rates. The addition of the f(ΔGr) term in the current model improves the predicted dissolution rates for the near-equilibrium data.

There might be variable explanations for the shape of the f(ΔG_r) versus ΔG_r curve determined in this study. The first order implication is that different dissolution mechanisms are needed against transition state theory, such as a dislocation-assisted dissolution (Nagy and Lasaga, 1992). (Burch et al., 1993) observed that for albite dissolution there is a narrow range of undersaturation where rate increases sharply with decreasing ΔG_r, and near-equilibrium rate are dependent on ΔG_r to a much lesser extent. They proposed to use parallel overall reactions and dislocations to explain their data. Our experiments do not show the narrow range of ΔG_r where dissolution rate changes sharply, but rather the rate changes over a large range of $\Delta G_{r.}$ If the dissolution is indeed by a dislocation mechanism, the transition state theory cannot be used to describe the measured dissolution rate as a function of saturation state since dislocations are thermodynamically irreversible defects.

4.4.7 Implications for CO_2 sequestration

Chlorite is a common divalent cation-bearing mineral in sedimentary rocks and hence its dissolution kinetics is important for understanding the fate of trapped CO_2 in the context of geologic carbon storage. The measured dissolution rate of chlorite in our study is about 10^{-11} mole/m^2/sec at *pH=3.3-3.4,* which is the pH for CO_2 saturated brine. If we consider 1 m^3 of chlorite-bearing sands with a rock density of 2800 kg/m^3, Landrot et al. (2012) measured that 8.3% of the rock is chlorite, and 31.8% of chlorite is accessible, then the mass of accessible chlorite in 1 m^3 of rock m_0= *73.9kg*. Using threactive surface area of chlorite measured by Landrot et al.(2012) ($A_0=11.62 \times 10^{-2} m^2/g$), on a time scale of 1000 years, the amount of dissolved chlorite would be about 115 moles, and the total amount of released Mg and Fe would be 575 moles. Assuming 10% of the rock volume is filled with capillary-trapped supercritical CO_2 which has a density of 600 kg/m^3, the total amount of CO_2 in 1 m^3 rock is 1364 moles. Therefore, the released Mg and Fe from chlorite in such sandstones could provide enough cations to potentially mineralize about half the stored CO_2 in this volume within 1000 years.

The above calculation is important because it shows that mineralization of CO_2 could be substantial in a long term, contrary to the common view that only minor chemical reactions will happen for CO_2 sequestration. The calculation is based on the assumption that pH $\approx$ 3.3-3.4, and that brine is far from equilibrium with respect to chlorite. The dissolution rate of chlorite would be inhibited if pH is increased or if brine is concentrated and close to equilibrium for chlorite. The general rate law in this study provides inputs for reactive transport simulation to calculate the amount of mineral dissolution under these circumstances.

4.5 Conclusions

The dissolution rate of Flagstaff Hill chlorite (CCa-2) was examined using a well-mixed flow-through reactor. The experiments were conducted at 100 ^oC, pH from 3-7.5 and a range of pCO_2 from 0 to 60 bars, and variable degree of saturation state. The average Mg/Si ratio in outflow samples is in good agreement with the molar ratio in the mineral, indicating stoichiometric dissolution of chlorite.

Chlorite dissolution rates were analyzed and fitted as functions of pH and chemical affinity (ΔG_r). Only the data that were under far from equilibrium conditions are used in fitting the relationship between dissolution rate and pH so as to ensure that the near equilibrium (ΔG_r) effects were not included. Using this approach, the effects of chemical affinity on the dissolution rate of chlorite have been determined for the first time. Results show that the experimental data can be fitted by an empirical nonlinear rate law within the framework of transition state theory as shown in Nagy and Lasaga (1992). The chlorite dissolution rate varied as a function of the Gibbs free energy over a larger range ($-\Delta G_r >$100 kJ/mol) than expected from a linear TST rate law, and was similar to the dissolution rate formulation determined for smectite ($-\Delta G_r >$130 kJ/mol) (Cama et al., 2000). Our results indicate that chlorite dissolution is inhibited under a wide range of saturation conditions and might explain the fact that a low reactivity of Cranfield rock was measured by Lu et al. (2012) in batch experiments even though a high reactive surface area was determined by Landrot et al. (2012).

Chapter 5 Reactive transport modeling of stable carbon isotope fractionation in a multi-phase multi-component system during carbon sequestration

5.1 Introduction

In this chapter, we present a numerical tool for modeling the transport of stable carbon isotopes in groundwater reactive systems, in addition to standard geochemical parameters such as pH and chemical concentrations. The isotopic composition of the injected CO_2 may provide an ideal tracer for the assessment of the movement and the fate of injected CO_2 in the reservoir. If the CO_2 injected into mature oil-fields, saline aquifers or un-mineable coal seams has isotope ratios that are significantly different from those of naturally occurring carbon compounds in the reservoir, then $\delta^{13}C$ values constitute a tracer for following the movement and reactions of injected CO_2 in the reservoir (Assayag et al., 2009; Emberley et al., 2005; Johnson et al., 2011; Myrttinen et al., 2010; Raistrick et al., 2006).

Subsurface CO_2 sequestration involves complicated processes including multiphase flow, fluid phase chemical exchange, solute transport and chemical reactions involving minerals in the rocks. Interpretations of carbon isotope data are difficult without a comprehensive model. Analytical models incorporating isotopes have been utilized for a variety of conditions to identify sources, transport and reactivity in near-surface environments (DePaolo, 2006; Johnson and DePaolo, 1994). While these models accurately reproduce the measured trends in isotope ratios of natural systems, simplifying assumptions limiting flow and reactivity to a few basic components are required. As computing power has grown, treatment of complex hydrogeochemical systems has developed into reactive transport models coupling hydrology, chemistry and biology as a means of improved integration and analysis (Steefel et al., 2005). Multi-component reactive transport models such as TOUGHREACT (Xu et al., 2004) and CrunchFlow (Steefel, 2007) integrate hydrologic transport, aqueous and surface complexation and dissolution/precipitation into a comprehensive network of kinetic and equilibrium pathways. Incorporation of isotopic ratios into such multi-component models has been demonstrated in analysis of vadose zone infiltration rates from temperature dependent equilibrium fractionation of water isotopes (Singleton et al., 2004), plagioclase dissolution from uranium-series isotopes (Maher et al., 2006) and recently the influence of hydrologic transport on measured isotope fractionation in compound-specific stable isotope analysis (Rolle et al., 2010).

Examples of stable carbon isotope fractionations directly calculated in multi-phase multi-component reactive transport models for application to CO_2 sequestration are scarce. Johnson et al. (2009) reported field data of carbon isotope ratios during two sequestration projects, and used a simple two end-member mixing model to interpret their data. The model shows consistent trends with observed data, but do not match some observations especially the initial change of isotope signature after CO_2 is injected. The two main objectives of this chapter are to 1) verify the validity of the numerical model to simultaneously simulate multiphase flow, multispecies transport, and phase partitioning together with isotope fractionation and 2) to demonstrate the effects of the multiphase flow and phase partitioning on the spatial and temporal distributions of isotopic signatures. We show that the exchange of carbon isotopes between dissolved and gaseous carbon species, and between fluids (brine and supercritical CO_2), combined with fluid flow and transport, produce isotopic effects that are significantly different from simple two-component mixing. These effects are important for understanding the isotopic variations observed in field demonstrations. We submited this chapter to the Energy Procedia for the conference of GHGT12, titled *Reactive transport modeling of stable carbon isotope fractionation in a multi-phase multi-component system during carbon sequestration.*

5.2 Model development

TOUGHREACT is a multiphase, multidimensional reactive transport code applicable to geochemical problems involving kinetically controlled redox and mineral dissolution/precipitation reactions, along with equilibrium hydrolysis, aqueous complexation, ion exchange, and surface complexation reactions. The code couples the hydraulic transport capabilities of TOUGH2 (Pruess, 1991a) with reactive transport based on thermodynamic principles of chemical equilibrium and kinetics (Xu and Pruess, 2001b). Singleton et al (2004) extended TOUGHREACT to simulate oxygen and hydrogen isotope fractionation. In this study a similar approach is employed, allowing for an unlimited number of isotopes for any element to be tracked. Rather than accounting for isotopes as non-reactive tracers, TOUGHREACT isotope models treat the isotope species as reactive constituents within a multiphase transport model. For example, the primary dissolved carbon species considered in the original model is $H^{12}CO_3^-$. Here another primary species $H^{13}CO_3^-$ is created to represent the isotope species of ^{13}C. The general equilibrium reactions that link secondary species and gas phase species to primary species are also included in the database for ^{13}C as follows.

Secondary species
$^{12}CO_2(aq) + H_2O = H^+ + H^{12}CO_3^-$ $\quad$ $\log K_1(50^oC)= -6.3880$
$^{13}CO_2(aq) + H_2O = H^+ + H^{13}CO_3^-$ $\quad$ $\log K_1'(50^oC)= -6.38613654$

$^{12}CO_3^{-2} = - H^+ + H^{12}CO_3^-$ $\quad$ $\log K_2(50^oC)= 10.0840$
$^{13}CO_3^{-2} = - H^+ + H^{13}CO_3^-$ $\quad$ $\log K_2'(50^oC)= 10.08408685$

Gas phase
$^{12}CO_2(g) = -H_2O + H^+ + H^{12}CO_3^-$ $\quad$ $\log K_3(50^oC)= -8.3570$
$^{13}CO_2(g) = -H_2O + H^+ + H^{13}CO_3^-$ $\quad$ $\log K_3'(50^oC)= -8.354834$

Isotope exchange reactions are described by equilibrium constants, defined in the standard thermodynamic form as the quotient of the activities of the products and reactant. The equilibrium constants for the abundant species K_1, K_2, and K_3 are maintained from the existing TOUGHREACT database, while the equilibrium constant for the much less abundant, heavier isotopic species (K_1', K_2', K_3') are determined using the appropriate equilibrium isotopic fractionation factor α_{eq} as follows:

$^{13}CO_2(g)+^{12}CO_2(aq)=^{12}CO_2(g) +^{13}CO_2(aq)$ $\quad$ $\alpha_{eq1}(50^oC)= 1.0007$
$^{13}CO_2(g) +H^{12}CO_3^-(aq) =^{12}CO_2(g) +H^{13}CO_3^-(aq)$ $\quad$ $\alpha_{eq2}(50^oC)= 1.0050$
$^{13}CO_2(g)+^{12}CO_3^{2-}(aq) = ^{12}CO_2(g)+^{13}CO_3^{2-}(aq)$ $\quad$ $\alpha_{eq3}(50^oC)= 1.0052$

These equilibrium fractionation factors are calculated by Thode et al. (1965) at 50 ^{o}C.

5.3 Evolution of carbon isotope ratio in ideal systems

Johnson et al. (2009) reported field data of carbon isotope ratios in two carbon sequestration projects, one at Weyburn and the other at Pembina, Canada. They used the so-called gas mixture model to interpret measured isotope ratios and mole fraction of CO_2 in the gas phase. To understand the possible effects of the interaction between gas and water phases and the two-phase flow and transport processes on the evolution of carbon isotope ratio in the gas phase, it's essential to first understand how the carbon isotope ratio evolves in ideal systems including single-gas-phase batch models, two-phase batch models, and finally 1D two-phase flow and transport models.

5.3.1 Gas mixture model

Consider a batch vessel that is filled with $^{12}CO_2$, $^{13}CO_2$ and CH_4 gas. The initial mole fraction of CO_2 is M_{ini} =1.75%. Initial $\delta^{13}C$ in the gas phase is -16.9, which corresponds to a $^{13}CO_2/^{12}CO_2$ ratio R_{ini} equal to 0.01104728 (R_{std}=0.0112372). Thus the vessel is initially 1.7308784% $^{12}CO_2$, 0.019121518% $^{13}CO_2$, and 98.25% CH_4 in mole fraction. Then CO_2 is injected into the vessel, and this CO_2 has a higher $\delta^{13}C$ value of -4.5, which corresponds to a $^{13}CO_2/^{12}CO_2$ ratio R_{inj} equal to 0.011186632. The mole fraction of CO_2 in the vessel after CO_2 injection is

$$M_{CO_2} = \frac{N_{injCO_2} + N_{iniCO_2}}{N_{injCO_2} + N_{iniCO_2} + N_{iniCH_4}} = \frac{\dfrac{N_{injCO_2}}{N_{iniCO_2}} + 1}{\dfrac{N_{injCO_2}}{N_{iniCO_2}} + \dfrac{1}{M_{ini}}}$$

where N designates the number of molecules of each component. We define :

$$X = \frac{N_{injCO_2}}{N_{iniCO_2}} \approx \frac{N_{inj^{12}CO_2}}{N_{ini^{12}CO_2}}$$

Then

$$M_{CO_2} = \frac{X+1}{X+1/M_{ini}}$$

The ratio of $^{13}CO_2$ and $^{12}CO_2$ in the gas phase is

$$R_{gas} = \frac{N_{inj^{13}CO_2} + N_{ini^{13}CO_2}}{N_{inj^{12}CO_2} + N_{ini^{12}CO_2}} = \frac{R_{inj}X + R_{ini}}{X+1}$$

Converting to $\delta^{13}C$ values yields:

$$\delta_{gas} = \frac{\delta_{inj}X + \delta_{ini}}{X+1}$$

For each X value, M_{CO2} and δ_{gas} can be calculated and plotted versus each other as shown in Fig.5.1. Explicitly,

$$\delta_{gas} = \frac{1 - M_{CO_2}}{M_{CO_2} / M_{ini} - M_{CO_2}} \delta_{ini} + \frac{M_{CO_2} / M_{ini} - 1}{M_{CO_2} / M_{ini} - M_{CO_2}} \delta_{inj}$$

For the initial conditions and the isotope ratio of injected CO_2 stated at the start of this section, the relationship of δ_{gas} and M_{CO2} is plotted in Fig. 5.1 as a solid curve. The newly developed carbon isotope module of TOUGHREACT is also used to model the same process. Model results are plotted in Fig. 5.1. as circles, which lie exactly on the theoretical line.

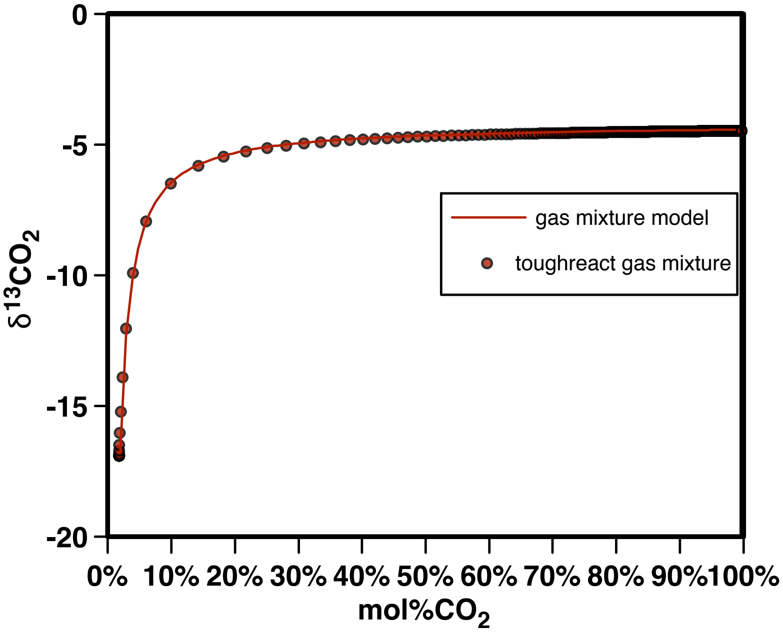

Figure 5.1 Theoretical gas mixture model and results from the newly develop TOUGHREACT code. The mole % of CO_2 is equivalent to 100X/(X+1) in the model.

5.3.2 Gas+water batch model

The $^{13}CO_2$ isotopic species preferentially goes into water relative to $^{12}CO_2$, so water is slightly enriched in ^{13}C relative to the gas phase. Thus, the existence of a water phase changes the mass balance in the gas phase and the evolution of the $\delta^{13}C$ signature. Below it will be illustrated how the equilibrium between gas and water phase affects the $\delta^{13}C$ of the gas phase.

Now we consider a slightly more complicated situation where the same batch vessel as in Section 3.1 is filled initially with 80% water and 20% gas by volume. The compositions of $^{12}CO_2$, $^{13}CO_2$ and CH_4 in the gas phase are the same as that in Section 5.3.1. If we assume (and this could be modified to account for kinetic transport effects) that the carbon species in the water phase are maintained at equilibrium with those in the gas phase, then

$$\frac{N_{^{13}C(aq)}}{N_{^{13}C(g)}} = K_{13}, \frac{N_{^{12}C(aq)}}{N_{^{12}C(g)}} = K_{12}$$

The equilibrium fractionation factor between aqueous phase and gas phase is:

$$\alpha_{aq-gas} = \frac{N_{{}^{13}C(aq)} / N_{{}^{12}C(aq)}}{N_{{}^{13}CO_2(g)} / N_{{}^{12}CO_2(g)}} = \frac{N_{{}^{13}C(aq)} / N_{{}^{13}CO_2(g)}}{N_{{}^{12}C(aq)} / N_{{}^{12}CO_2(g)}} = \frac{K_{13}}{K_{12}} = 1.0007 \sim 1.0052$$

where 1.0007 is the fractionation factor between CO_2(aq) and CO_2(g), and 1.0052 is the fractionation factor between CO_3^{2-}(aq) and CO_2(g).

Using $N_{12CO_2(g)inj}$ and $N_{13CO_2(g)inj}$ to designate the number of $^{12}CO_2$(g) and $^{13}CO_2$(g) molecules that are injected into the vessel, assume that N_{12Cdis} of $^{12}CO_2$(g) and N_{13Cdis} of $^{13}CO_2$(g) dissolves in the water phase, then

$$\frac{N_{{}^{12}C(aq)ini} + N_{{}^{12}Cdis}}{N_{{}^{12}CO_2(g)ini} + N_{{}^{12}CO_2(g)inj} - N_{{}^{12}Cdis}} = K_{12}$$

N_{12Cdis} can be solved as

$$N_{{}^{12}Cdis} = \frac{K_{12} N_{{}^{12}CO_2(g)ini} + K_{12} N_{{}^{12}CO_2(g)inj} - N_{{}^{12}C(aq)ini}}{1+K_{12}} = \frac{K_{12}}{1+K_{12}} N_{{}^{12}CO_2(g)inj}$$

The current number of $^{12}CO_2$(g) molecules in the gas phase is then

$$N_{{}^{12}CO_2(g)cur} = N_{{}^{12}CO_2(g)ini} - N_{{}^{12}Cdis} + N_{{}^{12}CO_2(g)inj} = N_{{}^{12}CO_2(g)ini} + \frac{1}{1+K_{12}} N_{{}^{12}CO_2(g)inj}$$

Similarly,

$$N_{{}^{13}CO_2(g)cur} = N_{{}^{13}CO_2(g)ini} + \frac{1}{1+K_{13}} N_{{}^{13}CO_2(g)inj}$$

where the term $N_{inj}/(1+K)$ is the effective number of molecules that stays in the gas phase, and accounts for $1/(1+K)$ of the total injected CO_2. The other fraction of $K/(1+K)$ goes into the water phase due to CO_2 dissolution.

The mole fraction of CO_2 in the gas phase is

$$M_{CO_2} = \frac{\frac{1}{1+K_{12}} N_{injCO_2} + N_{iniCO_2}}{\frac{1}{1+K_{12}} N_{injCO_2} + N_{iniCO_2} + N_{iniCH_4}} = \frac{\frac{1}{1+K_{12}} \frac{N_{injCO_2}}{N_{iniCO_2}} + 1}{\frac{1}{1+K_{12}} \frac{N_{injCO_2}}{N_{iniCO_2}} + \frac{1}{M_{ini}}} = \frac{\frac{X}{1+K_{12}} + 1}{\frac{X}{1+K_{12}} + \frac{1}{M_{ini}}}$$

The ratio of $^{13}CO_2$ and $^{12}CO_2$ in the gas phase is

$$R_{gas} = \frac{\frac{1}{1+K_{13}} N_{inj^{13}CO_2} + N_{ini^{13}CO_2}}{\frac{1}{1+K_{12}} N_{inj^{12}CO_2} + N_{ini^{12}CO_2}} = \frac{\frac{1}{1+K_{13}} R_{inj} X + R_{ini}}{\frac{1}{1+K_{12}} X + 1}$$

The final expression is illustrative in that when enough CO_2 is injected, $X \rightarrow \infty$

$$R_{gas} = \frac{\frac{1}{1+K_{13}} R_{inj} X + R_{ini}}{\frac{1}{1+K_{12}} X + 1} = \frac{\frac{1}{1+K_{13}} R_{inj} X}{\frac{1}{1+K_{12}} X} = \frac{1+K_{12}}{1+K_{13}} R_{inj}$$

The key to determining the final isotope ratio in this model would be the absolute values of K_{12} and K_{13}.

If $K_{12}, K_{13} << 1$,

$$R_{gas} = R_{inj}$$

This means that when most CO_2 is distributed in the gas phase, the effect of water is negligible, and the final ^{13}C ratio in the gas phase is the isotopic ratio of injected CO_2, as in the case of the gas mixture model. However, if $K_{12}, K_{13} >> 1$, in which case most of injected CO_2 dissolves in the water phase,

$$R_{gas} = \frac{K_{12}}{K_{13}} R_{inj} = \frac{1}{\alpha_{aq-gas}} R_{inj}$$

This means that when most of the injected CO_2 dissolves into water, the final ^{13}C isotope ratio in gas phase is 0.7-5.2‰ lower than the injected CO_2 due to fractionation of ^{13}C between the water phase and gas phase.

The parameter K_{12} is essentially the ratio of the number of carbon species in the aqueous phase over the number of CO_2 molecules in the gas phase. The absolute value of this ratio depends on the relative volume of water phase and gas phase in the batch vessel, and also on the chemistry of the water phase. In general, this ratio does not conform to either of the endmember cases discussed above. For example, for CO_2 dissolution in water, the Henry's Law coefficient at moderate temperature is about 200 MPa (approximately 2000 bar). If we assume that 1.0% of the gas phase is CO_2 with a total pressure of 100 bar, then the partial pressure of CO_2 is 1bar. According to Henry's Law, the mole fraction of dissolved CO_2 in the water phase is 1bar/200MPa=0.0005. If we consider a volume of 1L for the vessel with 80% filled with water, there will be 0.8L water and 0.2L gas. The molar density of water is 55 mol/L, then dissolved CO_2 is 0.8L x 55mol/L x 0.0005=0.022 mole. The number of CO_2 molecules in the gas phase is $n_{gas} \approx PV/RT \approx 10^5$Pa x 0.2L/(8.314J/mol/K x 300K)=0.008 mole. Hence, the ratio of carbon molecules in the aqueous phase and the gas phase is K_{12}=0.022/0.008=2.75.

The value of $K_{12} = 2.75$ is neither large enough to fully take all the carbon into the water phase from the gas phase, nor small enough to be neglected. However, CO_2 reacts with the water on dissolution and therefore one would expect that Henry's law has to be modified. Water with a high pH value would be expected to take more CO_2 than water with a lower pH. The K_{12} value for an initial water at pH 7.8 is 1.95 according to TOUGHREACT calculations. As CO_2 is injected, water pH decreases to 4.8 and the final K_{12} value is 1.90.

The value of K_{13} is equal to K_{12} times the fractionation factor α_{aq-gas} of ^{13}C isotope between aqueous phase and gas phase. Generally, HCO_3^-, CO_3^{2-}, and $CO_2(aq)$ are 5.0‰, 5.2‰ and 0.7‰ heavier than $CO_2(g)$ respectively, thus the fractionation factor between the total carbon species in water and in gas depends on the relative abundances of each species, which is affected by water pH. In acid conditions with pH<6 or alkaline conditions with pH>10, $CO_2(aq)$ or CO_3^{2-} dominates respectively in the water phase, so the total carbon in water is about 0.6‰ or 5.2‰ heavier than gas. In neutral pH range from 6 to 10, bicarbonate HCO_3^- dominates and the total carbon in water is about 5.0‰ heavier than that in gas.

Figure 5.2 shows the two end curves with initial K_{12} and α_{eq} values and final K_{12} and α_{eq} values. The dashed-dotted line represents the initial condition in the batch vessel at pH 7.8, K_{12}=1.95, and $\alpha_{aq\text{-}gas} \approx$ 1.005. The curve approaches a value around -7.8‰, which is 3.3‰ lower than injected CO_2 (-4.5‰). The dashed line represents the final state in the vessel when CO_2 reaches 95% in the gas phase with water pH=4.8, K_{12}=1.9, and $\alpha_{aq\text{-}gas} \approx$1.001. The curve reaches a limit around -5.1‰, which is only 0.6‰ lower than injected CO_2(-4.5‰).

During the process of injecting CO_2 into the batch as stated above, the values of K_{12} and $\alpha_{aq\text{-}gas}$ evolve with CO_2 injection due to the pH change. The exact theoretical expressions for K_{12} and $\alpha_{aq\text{-}gas}$ as a function of injected CO_2 are complicated to derive, but can be calculated using a numerical model with discrete time steps like the current code. The circles in Figure 5.2 are results from the carbon isotope module of TOUGHREACT developed in this study. The real evolution of ^{13}C isotope ratio and mole% of CO_2 lies between the two theoretical curves as expected. However, the model results approach the final end curve at a fairly early stage, indicating that $CO_2(aq)$ quickly starts to dominate in the aqueous phase due to the pH change.

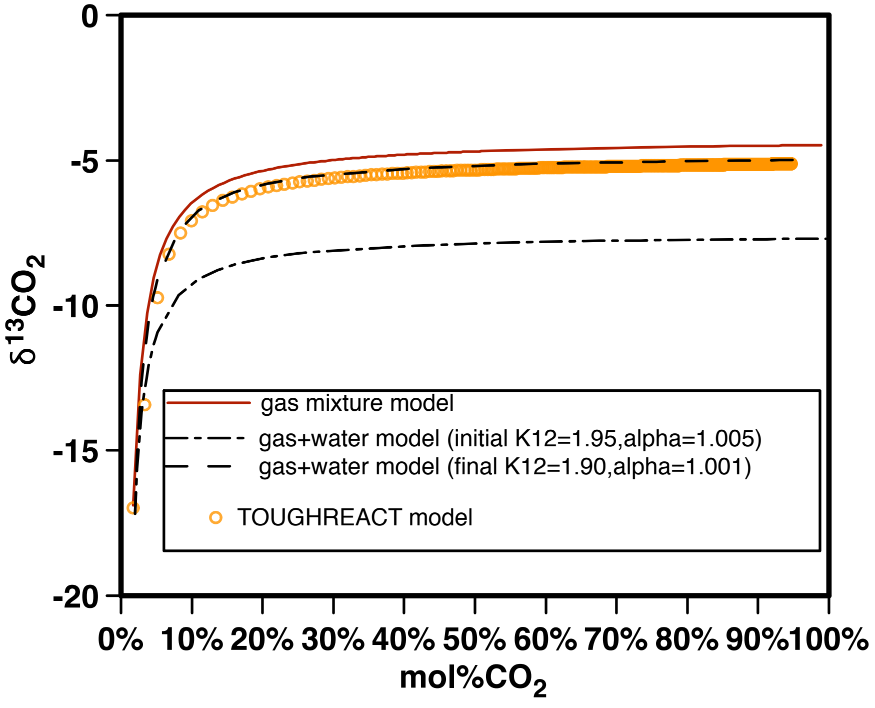

Figure 5.2 Theoretical gas+water batch model and model with TOUGHREACT

5.3.3 1D two-phase flow and transport model

In this section we consider a 1-dimensional flow and transport model where the model domain is divided into discrete grid blocks. The first grid block is used for CO_2 injection, and the last grid block is set at a constant boundary condition. The injected CO_2 flows from left to right, and replaces water. Initially water saturation is 0.75, and gas saturation is 0.25. Mole % CO_2 in the gas phase is 1.75%, and the other 98.25% is methane. Gas and water are assumed to be at equilibrium in each grid block at each time step. A sketch of the 1D flow problem is presented in Figure 5.3, and the parameters used for calculation are given in Table 5.1.

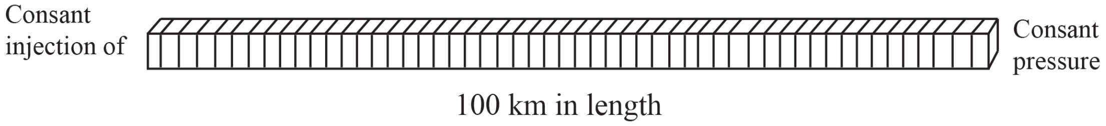

Figure 5.3 Sketch of the 1D two-phase flow and transport model

Table 5.1 Hydrological parameters used in the 1D radial flow and transport model.

Parameter	Value
Pressure	10 MPa
Temperature	50 °C
CO_2 injection rate	40 m^3/d
Initial gas saturation	0.25
Initial mole% of CO_2	1.75%
Initial $\delta^{13}CO_2$	-16.9
Injected $\delta^{13}CO_2$	-4.5
Porosity	0.174
Permeability	53.6 mD

Figure 5.4 shows the propagation of gas saturation and pH along the radial distance with time. Initially the gas saturation is 0.25 in the whole domain. As CO_2 is injected, the gas saturation near the injection well increases to 1.0. Generally, the gas saturation profile moves forward as time elapses. pH evolves in a similar pattern. The initial pH is 6.8, and decreases to 5.1 near the injection well due to CO_2 injection.

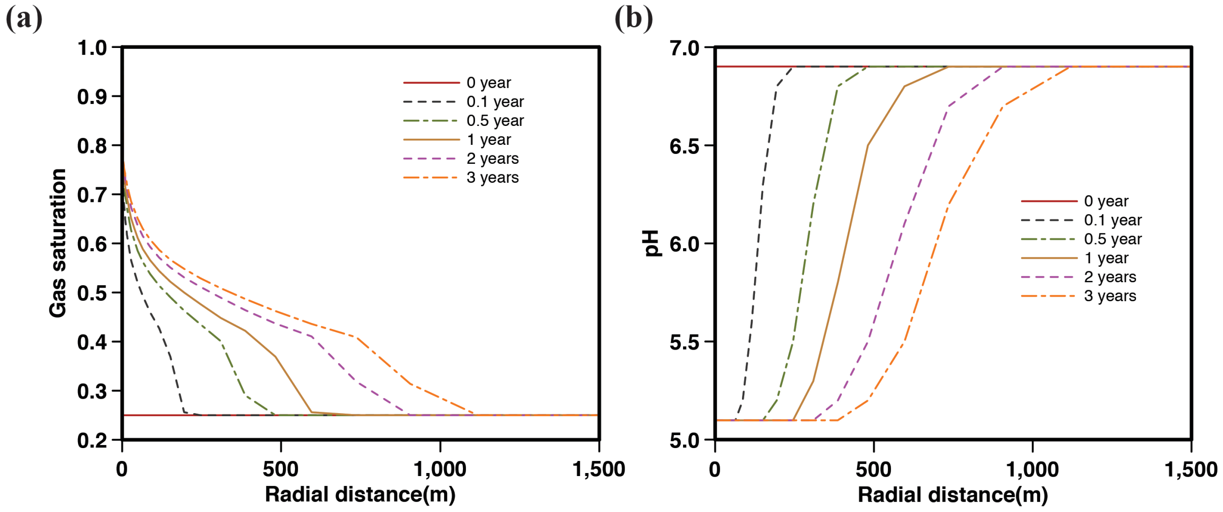

Figure 5.4 Profiles of gas saturation and pH along the radial distance evolving with time

Figure 5.5 presents the mole% of CO_2 and $\delta^{13}CO_2$ in the gas phase as a function of radial distance and time. Initially CO_2 accounts for 1.75% in the gas phase with an isotope ratio of -16.9. As CO_2 is injected, the mole% of CO_2 increases to 100%, while the isotope ratio increases to -4.3 near the injection well which is the isotope ratio in injected CO_2. The effect of fluid flow and transport on the relationship between $\delta^{13}CO_2$ and mole% of CO_2 will be discussed in Section 5.3.5.

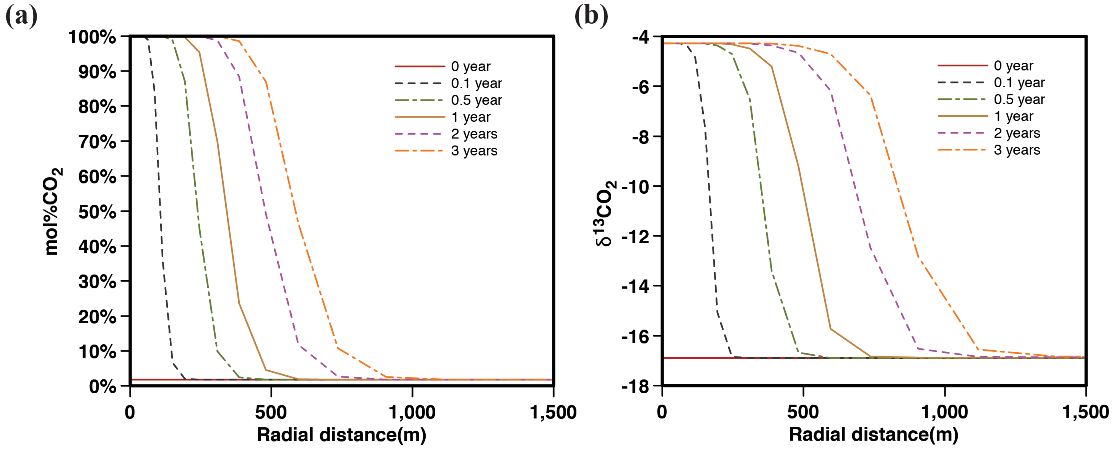

Figure 5.5 Profiles of mole% CO_2 and $\delta^{13}CO_2$ along the radial distance evolving with time

5.3.4 Calcite precipitation model

Calcite is about 8.4‰ heavier than CO_2 gas at equilibrium at 50 °C (Bottinga, 1968). Generally, for δ^{13}C, calcite>CO_3^{2-}>HCO_3^->CO_2(aq)>CO_2(g), with calcite being the heaviest, CO_2(g) being the lightest. So calcite would have the largest effect on the carbon isotope ratio in the gas phase, assuming that the kinetics of calcite dissolution or precipitation is fast enough. In the current TOUGHREACT model, we treat the carbonate mineral isotopologues as an ideal solid solution.

The condition of equilibrium for a solid solution is

$$Q_{ss}/(K_{ss}a_{ss})=1$$

where the subscript ss refers to the solid solution, and Q and K are the ion activity product and equilibrium constant for that solid solution respectively, and a is the activity of the solid solution. By convention, $a_{ss}=1$.

A similar expression can be written for the condition of equilibrium for each end-member of the solid solution:

$$Q_i/(K_i a_i)=1$$

In this case, the subscript i refers to each end member, and $a_i \neq 1$. In the case of an ideal solid solution, the activity of each endmember, a_i, is assumed to equal its mole fraction x_i in the solid solution. The kinetic law of mineral dissolution and precipitation is assumed to follow the simplest form of transition state theory,

$$R_i = k_i A(1-Q_i/(K_i x_i))$$

DePaolo (2011) developed a model that describes the effective isotopic fractionation factor for steady state precipitation as a function of deviation from equilibrium.

$$\alpha_p = \frac{\alpha_f}{1 + \frac{Q}{K}\left(\frac{\alpha_f}{\alpha_{eq}} - 1\right)}$$

This formulation was proposed for Ca isotopes in calcite, and it is not known whether it applies directly to C isotopes. We add it here to show how kinetic effects may come into play; the model can be easily adapted if different fractionation factors, or a different formulation are shown to be applicable in the future. The current model is verified relative to the DePaolo (2006) formula by modeling a series of precipitation scenarios with arbitrary values of the equilibrium (α_{eq}=1.009) and forward (α_f=0.9985) isotopic fractionation factors. The modeled effective fractionation factors are plotted versus (Q/K-1) and compared with the DePaolo (2011) model. Results show that using solid solution and transition state theory is able to accurately describe non-equilibrium isotope fractionation during mineral precipitation.

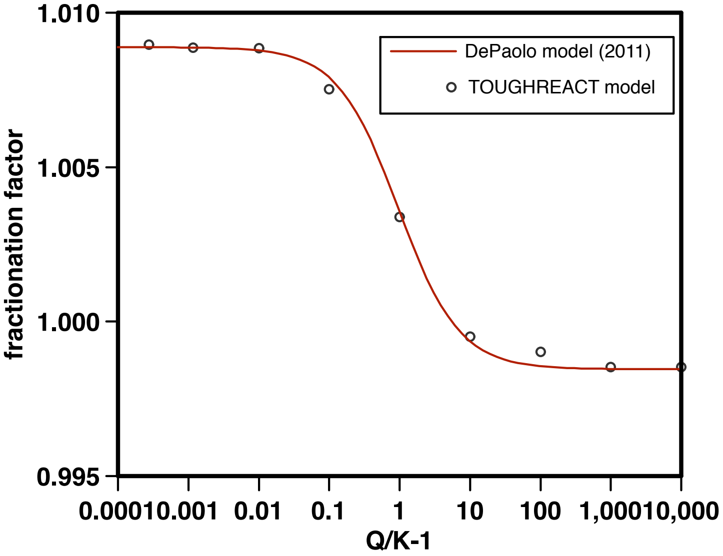

Figure 5.6 Effective isotopic fractionation factor as a function of deviation from equilibrium during mineral precipitation

5.3.5 Discussions

Johnson et al. (2009) reported field data for carbon isotope ratios during two carbon sequestration projects, one in Weyburn and the other in Pembina. They used a gas-mixture model to interpret the field data by plotting the ^{13}C isotope ratio in the gaseous CO_2 versus the mole fraction of CO_2 in the gas phase. Both data sets show that the carbon isotope signature arrives at the monitoring well earlier than expected from a gas mixture model, as indicated in Figure 5.7 where the field data from Pembina are plotted. For example, the field data (green crosses) show that carbon isotope ratio increases from its baseline value (-16.9 ‰) to the isotope ratio of injected CO_2 (-4.3 ‰) as the content of CO_2 increases due to injection, but the isotope ratio reaches -6 ‰ at a smaller value of CO_2 content than expected from the gas mixture model shown as the green solid line. This observation indicates that the change in carbon isotope ratio cannot be fully explained by the gas-mixture model from the change of CO_2 content in the gas phase.

As discussed in Section 5.3.2, the two-phase batch model shifts the theoretical curve down compared to the gas-mixture model due to fractionation of ^{13}C between the gas and aqueous phases. The 1D flow model in Section 5.3.3 shows a similar effect compared to the batch model, which is represented by the red dash line in Figure 5.7. The data are from one of the grid blocks downstream in the 1D flow model. The slight difference between the 1D flow model and the batch model is that the ^{13}C isotope ratio in the batch model is smaller than the gas-mixture model even when mole%CO_2 reaches 100%, while the 1D flow model eventually merges with the gas-mixture model when mole%CO_2 is close to 100%. The latter effect is because that the gas saturation in the 1D flow model is close to 1.0 when mole%CO_2 approaches 100%, and water is almost completely removed from the grid block. The 1D flow model is essentially the same as the gas-mixture model when gas saturation is close to 1.0, while the batch model accounts for 20% water.

However, if permeability is not as high as reported in the literature for the Pembina field, the 1D flow model would produce slightly different curves of $\delta^{13}C$ as a function of mole%CO_2. For example, if permeability is decreased by 5 orders of magnitude from the original value 53mD, the curve is shifted to the upper left in Figure 5.7, which is represented by the solid red line. The reason for this is that the low-permeability model has a different gas saturation profile compared with the base model as shown in Figure 5.8.

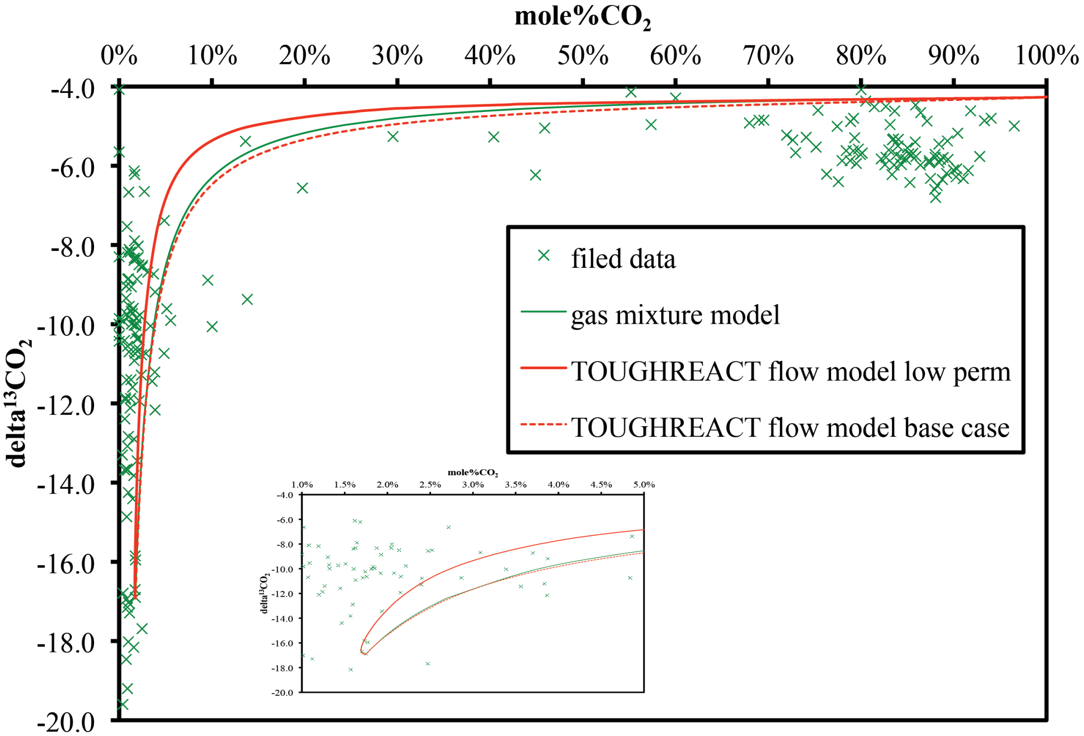

Figure 5.7 Time series field data of carbon isotope ratio and mole fraction of CO_2, and fitting with gas mixture model and current TOUGHREACT flow model

Figure 5.8 shows the propagation of gas saturation along the radial distance with time when permeability is decreased. Initially the gas saturation is 0.25 in the whole domain. As CO_2 is injected, the gas saturation near the injection well increases to 1.0. The difference between the low-permeability model and the base case model is that there is a low gas saturation region in the low-permeability model. For example, the gas saturation is below the initial gas saturation 0.25 around 500m at 3 years as shown in Figure 5.8. This decreased gas saturation increases the pressure in these grid blocks, and leads to more dissolution of gas into the aqueous phase. Since CO_2 and CH_4 have different Henry's coefficients, this enhanced dissolution changes the mole% of CO_2 in the gas phase. For example, the same batch model as in Section 5.3.2 was conducted but with water injected instead of CO_2 to increase total pressure from 100 bar to 124.2 bar. The amount of each component (H_2O, CO_2, $^{13}CO_2$, and CH_4) in the gas and aqueous phases are listed in Table 5.2 for both initial condition and final condition. As can be seen in Table 5.2, the mole%CO_2 decreased from 1.75% to 1.48% due to the pressure increase and gas dissolution. In the grid block from the 1D flow model, the mole%CO_2 decreases from 1.75% to 1.69% for the same reason. The slight decrease in initial mole%CO_2 changes the shape of the curve dramatically in Figure 5.7 and fits the field data somewhat better. Figure 5.7 also shows that large numbers of field data have mole%CO_2 that is smaller than the initial mole%CO_2 in the reservoir even after CO_2 injection. This agrees with the model with pressure increase and further dissolution of CO_2 and CH_4 in the aqueous phase. Thus, we suggest that either the permeability at Pembina is smaller than reported in the literature, or that there are localized low-permeability regions in the reservoir where pressure goes up and changes the relationship between isotope ratio and mole%CO_2.

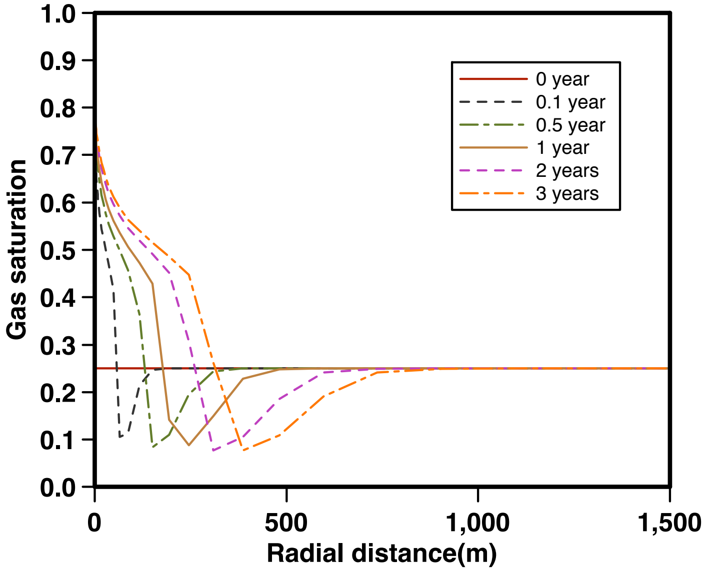

Figure 5.8 Profiles of gas saturation along the radial distance evolving with time in the low-permeability model

Table 5.2 Initial and final conditions of the two-phase batch model where water is injected to increase total pressure

Initial	Gas (moles)	Aqueous (moles)	Pressure (bar)
H_2O	3.27E+00	4.12E+06	
CO_2	1.78E+03	2.36E+03	1.73

$^{13}CO_2$	1.96E+01	2.61E+01	0.0191
CH_4	1.01E+05	6.81E+03	98.25
mole%CO_2	1.75%	Total pressure(bar)	100.00
Final	Gas (moles)	Aqueous (moles)	Pressure (bar)
H_2O	2.57E+00	4.42E+06	
CO_2	1.47E+03	2.67E+03	1.82
$^{13}CO_2$	1.62E+01	2.95E+01	0.0201
CH_4	9.88E+04	9.08E+03	122.37
mole%CO_2	1.48%	Total pressure(bar)	124.21

Besides the possible effects of permeability on the relationship between $\delta^{13}C$ and mole%CO_2, the initial value of mole%CO_2 might also change the curve significantly. The initial mole fraction of CO_2 in monitoring well 7-11 is 1.75%, and the range of this value in all monitoring wells is between 0.89% and 1.77%. If we use smaller values for the initial mole% of CO_2 in the model, the curve would be shifted to the left compared to the gas mixture model. However, to fully cover all the field data, the initial mol%CO_2 need to be decreased by 10 times to 0.175% as shown in Figure 5.9.

To conclude, low permeability and variability in initial mole fraction of CO_2 might be able to explain the measured isotope data in the Pembina project, while either of the reasons would require large changes from the base values measured in the field. Either permeability need to be decreased by 5 orders of magnitude, or initial mole percent of CO_2 need to be decreased by 10 times, to match the field data. There might be combined effects from the two parameters, and the uncertainty in field data also need to be further evaluated.

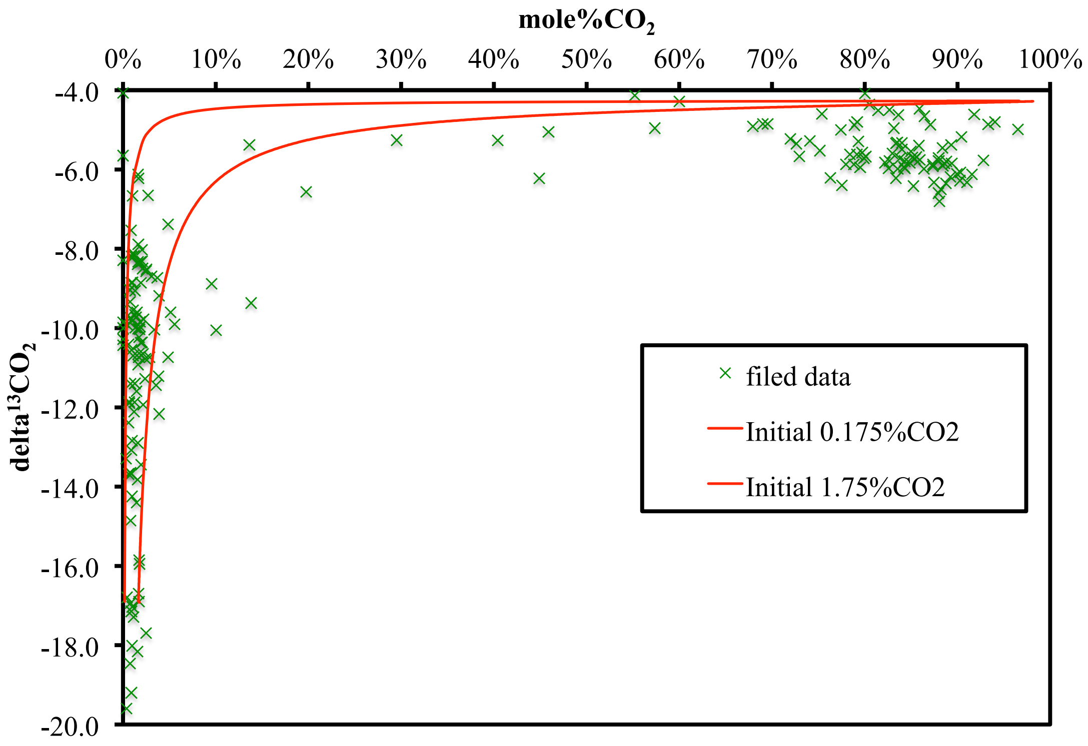

Figure 5.9 Fitting of $\delta^{13}C$ versus mol%CO_2 data using the gas mixture model with different initial mole fraction of CO_2

5.4 Time series data from the field

The development of the current isotope module of TOUGHREACT makes it possible to model carbon isotope evolution during carbon sequestration, while simultaneously keeping track of other geochemical and hydrological parameters as a function of time. A regular monthly geochemical monitoring program involving the collection and chemical and isotopic analysis of fluids and gases was conducted since February 2005 at the PennWest CO_2-EOR pilot, near Drayton Valley in Central Alberta. Six producing wells were sampled along with two control wells located outside of the pilot area. The operation is hosted in the Upper Cretaceous Cardium Formation of the Pembina oil field which is a siliciclastic reservoir at approximately 1650 m depth and reservoir temperature and pressure of 50°C and 19MPa respectively (Hitchon, 2009).

At the Pembina Cardium CO_2 Monitoring Pilot site, approximately 75,000 tons of CO_2 were delivered by truck and injected between 2005 and 2008 by two injector wells over two 5-spot patterns (1 injector, 4 producers) with 2 production wells being shared between the patterns (Hitchon, 2009). Injection on both wells varied with time. Injection wells were perforated in the conglomerate, upper and middle sands of the Cardium Formation, while production wells are either open-hole completed (10–11, 12–12) or are perforated throughout the whole stratigraphic succession (conglomerate to lower sand). Casing gas samples were obtained from the wellhead at the eight production wells sampled approximately monthly between February 2005 and March 2008. The baseline data were collected repeatedly between February and April 2005 allowing estimation of natural variability of various geochemical parameters. Following baseline sampling and the commencement of CO_2 injection, 15 monitoring events took place between May 2005 and January 2007. In February 2007 the EOR operation converted to a water alternating gas (WAG) regime and a further 13 monitoring events took place until March 2008. This paper focuses on the CO_2 injection phase only.

Monitored geochemical data are reported in John et al. (2001), Shevalier (2008) and several project reports. Four of the six producing wells, 07-11, 08-11, 09-11 and 12-12, show CO_2 breakthrough that occurs as early as May 2005, 66 days after CO_2 injection began. The remaining two wells, 10-11 and 05-12, and the two monitoring wells, 01-11 and 04-12, do not show signs of CO_2 breakthrough, but show that solubility trapping commences much later (July 2007). The first four wells (07-11, 08-11, 09-11, 12-12) show a decrease in pH to ~6.5 while the remaining wells (01-11, 10-11, 04-12, 05-12) have a fairly constant pH of ~7.5. The total alkalinity for all samples remained about constant. As with pH, the same four wells (07-11, 08-11, 09-11, 12-12) showed a general increase of calcium and iron concentrations over time while those of the remaining wells remained constant.

The CO_2 concentrations in the casing gas as a function of sampling dates are also obtained from monitoring trips. Initially the CO_2 concentrations were less than 2% for all wells. As with pH, four wells (07- 11, 08-11, 09-11, 12-12) showed an increase in CO_2 typically to more than 80% while the remaining four wells showed only a very minor increase in the CO_2 concentration. Initial $\delta^{13}C$-$CO_2(g)$ values were below -15‰. As with nearly all the other monitoring parameters, the $\delta^{13}C$-$CO_2(g)$ values as a function of sampling dates from the same four wells (07-11, 08-11, 09-

11, 12-12) show a quick initial change in the $\delta^{13}C$ value while the remaining four change slowly. The measured $\delta^{13}C$ values of the injection CO_2 ranged between -1 and -5‰ throughout the observation period.

5.5 Reactive transport modeling and fitting with well data

In this study the 1D flow and transport model is used for simulating the monitored geochemical data and isotopic signatures during CO_2 sequestration. The 100 km model domain is divided into 60 radial grid blocks logarithmically. The first grid block is used for CO_2 injection, and the last grid block is set to constant conditions to serve as a sink of CO_2 gas.

The field data fall into two groups based on change of geochemistry. Four wells, 07-11, 08-11, 09-11 and 12-12, show decreased pH, increased Ca, Fe concentrations, and reach about 80% of CO_2 in the gas phase. Meanwhile the other four wells, 10-11, 05-12, 01-11 and 04-12, do not show signs of dramatic change in pH, concentrations, or CO_2 mole fraction in the gas phase. For simplicity, only the geochemical data from well 7-11 are used to represent the first group of data for fitting purposes. However, since the other three wells in the first group all show similar patterns in terms of geochemical parameters, models for the other three wells are expected to be similar.

Core samples were collected from well 7-11 before CO_2 flooding. Analysis shows that porosity is about 17.4%, and permeability is about 53.6mD. Initially water saturation is 0.353, oil saturation is 0.4, and gas saturation is 0.247. Mole % of CO_2 in the gas phase is 1.75%, with most of the rest being CH_4. Reservoir pressure is at about 10 MPa, and temperature is around 50 ^{o}C. CO_2 is pumped down the two injection wells at a fairly constant injection rate of ~40 m^3/d per well. Wellhead pressure is ~10 to 12MPa. The distance from injection well to the monitoring well 7-11 is about 500 meters. In our model we did not model the oil phase, but rather added the oil saturation to water saturation. The model starts with 24.7% gas phase and 75.3% water (+oil) phase. Initial $\delta^{13}C$ in the reservoir CO_2 is -16.9‰, while the value for injected CO_2 is -4.3‰.

Nightingale et al. (2009) reported reservoir mineralogy before CO_2 injection from well 7-11. Whole rock geochemistry, including X-Ray Fluorescence (XRF), Inductively Coupled Plasma-Atomic Emission Spectrometry (ICP-AES), X-Ray Diffraction (XRD), total carbonate, and total sulfide analysis, was completed by SGS Laboratories (Lakefield, Ontario). The available minerals are summarized in Table 5.3. The sandstone samples analyzed are composed primarily of quartz (up to 90%), with smaller amount of feldspar (K-feldspar and albite), muscovite, chlorite, pyrite, and clay (illite and kaolinite) present. Carbonate minerals present include both calcite and siderite.

Initial water chemistry from well 7-11 is reported in the Penn West Energy Trust Pembina Cardium 'A' Lease-CO_2 Pilot Project annual report 2005 and listed in Table 5.4.

Table 5.3 Mineral composition of recovered core from well 7-11 before CO2 injection

Mineral	Weight%
Quartz	85.5
K-feldspar	1.5

Albite	1.6
Mus/Ill	2.6
Chlorite	0.9
Kaolinite	2.8
Calcite	0.1
Siderite	1.1
Pyrite	0.6

Table 5.4 Initial water chemistry in well 7-11

Parameters	Values
pH	6.87
Total alkalinity (mg/L)	421
Na (mg/L)	131
K (mg/L)	5.9
Ca (mg/L)	134
Mg (mg/L)	15.2
Fe (mg/L)	2.87
Cl (mg/L)	12200

Modeled mole fraction of CO_2, $\delta_{13C}(CO_2)$, pH, and Ca concentration are plotted as a function of time in Figure 5.10 and Figure 5.11 for grid blocks that are 300m, 250m, and 200m away from the injection well, compared with field data from well 7-11. Field data show large fluctuations, but generally can be fitted with the reactive transport model. The measured mole%CO_2 increases from 1.75% to over 80%, while the code predicts that all the methane will be flushed out by CO_2 and the mole%CO_2 increases to 100%. The mole%CO_2 in the field does not achieve 100% probably because of the heterogeneity issue in the field. Since injected CO_2 gas would always flow through high permeability paths preferentially, the CH_4 in the low permeability zones might be bypassed by injected CO_2 and thus stays in the reservoir. Samples that mixed with these residual CH_4 would not have mole%CO_2 as high as 100%. We currently do not account for this effect in our 1D flow model. $\delta_{13C}(CO_2)$ increases from initial -16.9 to -4.3. The pH is measured at surface conditions in the field, and corrected to downhole conditions (M. Shevalier, personal communication). Ca concentration increases in the fluid sample by about 3 times due to calcite dissolution at low pH.

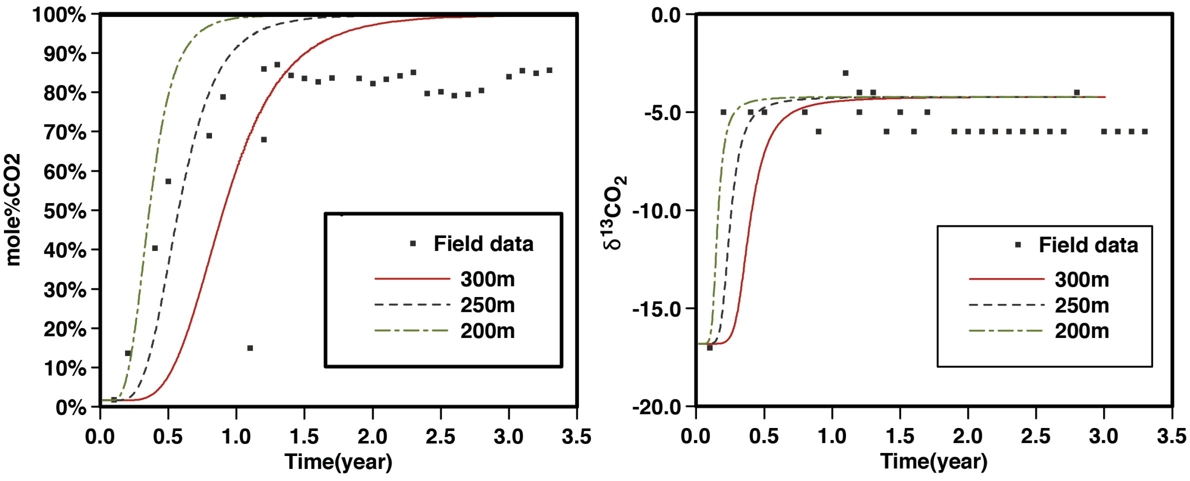

Figure 5.10 Fitting of mole%CO_2 and $\delta_{13C}(CO_2)$ time series data with reactive transport modeling

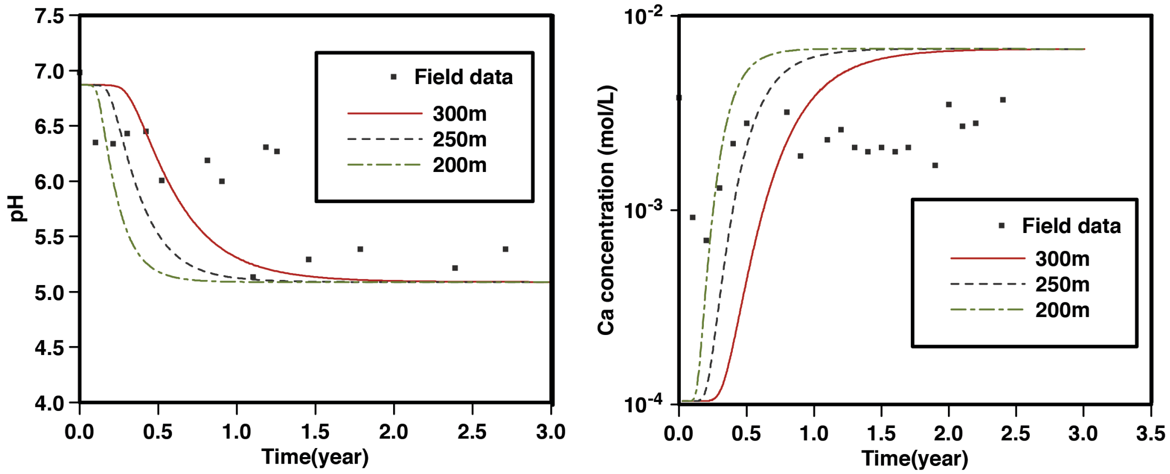

Figure 5.11 Fitting of pH and Ca concentration time series data with reactive transport modeling

5.6 Conclusions

A numerical code was developed to model the carbon isotope fractionation in CO_2 sequestration in addition to standard geochemical parameters such as pH and gas saturation. The code is an extension of the reactive transport code TOUGHREACT. The code is verified through modeling ideal systems including two-component gas mixture model, gas+water batch model, 1D flow and transport model, and mineral precipitation model. We show that the exchange of carbon isotopes between dissolved and gaseous carbon species, and between fluids (brine and supercritical CO_2), combined with fluid flow and transport, produce isotopic effects that are significantly different from simple two-component mixing. These effects are most prominent when permeability is low. The high variability in field isotope data might also be from the variability in initial mole% of CO_2. Other traditional geochemical parameters besides isotope ratios are also modeled with the current module of TOUGHREACT. These results are important in understanding the geochemical evolution in the subsurface during CO_2 sequestration.

References

Aagaard, P., Helgeson, H.C., 1982. Thermodynamic and kinetic constraints on reaction rates among minerals and aqueous solutions; I, Theoretical considerations. Am J Sci 282, 237-285.

AAPG, 1957. Correlation section across central
San Joaquin Valley fromSan Andreas fault to Sierra Nevada foot hills,plate 9:Pacific
Section, American Association ofPetroleum Geologists.

Aja, S.U., 2002. The stability of Fe-Mg chlorites in hydrothermal solutions: II. thermodynamic properties. Clay Clay Miner 50, 591-600.

Anderson, G., 2005. Thermodynamics of Natural Systems.

Armstrong-Altrin, J.S., Lee, Y.I., Verma, S.P., Ramasamy, S., 2004. Geochemistry of sandstones from the upper Miocene Kudankulam Formation, southern India: Implications for provenance, weathering, and tectonic setting. J Sediment Res 74, 285-297.

Arnold, R., Anderson, R., 1910. Geology and oil resources of the Coalinga district California. [s.n.], Washington :.

Assayag, N., Matter, J., Ader, M., Goldberg, D., Agrinier, P., 2009. Water-rock interactions during a CO2 injection field-test: Implications on host rock dissolution and alteration effects. Chemical Geology 265, 227-235.

Audigane, P., Gaus, I., Czernichowski-Lauriol, I., Pruess, K., Xu, T.F., 2007. Two-dimensional reactive transport modeling of CO2 injection in a saline Aquifer at the Sleipner site, North Sea. Am J Sci 307, 974-1008.

Baines, S.J., Worden, R.H., 2004. The long-term fate of CO2 in the subsurface: natural analogues for CO2 storage. Geological Society, London, Special Publications 233, 59-85.

Banfield, J.F., Murakami, T., 1998. Atomic-resolution transmission electron microscope evidence for the mechanism by which chlorite weathers to 1 : 1 semi-regular chlorite-vermiculite. Am Mineral 83, 348-357.

Bartow, J.A., 1987. The Cenozoic evolution ofthe San Joaquin Valley, California: U.S.
Geological Survey Open-File Report 87-581, 74 p.

Berger, A., Gier, S., Krois, P., 2009. Porosity-preserving chlorite cements in shallow-marine volcaniclastic sandstones: Evidence from Cretaceous sandstones of the Sawan gas field, Pakistan. Aapg Bull 93, 595-615.

Black, P.M., Clark, A.S.B., Hawke, A.A., 1993. Diagenesis and Very Low-Grade Metamorphism of Volcaniclastic Sandstones from Contrasting Geodynamic Environments, North-Island, New-Zealand - the Murihiku and Waipapa Terranes. J Metamorph Geol 11, 429-435.

Bloch, S., 1991. Empirical prediction of porosity and permeability in sandstones.

Bottinga, Y., 1968. Calculation of fractionation factors for carbon and oxygen isotopic exchange in the system calcite-carbon dioxide-water. The Journal of Physical Chemistry 72, 800-808.

Brandt, F., Bosbach, D., Krawczyk-Bärsch, E., Arnold, T., Bernhard, G., 2003. Chlorite dissolution in the acid ph-range: a combined microscopic and macroscopic approach. Geochim Cosmochim Ac 67, 1451-1461.

Burch, T.E., Nagy, K.L., Lasaga, A.C., 1993. Free energy dependence of albite dissolution kinetics at 80 °C and pH 8.8. Chem Geol 105, 137-162.

Cama, J., Ganor, J., Ayora, C., Lasaga, C.A., 2000. Smectite dissolution kinetics at 80 °C and pH 8.8. Geochim Cosmochim Ac 64, 2701-2717.

Cameron, D., John, C., California Energy, C., United States. Dept. of, E., National Energy Technology, L., United States. Dept. of Energy. Office of, S., Technical, I., 2005. An Overview of Geologic Carbon Sequestration Potential in California. United States. Dept. of Energy ; distributed by the Office of Scientific and Technical Information, U.S. Dept. of Energy, Washington, D.C.; Oak Ridge, Tenn.

Carroll, S., Mroczek, E., Alai, M., Ebert, M., 1998. Amorphous silica precipitation (60 to 120 °C): comparison of laboratory and field rates. Geochim Cosmochim Ac 62, 1379-1396.

De Ros, L.F., Morad, S., Al-Aasm, I.S., 1997. Diagenesis of siliciclastic and volcaniclastic sediments in the Cretaceous and Miocene sequences of the NW African margin (DSDP Leg 47A, Site 397). Sediment Geol 112, 137-156.

De Ros, L.F., Morad, S., Palm, P.S.G., 1994. The Role of Detrital Composition and Climate on the Diagenetic Evolution of Continental Molasses - Evidence from the Cambro-Ordovician Guaritas Sequence, Southern Brazil. Sediment Geol 92, 197-228.

DePaolo, D.J., 2006. Isotopic effects in fracture-dominated reactive fluid-rock systems. Geochim Cosmochim Ac 70, 1077-1096.

DePaolo, D.J., 2011. Surface kinetic model for isotopic and trace element fractionation during precipitation of calcite from aqueous solutions. Geochim Cosmochim Ac 75, 1039-1056.

Dibblee, T.W., Jr., 1971. Geologic maps ofCalifornia: Coalinga, Greenfield, Hernandez
Valley, Joaquin Rocks, New Idria, Panoche Valley, Parkfield, Priest Valley, "Reef
Ridge", San Ardo, and San Miguel quadrangles: U. S. Geological Survey Open File
Report 71-0087, scale 1:62,500.

Dickinson, W.R., Snyder, W.S., 1979. Geometry of triple junctions related to San Andreas Transform. Journal of Geophysical Research: Solid Earth 84, 561-572.

Dimarco, M.J., Lowe, D.R., 1989. Petrography and Provenance of Silicified Early Archean Volcaniclastic Sandstones, Eastern Pilbara Block, Western-Australia. Sedimentology 36, 821-836.

Dove, P.M., Han, N., Wallace, A.F., De Yoreo, J.J., 2008. Kinetics of amorphous silica dissolution and the paradox of the silica polymorphs. Proceedings of the National Academy of Sciences.

Durr, S.B., Gibling, M.R., 1994. Early Cretaceous Volcaniclastic and Quartzose Sandstones from North Central Nepal - Composition, Sedimentology and Geotectonic Significance. Geol Rundsch 83, 62-75.

Edwards, B.R., Russell, J.K., 1996. A review and analysis of silicate mineral dissolution experiments in natural silicate melts. Chem Geol 130, 233-245.

Emberley, S., Hutcheon, I., Shevalier, M., Durocher, K., Mayer, B., Gunter, W.D., Perkins, E.H., 2005. Monitoring of fluid-rock interaction and CO2 storage through produced fluid sampling at the Weyburn CO2-injection enhanced oil recovery site, Saskatchewan, Canada. Appl Geochem 20, 1131-1157.

Forster, A., Schoner, R., Forster, H.J., Norden, B., Blaschke, A.W., Luckert, J., Beutler, G., Gaupp, R., Rhede, D., 2010. Reservoir characterization of a CO2 storage aquifer: The Upper Triassic Stuttgart Formation in the Northeast German Basin. Mar Petrol Geol 27, 2156-2172.

Foss, C.D., 1972. A preliminary sketch of the San Joaquin Valley stratigraphic framework, in Rennie, E. W., Jr., cd., 1972 Guidebook - Geology and Oilfields, West Side Central San Joaquin Valley: Pacific Section, American Association of Petroleum Geologists, Society of Exploration Geophysicists, and Society of Economic Paleontologists and Mineralogists, p. 40-50.

Foster, D.A., 1962. Interpretation of the composition and a classification of the chlorites. Geological Survey Professional Paper 414-A.U.S. Geological Survey, Washing- ton, D.C (38 pp.).

Gailhanou, H., Rogez, J., Miltenburg, J.C.v., Genderen, A.C.G.v., Grenèche, J.M., Gilles, C., Jalabert, D., Michau, N., Gaucher, E.C., Blanc, P., 2009. Thermodynamic properties of chlorite CCa-2. Heat capacities, heat contents and entropies. Geochim Cosmochim Ac 73, 4738-4749.

Gailhanou, H., Rogez, J., Miltenburg, J.C.v., Genderen, A.v., Grenèche, J.M., Gaucher, E.C., Crouzet, C., Blanc, S.T.a.P., 2007. Experimental determination of thermodynamic properties of a chlorite. International Meeting, September 17-18, 2007, Lille, France Page 355. Clays in natural &engineered barriers for radioactive water confinement.

Galehouse, J.S., 1967. Provenance and paleocurrents of the Paso Robles formation.

Garzanti, E., 1985. The Sandstone Memory of the Evolution of a Triassic Volcanic Arc in the Southern Alps, Italy. Sedimentology 32, 423-433.

Gibson-Poole, C.M., Svendsen, L., Underschultz, J., Watson, M.N., Ennis-King, J., van Ruth, P.J., Nelson, E.J., Daniel, R.F., Cinar, Y., 2008. Site characterisation of a basin-scale CO2 geological storage system: Gippsland Basin, southeast Australia. Environ Geol 54, 1583-1606.

Gunter, W.D., Perkins, E.H., Hutcheon, I., 2000. Aquifer disposal of acid gases: modelling of water-rock reactions for trapping of acid wastes. Appl Geochem 15, 1085-1095.

Harding, T.P., 1976. Tectonic significance and hydrocarbon trapping consequences of sequential folding synchronous with San Andreas faulting, San Joaquin Valley, California. AAPG Bulletin 60, 356-378.

Hawlader, H.M., 1990. Diagenesis and reservoir potential of volcanogenic sandstones--Cretaceous of the Surat Basin, Australia. Sediment Geol 66, 181-195.

Hayashi, H., Yamada, M., 1990. Kinetics of dissolution of noncrystalline oxides and crystalline clay minerals in a basic tiron solution. Clay Clay Miner 38, 308-314.

Hellmann, R., Tisserand, D., 2006. Dissolution kinetics as a function of the Gibbs free energy of reaction: An experimental study based on albite feldspar. Geochim Cosmochim Ac 70, 364-383.

Hitchon, B., 2009. Pembina Cardium CO2 Monitoring Pilot: A CO2-EOR Project, Alberta, Canada: Final Report. Geoscience Publishing, Limited.

Ingersoll, R.V., 1983. Petrofacies and provenance of late Mesozoic forearc basin, Northern and Central California. Aapg Bull 67, 1125-1142.

Intergovernmental Panel on Climate Change, 2005. IPCC special report on carbon dioxide capture and storage : summary for policymakers. IPCC, S.l.

Johnson, G., Mayer, B., Shevalier, M., Nightingale, M., Hutcheon, I., 2011. Tracing the movement of CO2 injected into a mature oilfield using carbon isotope abundance ratios: The example of the Pembina Cardium CO2 Monitoring project. International Journal of Greenhouse Gas Control 5, 933-941.

Johnson, G., Raistrick, M., Mayer, B., Shevalier, M., Taylor, S., Nightingale, M., Hutcheon, I., 2009. The use of stable isotope measurements for monitoring and verification of CO2 storage. Energy Procedia 1, 2315-2322.

Johnson, T.M., DePaolo, D.J., 1994. Interpretation of isotopic data in groundwater-rock systems: Model development and application to Sr isotope data from Yucca Mountain. Water Resources Research 30, 1571-1587.

Kampman, N., Bickle, M., Becker, J., Assayag, N., Chapman, H., 2009. Feldspar dissolution kinetics and Gibbs free energy dependence in a CO2-enriched groundwater system, Green River, Utah. Earth Planet Sc Lett 284, 473-488.

Kelemen, P.B., Matter, J., 2008. In situ carbonation of peridotite for CO2 storage. P Natl Acad Sci USA 105, 17295-17300.

Kitamura, K.X., Z., 2006. An experimental study of Residual Gas Saturation of Carbon Dioxide in water-saturated porous sandstone by using multi-channel seismic wave imaging method. American Geophysical Union, Fall Meeting 2006, abstract #H51E-0531.

Kittrick, 1982. Solubility of two high-Mg and two high-Fe chloites using multiple equilibria. Clay Clay Miner. 30(3), 167– 179.

Klinkenberg, L., 1941. The Permeability Of Porous Media To Liquids And Gases. Drilling and Production Practice, 200–213. 1941: American Petroleum Institute.

Kumar, M. Noh, G.A. Pope, K. Sepehrnoori, S. Bryant, L.W. Lake, 2004. Reservoir Simulation of CO2 Storage in Deep Saline Aquifers. SPE/DOE Symposium on Improved Oil Recovery, 22-26 April 2006, Tulsa, Oklahoma, USA.

Landrot, G., Ajo-Franklin, J.B., Yang, L., Cabrini, S., Steefel, C.I., 2012. Measurement of accessible reactive surface area in a sandstone, with application to CO2 mineralization. Chem Geol 318–319, 113-125.

Lasaga, A.C., 1984. Chemical kinetics of water-rock interactions. Journal of Geophysical Research: Solid Earth 89, 4009-4025.

Lasaga, A.C., 1995. Fundamental approaches in describing mineral dissolution and precipitation rates. Reviews in Mineralogy and Geochemistry 31, 23-86.

Lasaga, A.C., 1998. Kinetic theory in the earth sciences. Princeton University Press, Princeton, N.J.

Lerbekmo, J.F., 1956. The character and origin of late-Tertiary blue sandstones in central California.

Lerbekmo, J.F., 1957. Authigenic montmorillinoid cement in andesitic sandstones of central California. Journal of Sedimentary Petrology, v. 27, no. 3, p. 298-305.

Lerbekmo, J.F., 1961. Genetic relationship among Tertiary blue sandstones in central California. Journal of Sedimentary Research 31, 594-602.

Link, M.H., Helmold, K.P., Long, W.T., 1990. Depositional Environments and Reservoir Characteristics of the Upper Miocene Etchegoin and Chanac Formations, Kern Front Oil Field, California. Pacific Section, SEPM (Society for Sedimentary Geology).

Linn, A.M., Depaolo, D.J., Ingersoll, R.V., 1992. Nd-Sr Isotopic, Geochemical, and Petrographic Stratigraphy and Paleotectonic Analysis - Mesozoic Great Valley Fore-Arc Sedimentary-Rocks of California. Geol Soc Am Bull 104, 1264-1279.

Loomis, K.B., 1990. Late Neogene depositional history and paleoenvironments of the west-central San Joaquin basin, California.

Lowson, R.T., Brown, P.L., Comarmond, M.C.J., Rajaratnam, G., 2007. The kinetics of chlorite dissolution. Geochim Cosmochim Ac 71, 1431-1447.

Lowson, R.T., Comarmond, M.C.J., Rajaratnam, G., Brown, P.L., 2005. The kinetics of the dissolution of chlorite as a function of pH and at 25°C. Geochim Cosmochim Ac 69, 1687-1699.

Lu, J., Kharaka, Y.K., Thordsen, J.J., Horita, J., Karamalidis, A., Griffith, C., Hakala, J.A., Ambats, G., Cole, D.R., Phelps, T.J., Manning, M.A., Cook, P.J., Hovorka, S.D., 2012. CO2-rock-brine interactions in Lower Tuscaloosa Formation at Cranfield CO2 sequestration site, Mississippi, U.S.A. Chem Geol 291, 269-277.

Maher, K., DePaolo, D.J., Christensen, J.N., 2006. U-Sr isotopic speedometer: Fluid flow and chemical weathering rates in aquifers. Geochim Cosmochim Ac 70, 4417-4435.

Maher, K., Steefel, C.I., White, A.F., Stonestrom, D.A., 2009. The role of reaction affinity and secondary minerals in regulating chemical weathering rates at the Santa Cruz Soil Chronosequence, California. Geochim Cosmochim Ac 73, 2804-2831.

Malmström, M., Banwart, S., Lewenhagen, J., Duro, L., Bruno, J., 1996. The dissolution of biotite and chlorite at 25°C in the near-neutral pH region. Journal of Contaminant Hydrology 21, 201-213.

Matter, J.M., Takahashi, T., Goldberg, D., 2007. Experimental evaluation of in situ CO2-water-rock reactions during CO2 injection in basaltic rocks: Implications for geological CO2 sequestration. Geochem Geophy Geosy 8, Q02001.

Maurice Shevalier, M.N., Gareth Johnson, Bernhard Mayer and Ian Hutcheon 2008. Reservoir Geochemical Monitoring of the PennWest CO2-EOR Site. 2008 CSPG CSEG CWLS Convention.

McGrail, B.P., Schaef, H.T., Ho, A.M., Chien, Y.J., Dooley, J.J., Davidson, C.L., 2006. Potential for carbon dioxide sequestration in flood basalts. J Geophys Res-Sol Ea 111.

Mito, S., Xue, Z., Ohsumi, T., 2008. Case study of geochemical reactions at the Nagaoka CO2 injection site, Japan. Int J Greenh Gas Con 2, 309-318.

Mito, S., Xue, Z., Sato, T., 2013. Effect of formation water composition on predicting CO2 behavior: A case study at the Nagaoka post-injection monitoring site. Appl Geochem 30, 33-40.

Monicard, R.P., 1980. Properties of Reservoir Rocks: Core Analysis. Gulf Publishing Co., Houston, TX.

Myrttinen, A., Becker, V., van Geldern, R., Wurdemann, H., Morozova, D., Zimmer, M., Taubald, H., Blum, P., Barth, J.A.C., 2010. Carbon and oxygen isotope indications for CO2 behaviour after injection: First results from the Ketzin site (Germany). International Journal of Greenhouse Gas Control 4, 1000-1006.

Nagy, K.L., Cygan, R.T., Hanchar, J.M., Sturchio, N.C., 1999. Gibbsite growth kinetics on gibbsite, kaolinite, and muscovite substrates: atomic force microscopy evidence for epitaxy and an assessment of reactive surface area. Geochim Cosmochim Ac 63, 2337-2351.

Nagy, K.L., Lasaga, A.C., 1992. Dissolution and precipitation kinetics of gibbsite at 80 °C and pH 3: The dependence on solution saturation state. Geochim Cosmochim Ac 56, 3093-3111.

Namson, J.S., Davis, T.L., 1988. Seismically active fold and thrust belt in the San Joaquin Valley, central California. Geological Society of America Bulletin 100, 257-273.

Narasimhan, T.N., Witherspoon, P.A., 1976. An integrated finite difference method for analyzing fluid flow in porous media. Water Resour. Res. 12, 57-64.

Nightingale, M., Johnson, G., Shevalier, M., Hutcheon, I., Perkins, E., Mayer, B., 2009. Impact of injected CO2 on reservoir mine ralogy during CO2-EOR. Energy Procedia 1, 3399-3406.

Oelkers, E.H., Helgeson, H.C., Shock, E.L., Sverjensky, D.A., Johnson, J.W., Pokrovskii, V.A., 1995. SUMMARY OF THE APPARENT STANDARD PARTIAL MOLAL GIBBS FREE-ENERGIES OF FORMATION OF AQUEOUS SPECIES, MINERALS, AND GASES AT PRESSURES 1 TO 5000 BARS AND TEMPERATURES 25 TO 1000-DEGREES-C. J Phys Chem Ref Data 24, 1401--1560.

Palandri, J.K., Y.K., 2004. A compilation of rate parameters of water-mineral interaction kinetics for application to geochemical modeling. US Geol. Surv. Open File Report2004-1068, 64pp.

Park, A.H.A., Jadhav, R., Fan, L.S., 2003. CO2 mineral sequestration: Chemically enhanced aqueous carbonation of serpentine. Can J Chem Eng 81, 885-890.

Parkhurst, D.L., 1999. User's guide to PHREEQC (version 2) [microform] : a computer program for speciation, batch-reaction, one-dimensional transport, and inverse geochemical calculations / by David L. Parkhurst and C.A.J. Appelo. U.S. Geological Survey : Earth Science Information Center, Open-File Reports Section [distributor], Denver, Colo. :.

Perkins, J.A., 1987. Provenance of the upper Miocene and Pliocene Etchegoin Formation : implications for paleogeography of the late Miocene of central California.

Peters, C.A., 2009. Accessibilities of reactive minerals in consolidated sedimentary rock: An imaging study of three sandstones. Chem Geol 265, 198-208.

Prigiobbe, V., Mazzotti, M., 2011. Dissolution of olivine in the presence of oxalate, citrate, and CO2 at 90 degrees C and 120 degrees C. Chem Eng Sci 66, 6544-6554.

Pruess, K., 1991a. TOUGH2: A general-purpose numerical simulator for multiphase fluid and heat flow, p. Pages: (102 p).

Pruess, K., 1991b. TOUGH2: A general-purpose numerical simulator for multiphase fluid and heat flow, p. Medium: ED; Size: Pages: (102 p).

Raghavan, R., 2006. Some observations on the scale dependence of permeability by pumping tests. Water Resour. Res. 42, W07402.

Raistrick, M., Mayer, B., Shevalier, M., Perez, R.J., Hutcheon, I., Perkins, E., Gunter, B., 2006. Using Chemical and Isotopic Data to Quantify Ionic Trapping of Injected Carbon Dioxide in Oil Field Brines. Environ Sci Technol 40, 6744-6749.

Reed, J.K., Gipson, M., Neese, D.G., 1993a. Hydrocarbon Potential of Sandstone Reservoirs in the Neogene East Slovakian Basin .1. A Petrographic Examination of Lithology, Porosity, and Diagenesis. J Petrol Geol 16, 89-108.

Reed, J.K., Gipson, M., Neese, D.G., 1993b. Hydrocarbon potential of sandstone reservoirs in the neogene east Slovakian basin part I: a petrographic examination of lithology, porosity and diagenesis. J Petrol Geol 16, 89-108.

Remy, R.R., 1994. Porosity Reduction and Major Controls on Diagenesis of Cretaceous-Paleocene Volcaniclastic and Arkosic Sandstone, Middle Park Basin, Colorado. J Sediment Res A 64, 797-806.

Rochelle, C.A., Bateman, K., MacGregor, R., Pearce, J.M., Savage, D., Wetton, P.D., 1994. Experimental Determination of Chlorite Dissolution Rates. . MRS Proceedings 353.

Rodrigues, K., 1991. Organic Geochemistry and Petroleum Potential of Jamaica. J Petrol Geol 14, 309-322.

Rolle, M., Chiogna, G., Bauer, R., Griebler, C., Grathwohl, P., 2010. Isotopic Fractionation by Transverse Dispersion: Flow-through Microcosms and Reactive Transport Modeling Study. Environ Sci Technol 44, 6167-6173.

Roser, B.P., Coombs, D.S., Korsch, R.J., Campbell, J.D., 2002. Whole-rock geochemical variations and evolution of the arc-derived Murihiku Terrane, New Zealand. Geol Mag 139, 665-685.

Ryu, I.-C., 2003. Petrography, diagenesis and provenance of Eocene Tyee Basin sandstones, southern Oregon Coast Range: New view from sequence stratigraphy. Isl Arc 12, 398-410.

Saccocia, P.J., Seyfried Jr, W.E., 1994. The solubility of chlorite solid solutions in 3.2 wt% NaCl fluids from 300–400°C, 500 bars. Geochim Cosmochim Ac 58, 567-585.

Sausse, J., Jacquot, E., Fritz, B., Leroy, J., Lespinasse, M., 2001. Evolution of crack permeability during fluid,rock interaction. Example of the Brzouard granite (Vosges, France). Tectonophysics 336, 199-214.

Singleton, M.J., Sonnenthal, E.L., Conrad, M.E., DePaolo, D.J., Gee, G.W., 2004. Multiphase Reactive Transport Modeling of Seasonal Infiltration Events and Stable Isotope Fractionation in Unsaturated Zone Pore Water and Vapor at the Hanford Site. Vadose Zone Journal 3, 775-785.

Smith, M.M., Wolery, T.J., Carroll, S.A., 2013. Kinetics of chlorite dissolution at elevated temperatures and CO2 conditions. Chem Geol 347, 1-8.

Smyth, H.R., Hall, R., Nichols, G.J., 2008. Significant volcanic contribution to some quartz-rich sandstones, East Java, Indonesia. J Sediment Res 78, 335-356.

Sonnenthal, E., Ito, A., Spycher, N., Yui, M., Apps, J., Sugita, Y., Conrad, M., Kawakami, S., 2005. Approaches to modeling coupled thermal, hydrological, and chemical processes in the Drift Scale Heater Test at Yucca Mountain. Int J Rock Mech Min 42, 698-719.

Spycher, N., Pruess, K., 2005. CO2-H2O mixtures in the geological sequestration of CO2. II. Partitioning in chloride brines at 12-100°C and up to 600 bar. Geochim Cosmochim Ac 69, 3309-3320.

Steefel, C.I., 2007. CrunchFlow User's Manual. Lawrence Berkeley National Laboratory.

Steefel, C.I., DePaolo, D.J., Lichtner, P.C., 2005. Reactive transport modeling: An essential tool and a new research approach for the Earth sciences. Earth Planet Sc Lett 240, 539-558.

Steefel, C.I., Lasaga, A.C., 1994. A Coupled Model for Transport of Multiple Chemical-Species and Kinetic Precipitation Dissolution Reactions with Application to Reactive Flow in Single-Phase Hydrothermal Systems. Am J Sci 294, 529-592.

Summer, N.S., Verosub, K.L., 1992. Diagenesis and organic maturation of sedimentary rocks under volcanic strata, Oregon. Aapg Bull 76, 1190-1199.

Sur, K.H., Lee, Y.I., Hisada, K., 2002. Diagenesis of the Lower Cretaceous Kanmon Group sandstones, SW Japan. J Asian Earth Sci 20, 921-935.

Tang, Z.H., Parnell, J., Longstaffe, F.J., 1997. Diagenesis and reservoir potential of Permian-Triassic fluvial/lacustrine sandstones in the southern Junggar basin, northwestern China. Aapg Bull 81, 1843-1865.

Thode, H.G., Shima, M., Rees, C.E., Krishnamurty, K.V., 1965. Carbon-13 isotope effects in systems containing carbon dioxide, bicarbonate, carbonate, and metal ions. Canadian Journal of Chemistry 43, 582-595.

Weibel, E.R., 1981. Stereological Methods. Vol. 1. Practical Methods for Biological Morphometry. By Ewald R. Weibel. Journal of Microscopy 121, 131-132.

Wentworth, C.M., Zoback, M.D., 1989. The style of Late Cenozoic deformation at the eastern front of the California Coast Ranges. Tectonics 8, 237-246.

White Art, F., Peterson Maria, L., 1990. Role of Reactive-Surface-Area Characterization in Geochemical Kinetic Models, Chemical Modeling of Aqueous Systems II. American Chemical Society, pp. 461-475.

Wolela, A., 2010. Diagenetic evolution of the Ansian-Pliensbachian Adigrat Sandstone, Blue Nile Basin, Ethiopia. J Afr Earth Sci 56, 29-42.

wolery, T.J., 1992. EO3/6:Software package for geochemical modeling of aqueous systems: Package overview and installation guide (version 7.0). Lawrence Livermore Natioinal Laboratory Report UCRL-MA-210662 PT I.

Wollast, R., Chou, L., 1985. Kinetic Study of The Dissolution of Albite with a Continuous Flow-Through Fluidized Bed Reactor, in: Drever, J. (Ed.), The Chemistry of Weathering. Springer Netherlands, pp. 75-96.

Xu, T., Pruess, K., 2001a. Modeling Multiphase Non-isothermal Fluid Flow and Reactive Geochemical Transport in Variably Saturated Fractured Rocks: 1. Methodology. Am J Sci 301, 16-33.

Xu, T., Sonnenthal, E., Spycher, N., Pruess, K., 2004. TOUGHREACT User's Guide: A Simulation Program for Non-isothermal Multiphase Reactive geochemical Transport in Variable Saturated Geologic Media.

Xu, T.F., Pruess, K., 2001b. On fluid flow and mineral alteration in fractured caprock of magmatic hydrothermal systems. J Geophys Res-Sol Ea 106, 2121-2138.

Yang, L., Steefel, C.I., 2008. Kaolinite dissolution and precipitation kinetics at 20°C and pH 4. Geochim Cosmochim Ac 72, 99-116.

Zeebe, R.E., 2011. On the molecular diffusion coefficients of dissolved CO2 and their dependence on isotopic mass. Geochim Cosmochim Ac 75, 2483-2498.

Zerai, B., Saylor, B.Z., Matisoff, G., 2006. Computer simulation of CO2 trapped through mineral precipitation in the Rose Run Sandstone, Ohio. Appl Geochem 21, 223-240.

Zhang, S., DePaolo, D., Xu, T., Zheng, L., 2013. Mineralization of carbon dioxide sequestered in volcanogenic sandstone reservoir rocks Int J Greenh Gas Con.